

**UNIVERSITÄT
BAYREUTH**

Lehrstuhl für Kristallographie

Modulated phases in organic molecular crystals

Von der Universität Bayreuth
zur Erlangung des akademischen Grades eines
Doktors der Naturwissenschaften (Dr. rer. nat)
genehmigte Abhandlung

vorgelegt von
Somnath Dey
aus Serampore, Hooghly Indien

1. Gutachter: Prof. dr. Sander van Smaalen
2. Gutachter: Prof. dr. Wulf Depmeier

Tag der Einreichung: 27.09.2016
Tag der Kolloquiums: 23.02.2017

Contents

1	Introduction	5
2	Molecular crystals and their properties	11
2.1	The higher-dimensional superspace approach	11
2.1.1	Reciprocal space	12
2.1.2	Direct space	15
2.1.3	Examples	18
2.2	Structural phase transitions	23
2.2.1	General overview	23
2.2.2	Modulated phases	24
2.3	Twinning	30
2.3.1	Definition and types	30
2.3.2	Symmetry relations	31
2.4	Diffuse scattering and disorder	33
3	Superspace description of trimethyltin hydroxide at $T = 100$ K	37
3.1	Introduction	37
3.2	Experimental	40
3.2.1	Data collection	40
3.2.2	Structure solution and refinement	44
3.3	Discussion	46
3.4	Conclusion	52
3.5	Acknowledgements	52

4	Modulated inter-strand C–H···O bonds in the high Z' superstructure of trimethyltin hydroxide	53
4.1	Introduction	54
4.2	Experimental	56
4.2.1	Diffraction experiment and data integration	56
4.2.2	Structure solution and refinement	59
4.3	Results and discussion	62
4.3.1	Symmetry relation to the low temperature structure	62
4.3.2	Conformation of the strands	62
4.3.3	Intra-strand and inter-strand interactions	63
4.4	Conclusion	68
5	The $Z' = 12$ superstructure of Λ-cobalt(III) sepulchrate trinitrate governed by C–H···O hydrogen bonds	69
5.1	Introduction	70
5.2	Experimental	72
5.2.1	Diffraction experiment and data integration	72
5.2.2	Structure solution and refinement	76
5.3	Discussion	80
5.3.1	Variation of molecular conformations for $Z' = 12$	80
5.3.2	Competing intermolecular interactions	84
5.4	Conclusion	90
5.5	Acknowledgement	90
6	Intermediate low temperature phases of Λ-Co(III) sepulchrate trinitrate	91
6.1	Single-crystal X-ray diffraction	91
6.1.1	Data integration and analysis of diffracted peaks	93
6.1.2	Structure solution and refinement of phase III	96
6.2	Discussion	98
6.2.1	Monoclinic distortion	101
6.2.2	Intermolecular interactions	103
6.3	Conclusion	105

<i>CONTENTS</i>	3
7 Summary	107
8 Zusammenfassung	109
A Supplementary material: Me₃SnOH	113
B Supplementary material: Λ-Co(sep)(NO₃)₃	131
Bibliography	141
Publications	155
Acknowledgements	157
Declaration	159

Chapter 1

Introduction

In crystals, modulated phases can be differentiated from classical three-dimensional periodic phases by their diffraction patterns. The diffraction pattern of a classical three dimensional periodic crystal shows sharp Bragg reflections arranged regularly in three-dimensions (Fig. 1.1(a)), which means that constituents of the crystal are arranged according to a three-dimensional lattice. When the crystal possesses a modulated structure, additional reflections, the so-called satellite reflections are observed (Fig. 1.1(b)), which means that the constituents of the crystal are arranged in such a way that they are regularly displaced from three-dimensional basic positions and these displacements can be described by a periodic modulation function.

Earliest discoveries of modulated phase in molecular organic crystals were made in years 1947 and 1948. The diffraction pattern of organic molecular complexes of 4:4'-dinitrodiphenyl with 4-chloro-, 4-bromo-, 4-iodo- and 4:4'-diiododiphenyl show

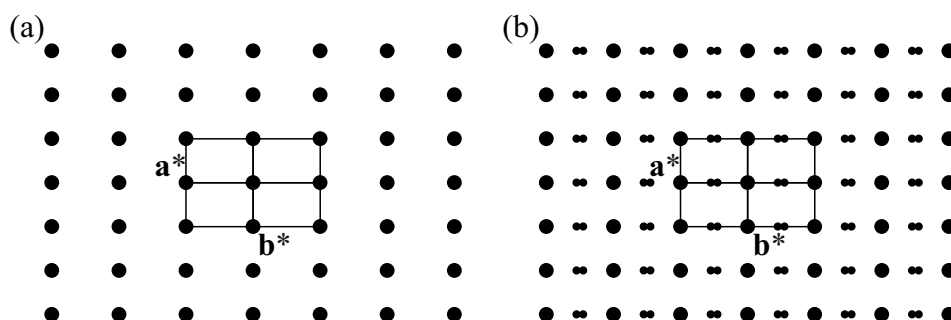


Figure 1.1: Schematic drawing of the diffraction pattern of a crystal showing (a) three-dimensional periodic phase and (b) modulated phase.

a mixture of sharp and weak spots (James and Saunder, 1947; 1948). These weak spots could be found systematically along \mathbf{c}^* in between the sharp spots. The authors concluded that “periodic errors” in the regular spacing of layers of dinitrophenyl molecules along \mathbf{c} explain the origin of the weak spots in the diffraction pattern (James and Saunder, 1948). In 1952 in the diffraction pattern of *n*-hexadecane complex, a urea-hydrocarbon complex, weak reflections were observed equally spaced between strong reflections along the \mathbf{c}^* -axis (Smith, 1952). In direct space that means doubling of the \mathbf{c} -axis. Later, the mathematical tool for interpreting the diffraction pattern of incommensurately modulated structures which have subsets of strong reflections and weak reflections was proposed by de Wolff (1974). The idea was to introduce additional dimensions in order to recover periodicity of the diffraction pattern of incommensurately modulated crystals in a higher-dimensional space.

In Chapter 2 higher-dimensional superspace and embedding of three-dimensional space in such higher dimensional superspace is explained. A few examples of molecular crystals which are already published demonstrating origin of modulation in their crystal structures are introduced. Phase transitions leading to modulated phases in molecular crystals are discussed with the help of illustrative examples. Twinning as a result of phase transitions in crystals and twin relations are explained. Finally, brief descriptions of diffuse scattering and disorder are given.

The aim of this thesis is to understand origin and stability of modulated phases in organic molecular crystals. The focus is towards understanding the correlation between origin of the modulation and intra- and intermolecular interactions *via* crystal-chemical analysis. For this purpose, two compounds trimethyltin hydroxide, $(\text{CH}_3)_3\text{SnOH}$, abbreviated as Me_3SnOH and Λ -cobalt(III) sepulchrate trinitrate, $[\text{Co}(\text{C}_{12}\text{H}_{30}\text{N}_8)]^{3+}3(\text{NO}_3)^-$, abbreviated as $\text{Co}(\text{sep})(\text{NO}_3)_3$ are studied.

Trimethyltin hydroxide

Me_3SnOH is an organometallic compound where the Sn(IV) center is coordinated to three methyl groups and two hydroxy groups in a trigonal bipyramid. The compound has a dimeric structure in solution with two Sn–O groups forming a four-membered ring; in solid state it crystallizes as polymeric chains bridged by Sn–O–Sn bonds (Fig. 1.2) (Kriegsmann et al., 1962; Deacon et al., 1993). The crystal structure undergoes a first-order phase transition at $T_c \approx 176$ K from a high Z' phase to a

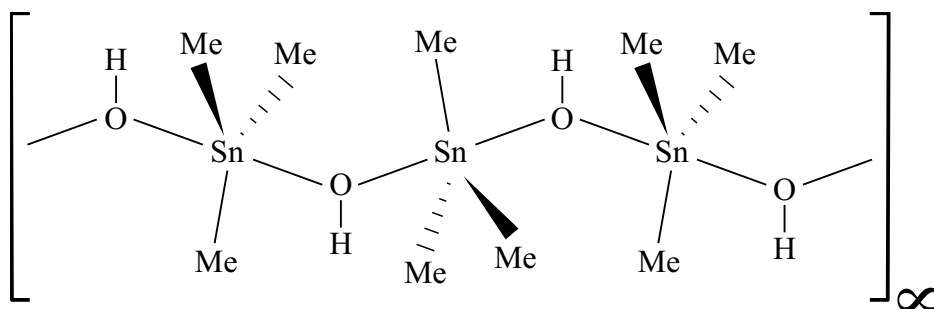


Figure 1.2: Schematic drawing of the polymeric chain of Me_3SnOH in solid state. Figure redrawn from [Anderson et al. \(2011\)](#).

low Z' phase upon cooling ([Anderson et al., 2011](#)).

In Chapter 3 the low Z' ($Z' = 1$) phase of Me_3SnOH is presented. Single-crystal X-ray diffraction experiment was performed at $T = 100$ K using synchrotron radiation. The twofold superstructure is solved as commensurately modulated structure within the (3+1)-dimensional superspace approach. Complete crystal-chemical analysis is done in order to understand the geometry of the individual polymeric chains and packing forces between chains in terms of C–H \cdots O hydrogen bonds and van der Waals forces. This low Z' structure serves as basis to understand the origin of the high Z' structure above $T = 176$ K.

In Chapter 4 the high Z' structure of Me_3SnOH and its relation to the crystal structure at $T = 100$ K is presented. Single crystal X-ray diffraction experiment was performed at $T = 220$ K using synchrotron radiation. The eightfold superstructure is solved as commensurately modulated structure within (3+1)-dimensional superspace approach in order to establish unique phase relation with the low Z' phase and describe a complete chemically and physically meaningful structural model. The origin of modulation due to competitive intra-chain forces is investigated. Effect of such modulation on the inter-chain C–H \cdots O hydrogen bonds is discussed.

Λ -Cobalt(III) sepulchrate trinitrate

$\text{Co}(\text{sep})(\text{NO}_3)_3$ is a co-ordination complex comprising of a cationic cage with Co^{3+} as center and three nitrate anions (Fig. 1.3). At room temperature the compound crystallizes in hexagonal space group $P6_322$. The $\text{Co}(\text{sep})$ cage and the two ordered nitrate groups are centred on threefold rotation axes. The third nitrate group

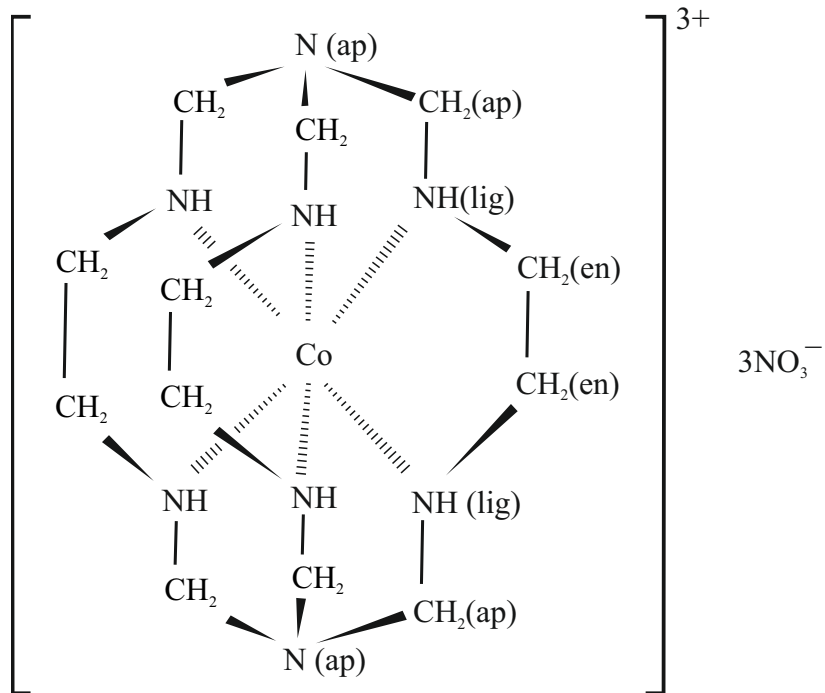


Figure 1.3: Schematic drawing of the chemical scheme of $\text{Co}(\text{sep})(\text{NO}_3)_3$. Figure redrawn from Schönleber et al. (2010).

is shifted out of the origin and show disorder of orientation (Dubicki et al., 1984; Schönleber et al., 2010). The packing comprises of layers of $\text{Co}(\text{sep})$ cages hydrogen bonded ($\text{N}-\text{H}\cdots\text{O}$) to two ordered nitrate groups and in between are layers of the third nitrate groups which are disordered by symmetry (Schönleber et al., 2010). Applying spectroscopic methods, the compound is reported to undergo phase transition at $T_{c1} = 133$ K upon cooling. This phase transition is proposed as order-disorder type with freezing of the disordered nitrate groups at inequivalent sites with possibilities of formation of multiple domains in the crystal (Dubicki et al., 1984). Temperature dependent single-crystal neutron diffraction experiments were performed by Larsen et al. (1988). By doing so phase transitions at $T_{c1} = 133$ K, $T_{c2} = 107$ K and $T_{c3} = 98$ K have been observed through the observation of satellite reflections in the diffraction pattern below T_{c1} . Hence the phase transition at T_{c1} can be characterized as a classical three-dimensional periodic to incommensurate phase transition. All the three low temperature phases II ($T_{c1} > T > T_{c2}$), III ($T_{c2} > T > T_{c3}$) and IV ($T < T_{c3}$) are modulated phases (Larsen et al., 1988).

In Chapter 5 the sixfold twinned 12-fold superstructure of $\text{Co}(\text{sep})(\text{NO}_3)_3$ in phase IV is presented. Data reduction of overlapping diffraction peaks contributed by pseudo-merohedral twin domains in the crystal is demonstrated. The crystal structure is solved and refined within the (3+1)-dimensional superspace formalism. Crystal chemical analysis is done to study competitive intermolecular forces in the form of N–H...O and C–H...O hydrogen bonds responsible for such high $Z' = 12$ superstructure. Possible reasons for long range ordering of the disordered nitrate groups are demonstrated.

In Chapter 6 the intermediate phases II and III of $\text{Co}(\text{sep})(\text{NO}_3)_3$ are presented. Determination of crystal symmetry from the analysis of intensities of Bragg reflections are demonstrated to understand the phase transition scheme of the compound. The incommensurately modulated structure at $T = 100$ K (phase III) is solved within the (3+1)-dimensional superspace approach. Relations between the crystal structures in phase I, phase III and phase IV are established.

In Chapter 7 results obtained during the course of this thesis are summarized in English and in Chapter 8 they are summarized in German. Additional information of the two compounds Me_3SnOH and $\text{Co}(\text{sep})(\text{NO}_3)_3$ are provided in the supplementary materials.

Chapter 2

Molecular crystals and their properties

A molecular compound in the solid state can be explained in terms of the different kinds of binding forces; within a molecule or a molecular fragment the binding forces are determined by strong covalent forces which do not change significantly with temperature and/or pressure. Between these molecular entities exist bonding forces like ionic bonds, hydrogen bonds, halogen bonds and van der Waals interactions, which show significant dependence on temperature and/or pressure. This difference in the bonding forces has profound effects on the crystal packing of these compounds ([Luis and Amorós, 1968](#)).

In this chapter, the superspace approach is introduced to understand how to recover periodicity in the diffraction pattern and crystal structure of a modulated crystal. In the context of the present thesis structural phase transitions, twinning and disorder are discussed with the help of illustrative examples.

2.1 The higher-dimensional superspace approach

A classical three-dimensional periodic crystal consists of atoms whose spacial arrangement follow three-dimensional periodicity. Aperiodicity (lack of three-dimensional periodicity) in crystal structures does not mean short range order or disorder. A crystal is defined as “any solid having an essentially discrete diffraction pattern” ([Pérez-Mato et al., 1992](#)) which clearly demonstrates that Bragg reflec-

tions need not to be arranged in such a way that they must necessarily follow three-dimensional periodicity but must possess long range order in crystals.

Description of aperiodic crystal structures within the $(3+d)$ -dimensional superspace approach is now well established (Janssen et al., 2007; Wagner and Schönleber, 2009; Schönleber, 2011; van Smaalen, 2012). In this notation, the “3” refers to the three-dimensional real space or the three-dimensional reciprocal space of the diffraction pattern and the additional “ d ” dimensions are orthogonal to the three-dimensional space. The three-dimensional real space is called the external or parallel space, V_E or V^{\parallel} and the subspace “ d ” is called the internal or perpendicular space, V_I or V^{\perp} (de Wolff, 1974; Schönleber, 2011). The reason behind such a distinction between the “3” and the additional dimensions “ d ” is made because these subspaces cannot be transformed into each other using symmetry operations.

In the course of the following subsections embedding of three-dimensional direct and reciprocal space in real and reciprocal superspace is explained. Modulation in molecular crystals are discussed based on selected examples taken from literature.

2.1.1 Reciprocal space

Diffraction pattern of modulated crystals have strong main reflections regularly surrounded by weaker satellite reflections. In incommensurately modulated crystals, these satellite reflections cannot be indexed using the basis vectors \mathbf{a}^* , \mathbf{b}^* , \mathbf{c}^* which are used to index the strong main reflections or any other set of three vectors.

In addition to the basis vectors \mathbf{a}^* , \mathbf{b}^* , \mathbf{c}^* modulation wave vectors up to three are required to index satellite reflections. In case of one-dimensional modulation one modulation vector \mathbf{q} and four integers $(hklm)$ for peak indexing, two vectors \mathbf{q}^1 and \mathbf{q}^2 for two-dimensional modulation and five integers $(hklmn)$ for peak indexing and three vectors \mathbf{q}^1 , \mathbf{q}^2 and \mathbf{q}^3 for three-dimensional modulation and six integers $(hklmnp)$ for peak indexing are used. The scattering vector, \mathbf{H} as function of reflection indices, lattice and modulation wave vectors can be expressed as

$$\begin{aligned}\mathbf{H}_{3+1} &= h\mathbf{a}^* + k\mathbf{b}^* + l\mathbf{c}^* + m\mathbf{q} \\ \mathbf{H}_{3+2} &= h\mathbf{a}^* + k\mathbf{b}^* + l\mathbf{c}^* + m\mathbf{q}^1 + n\mathbf{q}^2 \\ \mathbf{H}_{3+3} &= h\mathbf{a}^* + k\mathbf{b}^* + l\mathbf{c}^* + m\mathbf{q}^1 + n\mathbf{q}^2 + p\mathbf{q}^3\end{aligned}\tag{2.1}$$

where m , n and p are the indices of the satellite reflections. In case of two-dimensional modulation one has also to consider linear combinations of m and n

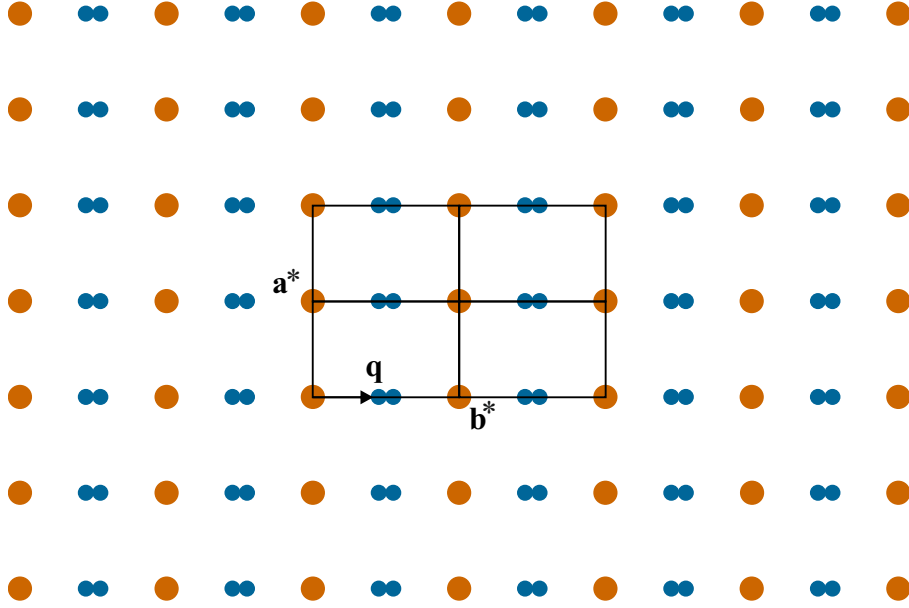


Figure 2.1: A schematic representation of the diffraction pattern showing the strong main reflections and weaker satellite reflections. The position vector of the satellite reflections with respect to the basis vectors of the basic cell is $\mathbf{q} = 0.4714\mathbf{b}^*$.

to define satellite order and in three-dimensional modulation case linear combinations of m , n and p .

From here on, discussion is limited to one-dimensional modulation since this thesis deals with description of crystal structures within the (3+1)-dimensional superspace.

Fig. 2.1 shows the $(\mathbf{a}^*, \mathbf{b}^*)$ -plane of the diffraction pattern of a hypothetical crystal as an example. With respect to the reciprocal lattice vectors \mathbf{a}^* , \mathbf{b}^* , \mathbf{c}^* or \mathbf{a}_1^* , \mathbf{a}_2^* , \mathbf{a}_3^* the modulation wave vector \mathbf{q} in general is expressed by

$$\mathbf{q} = \sigma_1\mathbf{a}_1^* + \sigma_2\mathbf{a}_2^* + \sigma_3\mathbf{a}_3^* \quad (2.2)$$

In the present example, $\sigma_1 = \sigma_3 = 0$ and $\sigma_2 = 0.4714$. The incommensurability of the modulation wave vector can be understood in terms of the irrational character of its components ($\sigma_2 = 0.4714 = \frac{\sqrt{2}}{3}$) and the aperiodicity then can be understood from the fact that the period of this modulation wave vector is not any integral number of lattice translations.

The diffraction pattern can be interpreted following the idea of de Wolff (de Wolff, 1974); the diffraction pattern consisting of main and satellite reflections is a projec-

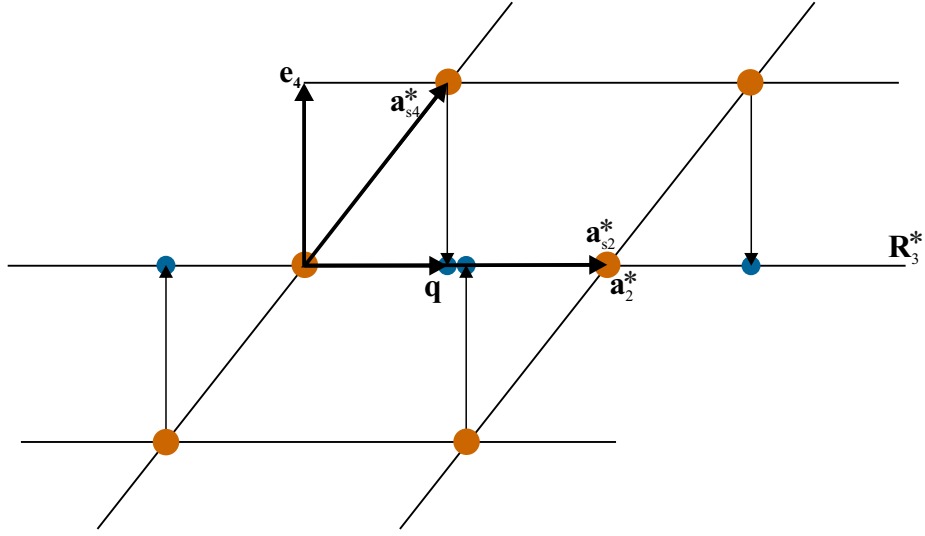


Figure 2.2: A schematic representation illustrating the embedding of three-dimensional reciprocal lattice in (3+1)-dimensional superspace. Reflections in (3+1)-dimensional superspace which run along \mathbf{a}_{s4}^* are projected as satellite reflections (blue) in three-dimensional space \mathbf{R}_3^* . Further explanation can be found in text.

tion of higher-dimensional reciprocal space onto three-dimensional reciprocal space (Fig. 2.2).

The reciprocal lattice vectors of three-dimensional real space \mathbf{a}_1^* , \mathbf{a}_2^* and \mathbf{a}_3^* are identified with \mathbf{a}_{s1}^* , \mathbf{a}_{s2}^* , \mathbf{a}_{s3}^* of (3+1)-dimensional reciprocal superspace. Unit vector \mathbf{e}_4 is introduced perpendicular to the real space. Hence, the lattice vectors \mathbf{a}_{s1}^* , \mathbf{a}_{s2}^* , \mathbf{a}_{s3}^* have components zero along \mathbf{e}_4 and the additional vector \mathbf{a}_{s4}^* has component one along \mathbf{e}_4 (eq. 2.3).

$$\begin{aligned}
 \mathbf{a}_{s1}^* &= (\mathbf{a}_1^*, 0) \\
 \mathbf{a}_{s2}^* &= (\mathbf{a}_2^*, 0) \\
 \mathbf{a}_{s3}^* &= (\mathbf{a}_3^*, 0) \\
 \mathbf{a}_{s4}^* &= (\mathbf{q}, 1)
 \end{aligned} \tag{2.3}$$

So far, the diffraction pattern of the present example shows incommensurate modulation. Consider that the modulation wave vector is $\mathbf{q} = \frac{1}{2}\mathbf{b}^*$ (compare Fig. 2.3 to Fig. 2.1). The component $\sigma = \frac{1}{2}$ means that the modulation wave vector is commensurate in character. One can either define the diffraction pattern in (3+1)-dimensional superspace or in a supercell in three-dimensions by doubling the \mathbf{b} -axis.

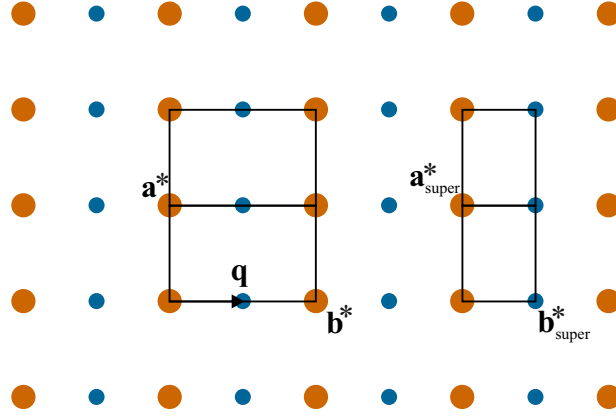


Figure 2.3: A schematic representation of the diffraction pattern of the hypothetical crystal consisting of satellite reflections at positions commensurate with the basic lattice. Modulation wave vector $\mathbf{q} = 0.5\mathbf{b}^*$. Alternate supercell description is done by defining the lattice parameters to be $\mathbf{a}_{\text{super}}^* = \mathbf{a}^*$, $\mathbf{b}_{\text{super}}^* = \frac{1}{2}\mathbf{b}^*$ and $\mathbf{c}_{\text{super}}^* = \mathbf{c}^*$.

Indexing the peaks in (3+1)-dimensional superspace enables unique relation between incommensurate and commensurate phase.

2.1.2 Direct space

In case of a classical three-dimensional periodic crystal structure, the reciprocal space is described as the Fourier transform of the crystal structure and the crystal structure is described by the inverse Fourier transform of the diffraction pattern. According to the property of Fourier transform, inverse Fourier transform of a higher dimensional space projected onto three-dimensional reciprocal space \mathbf{R}_3^* describes a three-dimensional section or cut \mathbf{R}_3 (real space) of a higher-dimensional space. Hence the crystal structure of a modulated crystal is interpreted as a three-dimensional section or cut of a higher-dimensional periodic structure.

Fig. 2.4 presents a schematic representation of the structure of the hypothetical crystal in (3+1)-dimensional superspace. The horizontal line represents the three-dimensional real space \mathbf{R}_3 consisting of direct space lattice vectors \mathbf{a}_1 , \mathbf{a}_2 and \mathbf{a}_3 . Lattice vectors defining the (3+1)-dimensional superspace are \mathbf{a}_{s1} , \mathbf{a}_{s2} , \mathbf{a}_{s3} and \mathbf{a}_{s4} . In general, relation between direct and reciprocal lattice vectors is given by,

$$\mathbf{a}_{si}^* \cdot \mathbf{a}_{sj} = \delta_{ij} \quad (2.4)$$

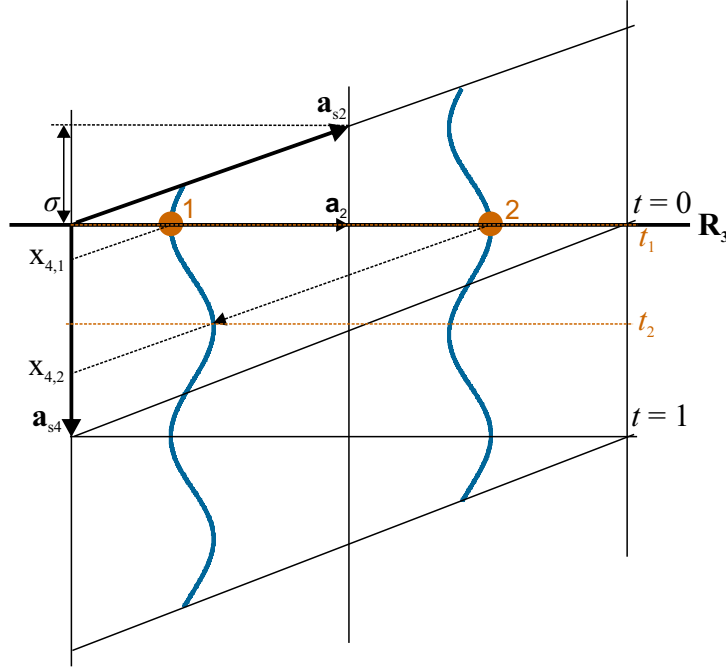


Figure 2.4: A schematic representation of an aperiodic crystal structure in real space \mathbf{R}_3 cut from a periodic structure in (3+1)-dimensional superspace. The horizontal bold line represents real space. The positions of the atoms (orange) in the two consecutive unit cells are 1 and 2 which are three-dimensional sections at $t = t_1$ and t_2 from (3+1)-dimensional superspace at points $x_{4,1}$ and $x_{4,2}$. Further explanation can be found in text.

$\delta_{ij} = 1$ for $i = j$ and zero otherwise. Applying this relation the superspace lattice vectors can be defined as is given by (with respect to eq. 2.3)

$$\begin{aligned}
 \mathbf{a}_{s1} &= (\mathbf{a}_1, -\mathbf{q} \cdot \mathbf{a}_1) = (\mathbf{a}_1, 0) \\
 \mathbf{a}_{s2} &= (\mathbf{a}_2, -\mathbf{q} \cdot \mathbf{a}_2) = (\mathbf{a}_2, -\sigma) \\
 \mathbf{a}_{s3} &= (\mathbf{a}_3, -\mathbf{q} \cdot \mathbf{a}_3) = (\mathbf{a}_3, 0) \\
 \mathbf{a}_{s4} &= (0, 1)
 \end{aligned} \tag{2.5}$$

General position vector of the atom in (3+1)-dimensional superspace is

$$\mathbf{x}_s = \bar{x}_{s1} \mathbf{a}_{s1} + \bar{x}_{s2} \mathbf{a}_{s2} + \bar{x}_{s3} \mathbf{a}_{s3} + \bar{x}_{s4} \mathbf{a}_{s4} \tag{2.6}$$

Relation between \bar{x}_{s4} and phase of the modulation wave t is given by

$$\bar{x}_{s4} = t + \mathbf{q} \cdot \bar{\mathbf{x}} \tag{2.7}$$

where \bar{x} is position vector in the basic structure. In the present case, the relation reduces to

$$\bar{x}_{s4} = t + (\sigma \mathbf{a}_2^*) \cdot (x_1 \mathbf{a}_1 + x_2 \mathbf{a}_2 + x_3 \mathbf{a}_3) = t + \sigma x_2 \quad (2.8)$$

The atoms in (3+1)-dimensional superspace can be thought as one-dimensional strings (in comparison to discrete point objects in three-dimensions) modelled by atomic modulation functions. These strings representing the atoms are periodic along \mathbf{a}_{s4} . In Fig. 2.4, two three-dimensional sections at t_1 and t_2 are cut at atomic positions $x_{4,1}$ and $x_{4,2}$ (the spacing between $x_{4,1}$ and $x_{4,2}$ is equal to σ). In three-dimensions these atoms are represented by point ‘1’ and ‘2’ which are the atomic positions in two consecutive unit cells.

Modulations can be modulation of atomic positions (displacive), modulation of ADPs, modulation of occupancies of atoms, modulation of charge and modulation of spin. In Fig. 2.4, the continuous blue line showing displacive modulation of atom ‘ μ ’ has been modelled using harmonic wave function. Such harmonic wave functions can be written as,

$$f_i^\mu(\bar{x}_{s4}) = x_i^0 + \sum_{n=1}^{\infty} \left(A_i^n \sin(2\pi n \bar{x}_{s4}) + B_i^n \cos(2\pi n \bar{x}_{s4}) \right) \quad (2.9)$$

$i=1,2,3$ representing three dimensions. x_i^0 represents the basic position of the atom ‘ μ ’. n refers to the order of the harmonic wave. A_i^n and B_i^n represent the Fourier coefficients that define the modulation functions of the atom μ . In the present example, one harmonic wave ($n = 1$) is used and in Fig. 2.4, $A_1^1 = 0.0151$ and $B_1^1 = -0.0064$.

Likewise classical three-dimensional crystals, higher symmetry of aperiodic crystals is derived from their diffraction pattern. At first point group symmetry valid for both the main and satellite reflections is determined and then superspace group symmetry is found by analysis of the systematic absences.

Consider the point group symmetry to be monoclinic \mathbf{b} -unique and a superspace group $P2(0\sigma)s$, No. 3.1.5.4 (standard setting. $P2(00\sigma)s$ in Stokes et al. (2011); van Smaalen et al. (2013)) is used to describe the diffraction data. The symmetry equivalent positions in superspace are

$$\begin{array}{l} 1 : \quad \bar{x}_{s1} \quad \bar{x}_{s2} \quad \bar{x}_{s3} \quad \bar{x}_{s4} \\ 2 : \quad -\bar{x}_{s1} \quad \bar{x}_{s2} \quad -\bar{x}_{s3} \quad \bar{x}_{s4} + \frac{1}{2} \end{array} \quad (2.10)$$

The modulation wave vector, $\mathbf{q} = (0, \sigma, 0)$ is parallel to reciprocal lattice vector \mathbf{a}_2^* which means parallel to the twofold rotation axis. \mathbf{q} remains invariant under the rotational symmetry operator 2_y (eq. 2.11).

$$\begin{pmatrix} -1 & 0 & 0 \\ 0 & 1 & 0 \\ 0 & 0 & -1 \end{pmatrix} \cdot \begin{pmatrix} 0 \\ \sigma \\ 0 \end{pmatrix} = \begin{pmatrix} 0 \\ \sigma \\ 0 \end{pmatrix} \quad (2.11)$$

The ‘s’ refers to intrinsic shift of $\frac{1}{2}$ in the internal dimension associated with twofold rotation axis parallel \mathbf{a}_2 . This means a 2_1 screw axis in the internal dimension.

Let us revisit the crystal structure of the present example. As it is a incommensurately modulated crystal structure, each value of t from 0 to 1 has physical meaning. Consider the commensurate modulation case as discussed in the previous subsection ($\sigma = \frac{1}{2}$). In such case, the modulation wave vector has period equal to $2\mathbf{a}_2$. Two three-dimensional sections equidistant by $\Delta t = \frac{1}{2}$ are relevant. The argument of the atomic modulation function at these two equidistant t -sections will be equal to the displacements of the atoms from the basic position in the corresponding twofold superstructure.

In the course of the next three examples, origin of modulation in molecular crystals and advantages of description of superstructures within the (3+1)-dimensional superspace approach are demonstrated.

2.1.3 Examples

Biphenyl

Biphenyl, $C_{12}H_{10}$ has two phenyl rings connected by C–C single bond (Fig. 2.5). In the gas phase, the dihedral angle between the two phenyl rings is reported to be about 42 deg (Bastiansen, 1949), in solution the dihedral angle is estimated to be 32 deg (Eaton and Steele, 1973) and in the solid state at room temperature the complete molecule is planar (Trotter, 1961). In both gas and solution phase, the mutual rotation of the phenyl rings are a result of reducing steric hindrance between the ortho hydrogen atoms. The room temperature crystal structure is described in monoclinic (**b**-unique) space group $P2_1/a$. The complete molecule was found to be planar and the ortho hydrogens are found displaced away from each other in order

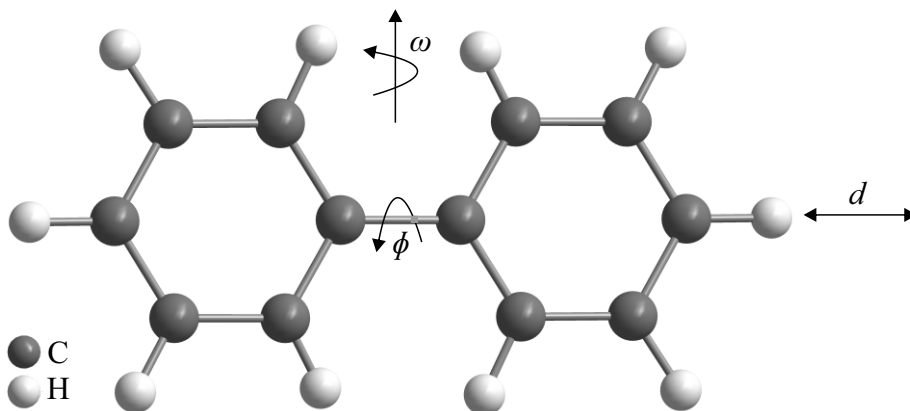


Figure 2.5: A schematic representation of the effect of modulation on the torsion (ϕ), rotation (ω) and displacement (d) of the molecular fragments in biphenyl. Molecule redrawn from [Baudour and Sanquer \(1983\)](#). Modulation scheme redrawn from [Schönleber \(2011\)](#).

to avoid steric interactions ([Hargreaves and Hasan Rizvi, 1962](#)).

Upon cooling, two phase transitions occur at $T_{c1} = 40$ K and $T_{c2} = 21$ K ([Cailleau et al., 1979](#); [Baudour and Sanquer, 1983](#)). Both low temperature phases were identified as incommensurately modulated. In the intermediate phase between T_{c1} and T_{c2} , the modulation wave vector is $\mathbf{q} = 0.05\mathbf{a}^* + 0.46\mathbf{b}^*$. Below T_{c2} , the modulation wave vector is $\mathbf{q} = 0.46\mathbf{b}^*$ ([Baudour and Sanquer, 1983](#)).

Below T_{c2} , the crystal structure was solved within the (3+1)-dimensional superspace approach in superspace group monoclinic (\mathbf{b} -unique) $Pa(0\sigma_20)0$ (No. 7.1.5.3 in [Stokes et al. \(2011\)](#); [van Smaalen et al. \(2013\)](#)) ([Baudour and Sanquer, 1983](#); [Petricek et al., 1985](#); [Schönleber, 2011](#)). Each of the phenyl rings was defined to be planar. Crystal-chemical analysis of the modulated phase revealed three different types of modulation;

1. Modulation of torsion between the phenyl rings along the long molecular axis with an amplitude of $\phi = 5.5$ deg.
2. Modulation of rotation of rigid fragments with an amplitude of $\omega = 1$ deg in a direction normal to the molecular planes, which is out of phase approximately by 90 deg with the modulation of torsion ϕ .
3. Modulation of displacement of the complete molecule of biphenyl along the molecular axis with an amplitude of $d = 0.035$ Å, which is in phase with the

modulation of torsion, ϕ (Baudour and Sanquer, 1983).

With reference to the twisted molecule in the gas phase and the planar molecule at room temperature, the origin of the modulation at low temperature is argued to be a result of competition between the intramolecular and intermolecular forces (Schönleber, 2011); the intermolecular forces responsible for crystal packing favour the biphenyl molecule to be planar while intramolecular interactions (steric interactions) require the phenyl rings to be rotated and twisted with respect to each other.

Adamantan-1-ammonium 4-fluorobenzoate

The crystal structure of adamantan-1-ammonium 4-fluorobenzoate is incommensurately modulated at $T = 97$ K (Schönleber et al., 2014). The compound consists of molecular rigid fragments; the adamantan-1-ammonium cation and the 4-fluorobenzoate anion. The cation and the anion interact *via* N–H \cdots O and C–H \cdots F hydrogen bonds (Fig. 2.6).

The crystal structure is described in monoclinic (**b**-unique) superspace group $P2_1/n(\sigma_1\sigma_3)00$, No. 14.1.2.1 (Stokes et al., 2011; van Smaalen et al., 2013) applying two harmonic waves for displacive and two waves for ADP modulation (Schönleber et al., 2014). The adamantan-1-ammonium cation and the carboxylate anion interact *via* N–H \cdots O hydrogen bonds at the head part of the anion (Fig. 2.6). At the back end of the anion, the fluorine atoms and the cation are involved in weak C–H \cdots F hydrogen bonds (Fig. 2.6).

The N–H \cdots O and C–H \cdots F hydrogen bonding schemes are reported to not vary significantly as function of phase of modulation, t (Schönleber et al., 2014). Due to these intermolecular interactions any displacements of the anion and cation away from each other is unlikely. On the other hand, the contact distances between the hydrogen atoms of the neighbouring phenyl rings along direction [010] are shorter than 2.2 Å which indicates steric interactions between these hydrogen atoms (Rowland and Taylor, 1996). The origin of modulation is argued to be a competition between the optimal conformation of the cations and anions to facilitate these directional intermolecular interactions and the dense packing of cations and anions. Avoidance of steric hindrance between hydrogen atoms of the neighbouring phenyl rings requires the cations and anions to be displaced away from each other, while the

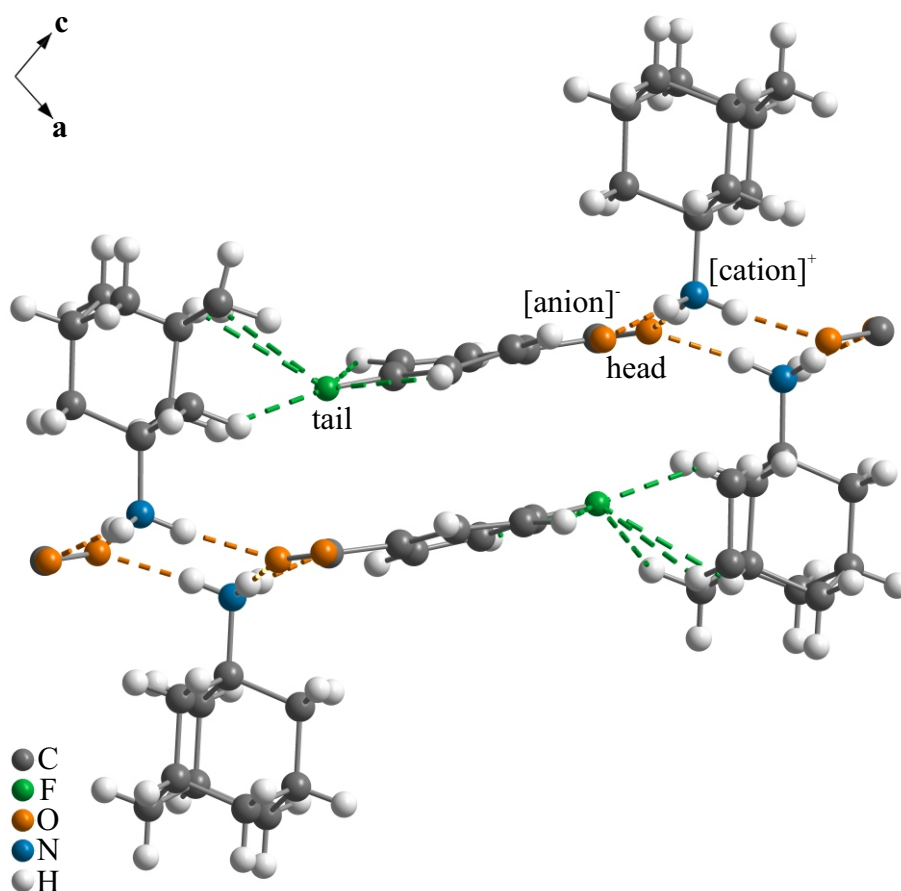


Figure 2.6: Molecules of adamantan-1-ammonium 4-fluorobenzoate interacting *via* N–H···O (dashed orange) and C–H···F (dashed green) hydrogen bonds. Figure redrawn from Schönleber et al. (2014).

rigid scheme of N–H···O and C–H···F hydrogen bonds allows only internal twisting of the 4-fluorobenzoate anions (Schönleber et al., 2014).

p-Chlorobenzamide

p-Chlorobenzamide, C_7H_6ClNO consists of two planar groups (Fig. 2.7); a phenyl ring and an amide group. These two groups are connected by C–C bond. The compound undergoes a phase transition at $T = 317$ K from γ -phase to α -phase upon cooling. The phase transition is reported to be reversible (Takaki et al., 1978; Schönleber et al., 2003). The γ -form can be differentiated from the α -form from

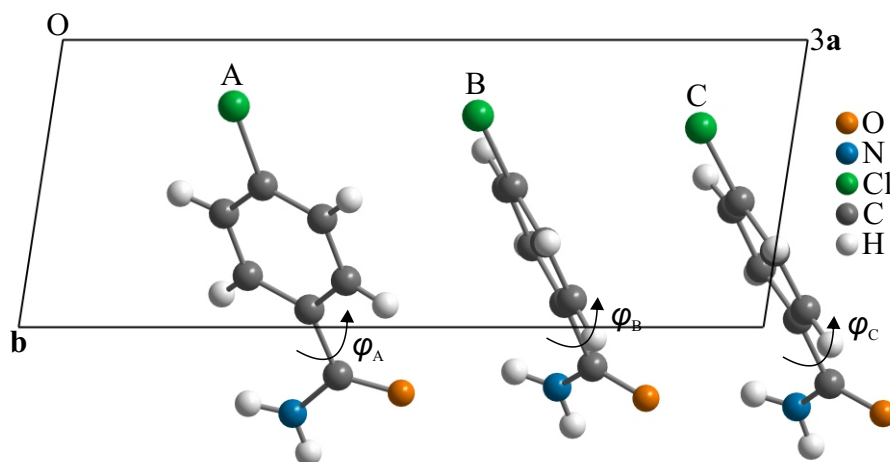


Figure 2.7: The three crystallographically independent units of *p*-chlorobenzamide in α -phase exhibiting different spatial orientation in the unit cell. Figure redrawn from Schönleber et al. (2003).

the diffraction pattern; in former the diffraction pattern is identified with only main reflections indexed on a triclinic lattice and in the latter, weaker satellite reflections are observed in addition to the main reflections. The modulation wave vector with respect to a triclinic lattice is $\mathbf{q} = \frac{1}{3}\mathbf{a}^*$. The crystal structure is described as commensurately modulated structure within the (3+1)-dimensional superspace formalism in superspace group $P\bar{1}(\sigma_1\sigma_2\sigma_3)$ No. 2.1.1.1 (Stokes et al., 2011; van Smaalen et al., 2013). The asymmetric unit in the commensurate model consists of one molecule of C_7H_6ClNO . First order harmonic wave for displacive and anisotropic ADPs for all atoms are used to describe the modulation of the molecule. For sake of comparison, the crystal structure is also described as a threefold superstructure in triclinic space group $P\bar{1}$. The asymmetric unit in the superstructure consists of three molecules. Both structural models give similar results with respect to the fit to the diffraction data (Schönleber et al., 2003). The unit cell of the superstructure comprises of three crystallographically independent molecules of *p*-chlorobenzamide ($Z' = 3$) (Fig. 2.7). The torsion angles between the planes of the phenyl rings and the amide groups of these three molecules are $\phi_A = 19.0$ deg, $\phi_B = 33.9$ deg and $\phi_C = 28.6$ deg. The advantage of the superspace approach over the three-dimensional approach is found to lie in the description of the basic structure of modulated structure. The basic structure model of the α -form was found to be equal to the structural model

of the γ -form. The average torsion angle between the planes of the phenyl rings and the amide groups of the three molecules in the superstructure is 27.3 deg which is the torsion angle in the γ -form and of the basic structure in the α -form. The phase transition thus was concluded as a loss or gain of modulation depending on the direction of change in temperature (Schönleber et al., 2003).

2.2 Structural phase transitions

2.2.1 General overview

Phase transitions in crystals can be classified into continuous and discontinuous transitions owing to the nature of change of structural parameters and internal energy at the transition temperature. Continuous phase transitions are of reversible nature. At a discontinuous phase transition, at least two phases coexist in an equilibrated state. This is understood from the irreversible nature of this type of phase transitions often showing hysteresis.

Structure analysis serves as an important part in understanding phase transition scheme in crystals. One of the tasks is to study thermal expansion of lattice parameters as function of temperature using diffraction techniques and then find out any discontinuity or anomaly in these parameters at some critical temperatures (T_c). Another task is to analyze peak profile as function of temperature to find out say possible peak splitting which indicates symmetry lowering. For incommensurately and commensurately modulated phases, in addition to the lattice parameters, length and direction of the modulation wave vector serves a critical parameter in identifying T_c . After confirming T_c , one has to perform complete data collection at temperatures above and below T_c . Then complete crystal structure analysis has to be performed to find out changes in atomic configurations as result of the phase transition.

In case of continuous (second order) phase transitions, lattice parameters do not show discontinuities upon heating or cooling. Changes in atomic configurations are subtle and phases have group-subgroup relations. Such phase transitions can be understood by atoms present at an equilibrium position at the high symmetry phase gets more degrees of freedom in the low symmetry phase to displace away from the equilibrium position.

Discontinuous (first order) phase transition in crystals can be understood in

terms of discontinuities in lattice parameters and/or atomic configurations and/or absence of group-subgroup relations. Discontinuities in atomic configurations can be of reconstructive nature which can be understood by breaking of chemical bonds. In such case, phases above and below T_c do not have group-subgroup relations.

2.2.2 Modulated phases

In section 2.1, identification of modulated phases from diffraction patterns and the origin of modulation in molecular crystals are already explained. In the course of the next two examples phase transitions from classical three-dimensional periodic phases to modulated phases and modulated to modulated phases in molecular crystals on the basis of diffraction techniques and structural changes are briefly explained.

Hexamethylenetetramine suberate

Hexamethylenetetramine suberate, $N_4(CH_2)_6 \cdot (CH_2)_6(COOH)_2$ consists of two molecules hexamine and suberic acid. The compound can be described as layer structure where the molecules are linked by alternating N–H...O and O–H...N hydrogen bonds (Fig. 2.8).

Temperature dependence of the lattice parameters and the modulation wave vector revealed a phase transition at $T = 300$ K (Bussien Gaillard et al., 1996). Above $T = 300$ K the components of the modulation wave vector is commensurate in character ($\mathbf{q} = \frac{1}{4}\mathbf{c}^*$). (Fig. 2.9(a)). Below $T = 300$ K the compound undergoes commensurate to incommensurate phase transition. At $T = 295$ K the modulation wave vector is reported to be $\mathbf{q} = -0.035(5)\mathbf{a}^* + 0.241(5)\mathbf{c}^*$ (Fig. 2.9(b)). Upon further cooling components of modulation wave vector are found invariant (Bussien Gaillard et al., 1996).

Superspace group (monoclinic \mathbf{b} -unique) $P2_1(\sigma_1 0 \sigma_3)0$ (No. 4.1.2.1 in Stokes et al. (2011); van Smaalen et al. (2013)) was used for the description of the structural model at $T = 295$ K (Bussien Gaillard et al., 1996). The phase transition from commensurate to incommensurate at $T = 300$ K is driven by major changes in the scheme of intermolecular interactions. In the commensurate phase above $T = 300$ K, the three layers A, B and C of hexamethylene tetramine and suberic acid are connected by hydrogen bonds. This hydrogen bonds are absent in the fourth layer D (Fig. 2.8). Below $T = 300$ K with the development of incommensurability in the

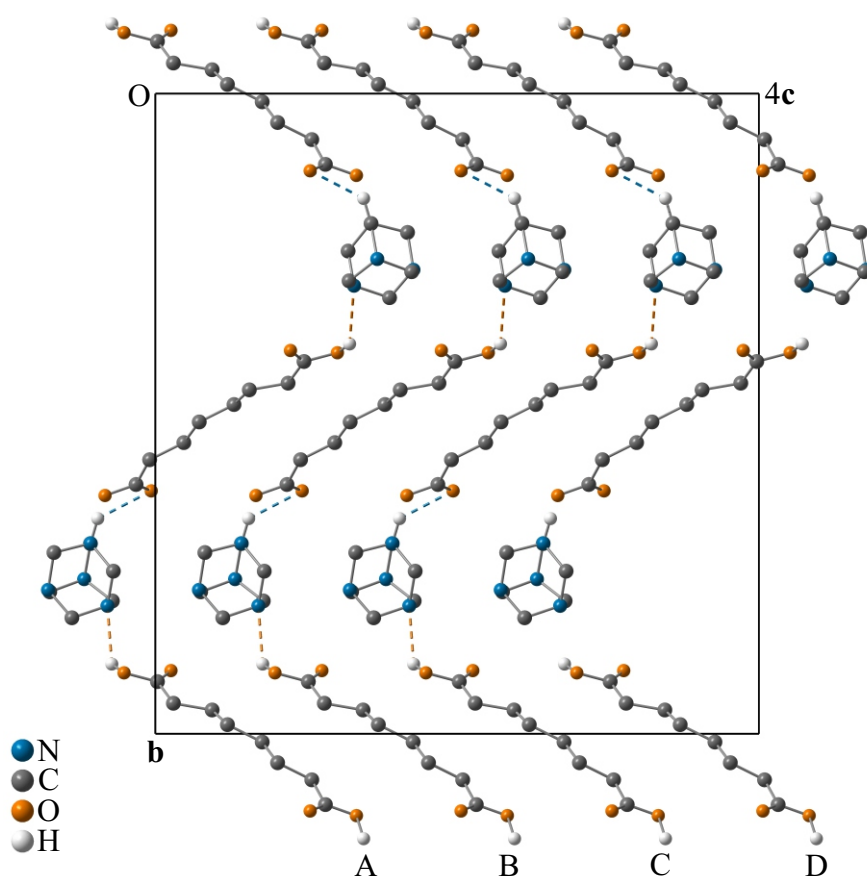


Figure 2.8: The fourfold superstructure approximation of hexamethylenetetramine suberate along c showing the alternating $N-H\cdots O$ (dashed blue) and $O-H\cdots N$ (dashed orange) hydrogen bonds between hexamine and suberic acid. A, B, C and D represent the four layers. Figure redrawn from [Bussien Gaillard et al. \(1996\)](#).

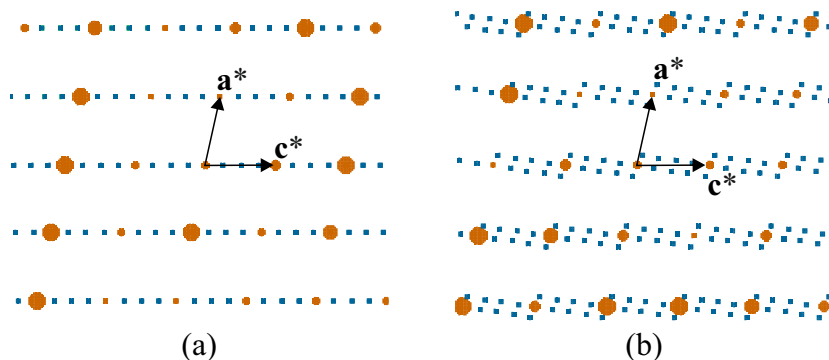


Figure 2.9: Simulated $h0l$ planes of the diffraction pattern of hexamethylenetetramine suberate at (a) $T = 352$ K, (b) $T = 295$ K. The main reflections are drawn in red and the satellites in blue. The simulations are generated from [Bussien Gaillard et al. \(1996\)](#) using JANA2006.

crystal structure, relative orientations of the two molecular fragments change. The hexamine molecule is found strongly modulated along \mathbf{b} (up to 1 \AA) while it is weaker along the other directions. On the other hand, amplitudes of modulation of the suberic acid molecule are approximately equal along all directions. Such difference facilitate formation of the hydrogen bonds within all the layers ([Bussien Gaillard et al., 1996](#)).

The commensurate to incommensurate phase transition (modulation wave vector develops additional component along \mathbf{a}^*) is argued to lie in these molecular fragments twisting themselves in order to achieve long range order of such intermolecular interactions ([Pan et al., 2001](#); [Pan and Chapuis, 2002](#); [2005](#)).

bis-Propylammonium tetrachlorometallate

The system of bis-propylammonium tetrachlorometallate, $(\text{C}_3\text{H}_7\text{NH}_3)_2\text{MCl}_4$ ($\text{M} = \text{Cd}, \text{Mn}, \text{Cu}$) abbreviated as C3M has attracted special interest because of its richness in phase transitions in solid state ([Kind and Muralet, 1986](#)) and occurrence of more than one incommensurate phase during phase transitions.

These compounds have a perovskite type layered structure which consists of corner shared MCl_6 octahedra in a layer. Perpendicular to these layers double layers of alkylammonium chains are situated (Fig. [2.10](#)). The alkylammonium groups interact with the MCl_6 octahedra *via* $\text{N-H}\cdots\text{Cl}$ hydrogen bonds.

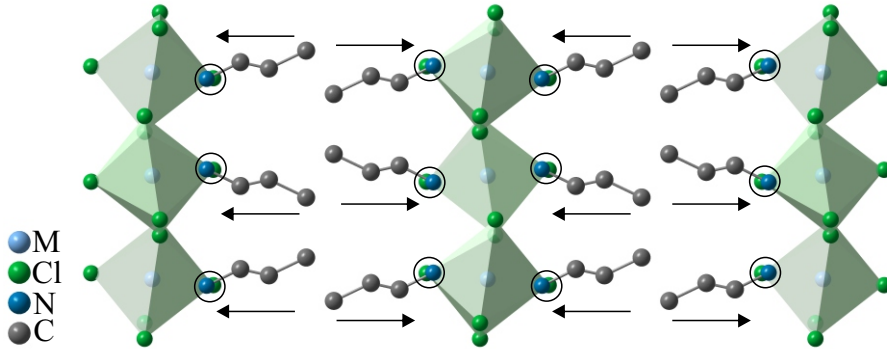


Figure 2.10: A schematic representation of $(\text{C}_3\text{H}_7\text{NH}_3)_2\text{MCl}_4$ showing the alternating MCl_4 and alkylammonium chains. Hydrogen atoms not shown for the sake of clarity. Circles represent the site of the interaction of the alkylammonium chains and the MCl_4 layers. Horizontal arrows represent the direction of displacive modulation of the alkylammonium chains. Figure redrawn from Chapuis (1978).

The C3M show different behavior for different M atoms.

C3Cd, $(\text{C}_3\text{H}_7\text{NH}_3)_2\text{CdCl}_4$ (Fig. 2.11(a)) – The tetragonal α -phase ($\alpha_{(T)}$) undergoes phase transition towards a orthorhombic δ -phase at $T = 450$ K (Chapuis, 1996). The lost fourfold rotation axis serves as the symmetry relation between the two orthorhombic twin domains. At $T = 175$ K the compound undergoes a first-order phase transition confirmed by differential thermal analysis and optical measurements towards incommensurate ε -phase and another first order phase transition towards φ -phase at $T = 150$ K with sudden disappearance of satellite reflections (Chapuis, 1978; Doudin and Chapuis, 1988).

C3Mn, $(\text{C}_3\text{H}_7\text{NH}_3)_2\text{MnCl}_4$ (Fig. 2.11(b)) – In contrast to C3Cd, more phases were detected as function of temperature (Kind and Mural, 1986). The high temperature α -phase ($\alpha_{(T)}$) is described in tetragonal space group $I4/mmm$. At $T = 441$ K the symmetry reduces to orthorhombic $Abma$ towards the β -phase. This phase transition is continuous associated with the propylammonium chains tilting around the \mathbf{a} -axis by 8 deg which are otherwise perfectly aligned in the α -phase. At $T = 388$ K the incommensurate γ -phase was found. The modulation wave vector was reported to be $\mathbf{q} = 0.178\mathbf{a}^* + 0.05\mathbf{b}^*$ (Depmeier, 1981; Mural et al., 1982). At $T = 340$ K, the δ -phase was found. The satellite reflections are not observed in this phase (Chapuis, 1996). At $T = 168$ K the compound undergoes a second-

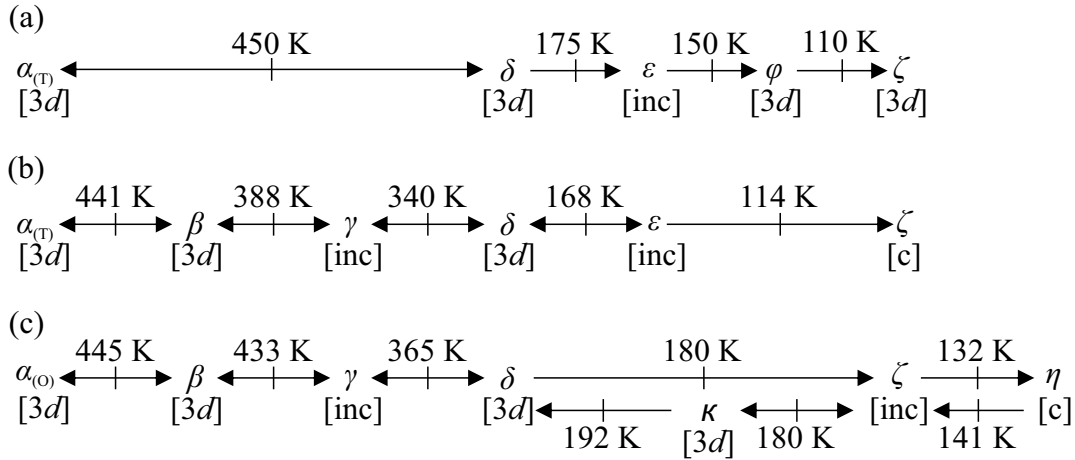


Figure 2.11: A schematic representation of comparisons phase transition schemes of (a) C3Cd, (b) C3Mn and (c) C3Cu as function of temperature. The phase transition temperatures are mentioned on top of the arrows. Both sided arrows represents reversible phase transitions while single side arrows not. [3d] – diffraction pattern with only main reflections, [inc] – diffraction pattern with satellite reflections at incommensurate positions and [c] – diffraction pattern with satellite reflections at commensurate positions. Figure redrawn from Chapuis (1996).

order phase transition towards incommensurate ε -phase and the components of the modulation wave vector were found to be $\approx \frac{1}{3}$ along \mathbf{a}^* and \mathbf{b}^* with respect to a quasi tetragonal lattice (Depmeier et al., 1977). Please note that the authors use an alternate orthorhombic setting. A lock-in ζ -phase was found at $T = 114$ K and $\mathbf{q} = \frac{1}{3}\mathbf{a}^* + \frac{1}{3}\mathbf{b}^*$ (Depmeier et al., 1977).

C3Cu, $(\text{C}_3\text{H}_7\text{NH}_3)_2\text{CuCl}_4$ (Fig.2.11(c)) – In contrast to C3Cd and C3Mn, the high temperature α -phase ($\alpha_{(O)}$) of C3Cu is orthorhombic. The distortion of the tetragonal lattice was found to be in the Cu atom displaced out of the centre of the CuCl_6 octahedron (Jahn et al., 1989; Doudin and Chapuis, 1990a). On the other hand, the length of lattice parameters a and b were found to be equal within standard uncertainties. Upon cooling β -phase was found at $T = 445$ K. The lattice parameters a and b were found to be unequal (Jahn et al., 1989; Doudin and Chapuis, 1990a). Below, $T = 433$ K incommensurate γ -phase was found. The modulation wave vector was found to be $\mathbf{q} = 0.175(5)\mathbf{a}^*$ (Doudin and Chapuis, 1990b; Doudin and Heine, 1990, and references therein). Below $T = 365$ K the δ -phase (room temperature phase) appears with complete disappearance of satellite reflections in

the diffraction pattern. In the temperature range $\Delta T = 433\text{--}365$ K the intensities of the satellite reflections increase and then decrease continuously. All these phase transitions are of second order owing to their continuous nature and reversibility. Close to $T = 180$ K the ζ -phase was found accompanied by splitting of the main reflections which indicate distortion of the orthorhombic lattice (Jahn et al., 1994) and formation of two monoclinic twin domains. In addition satellite reflections also appear in the diffraction pattern. Upon heating the satellite reflections disappear at $T = 180$ K but the main reflections are split up to $T = 192$ K. This scheme of phase transition associated with hysteresis and an additional phase (κ) on heating shows that the phase transition is of discontinuous nature (first order). Below, $T = 132$ K the satellite reflections lock-in towards a commensurate η -phase. Heating reveals hysteresis of $\Delta T = 10$ K which shows that the phase transition from ζ - η is discontinuous (Jahn et al., 1994).

The origin of incommensurate γ -phase common to systems C3Mn and C3Cu is argued to be an attempt to accommodate structural features of the adjacent phases β and δ (Chapuis, 1996, and references therein). In the β -phase each of the alkylammonium chains are parallel to each other making fourfold co-ordination with four similar neighbors in a tetragonal packing. In the δ -phase the chains are packed more dense not retaining the tetragonal arrangement (lattice parameter perpendicular to the octahedron layer is shorter by more than 1 Å in comparison to the β -phase). In the intermediate γ -phase the MCl_6 octahedra are weakly modulated. Modulation of the chains are stronger and are out of phase (Fig. 2.10). The origin of modulation can be understood as a competition between the optimal tetrahedral co-ordination of the chains in the β -phase and dense packing in the δ -phase (Chapuis, 1996, and references therein).

The incommensurate ε -phase is common to the systems C3Cd and C3Mn. In this phase the modulation is driven mainly by the MCl_6 octahedra in contrast to γ -phase. The octahedra show modulation of displacive nature normal to its layers and modulation of rotation about the axis parallel to the octahedra layers. Such reorientation of the octahedra facilitates optimal crystal packing with respect to the hydrogen bonds between the octahedra and alkylammonium chains (Chapuis, 1996, and references therein).

2.3 Twinning

2.3.1 Definition and types

In the *International Tables of Crystallography, Volume D: Physical Properties of Crystals* (Hahn and Klapper, 2006) a twin is defined as: ‘An intergrowth of two or more macroscopic, congruent or enantiomorphic, individuals of the same crystal species is called a *twin*, if the orientation relations between the individuals occur frequently and are ‘crystallographic’. The individuals are called twin components, twin partners or twin domains. A twin is characterized by the *twin law*, *i.e* by the *orientation and chirality relation* of the two twin partners, as well as by their contact relation (twin interface, composition plane, domain boundary).’

Growth twins are obtained when a crystal grows with two or more orientations of its lattice from a single nucleus. Such type of twinning can be avoided by variation of thermodynamic conditions during crystal growth procedure or careful mechanical separation of the grains when they are of macroscopic sizes (Giacovazzo et al., 2002; van Smaalen, 2012).

Transformation twins are generated as result of phase transitions. The structure transforms from a state with higher point symmetry towards lower point symmetry. This type of twinning is unavoidable as the domains are of microscopic sizes. Symmetries of the two different phases follow a group subgroup relation. Certain symmetry operations belonging to the point group of the higher symmetry are suppressed during the transition. The low symmetry domains are related to each other by one of the suppressed symmetry elements.

The diffraction pattern of a twinned crystal can be understood as superposition of the diffracted intensities of the individual twin domains (Parsons, 2003). Diffracted peaks of twin domains are rotated, inverted or reflected with respect to each other and the intensities are weighted according to the twin volumes. Cases where reflections from different lattices overlap completely on each other making it impossible to distinguish these reflections are referred to as merohedral twinning. Pseudo-merohedral twin refers to cases where the diffraction pattern exhibits partially overlapped Bragg reflections of different twin domains. Such twinning can be result of a compound undergoing a phase transition with a slight or significant distortion of the lattice.

In both cases of merohedral and pseudo-merohedral twinning diffraction peaks

from different domains either overlap completely or partially all across the diffraction pattern. A third category of twinning exists known as non-merohedral twinning where peaks from twin domains overlap in only certain part of the reciprocal space (Parsons, 2003). This type of twinning is further not discussed as is beyond the scope of this thesis.

2.3.2 Symmetry relations

As mentioned above, twin domains are related by specific symmetry operations known as the twin law. In the course of the next example, symmetry relations between twin domains of transformation nature are explained.

Phenazine-chloranilic acid

Phenazine-chloranilic acid, $C_{12}H_8N_2 \cdot C_6H_2Cl_2O_4$ is a co-crystal of phenazine and chloranilic acid. At room temperature, the paraelectric phase (PE phase) of the compound crystallizes in monoclinic (**b**-unique) space group $P2_1/n$ (Fig. 2.12) (Horiuchi et al., 2005).

The compound undergoes phase transition towards a ferroelectric phase (FE-I) at $T_{c1} = 253$ K upon cooling. During this phase transition the inversion symmetry is lost, the space group symmetry of the crystal structure is $P2_1$ (Horiuchi et al., 2005; Kumai et al., 2007; Gotoh et al., 2007). At $T_{c2} = 147$ K, the compound undergoes another phase transition towards an incommensurate phase (FE-IC) and finally a lock-in transition at $T_{c3} = 137$ K towards a twofold superstructure (Saito et al., 2006; Horiuchi et al., 2009).

Complete crystal-chemical analysis was performed in the FE-I, FE-IC and FE-II phase in order to investigate the structure-property relationship (Noohinejad et al., 2014; 2015). In the FE-I phase the crystal is pseudo-merohedrally twinned. As the crystal symmetry reduces from $P2_1/n$ in the PE phase to $P2_1$ in the FE-I phase the lost symmetry inversion center is described as the twin law (twin domains ‘i’ and ‘ii’ in Fig. 2.12). The inversion symmetry transforms **a** to **-a**, **b** to **-b** and **c** to **-c**. The symmetry relates the indices of pairs of overlapping reflections of the domains ‘i’ and ‘ii’,

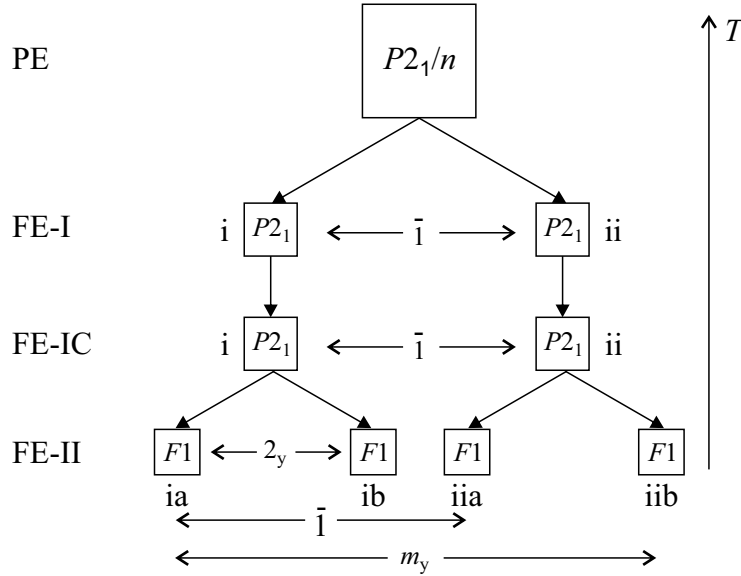


Figure 2.12: A schematic representation of the development of transformation twinning as a result of phase transitions as function of temperature in phenazine-chloranilic acid and the relation between the twin domains (symmetry relation $\bar{1}$ and 2_y and m_y). The boxes are representative of the domains. The space group symmetries of the domains are mentioned inside the boxes. Further explanation can be found in text.

$$\begin{pmatrix} h_{ii} \\ k_{ii} \\ l_{ii} \end{pmatrix} = \begin{pmatrix} -1 & 0 & 0 \\ 0 & -1 & 0 \\ 0 & 0 & -1 \end{pmatrix} \cdot \begin{pmatrix} h_i \\ k_i \\ l_i \end{pmatrix} = \begin{pmatrix} -h_i \\ -k_i \\ -l_i \end{pmatrix} \quad (2.12)$$

The non-centrosymmetric monoclinic symmetry was retained in the FE-IC phase (twin domains ‘i’ and ‘ii’ in Fig. 2.12). Refinement of the twin volumes resulted values equal to 0.5 (Noohinejad et al., 2015).

Crystal symmetry reduces to triclinic in FE-II phase. Four twin domains with twin volumes close to 0.25 were confirmed from structure refinements (Noohinejad et al., 2014). Consider that domain ‘i’ splits into domains ‘ia’ and ‘ib’ and domain ‘ii’ splits into domains ‘iia’ and ‘iib’ (Fig. 2.12(d)). The lost symmetry twofold rotation parallel \mathbf{b} serves as the twin law between domains ‘ia’ and ‘ib’; domains ‘iia’ and ‘iib’.

First consider domains ‘ia’ and ‘ib’. The twofold rotation transforms \mathbf{a} to $-\mathbf{a}$, \mathbf{b} to \mathbf{b} and \mathbf{c} to $-\mathbf{c}$. Indices of the pairs of overlapping reflections are related by the

symmetry operation,

$$\begin{pmatrix} h_{ib} \\ k_{ib} \\ l_{ib} \end{pmatrix} = \begin{pmatrix} -1 & 0 & 0 \\ 0 & 1 & 0 \\ 0 & 0 & -1 \end{pmatrix} \cdot \begin{pmatrix} h_{ia} \\ k_{ia} \\ l_{ia} \end{pmatrix} = \begin{pmatrix} -h_{ia} \\ k_{ia} \\ -l_{ia} \end{pmatrix} \quad (2.13)$$

Let us reiterate the fact that the domain sets $\{ia,ib\}$ and $\{iia,iib\}$ are related by inversion center. The composite symmetry of the inversion center and twofold rotation axis is then a mirror plane perpendicular \mathbf{b} .

$$\begin{pmatrix} -1 & 0 & 0 \\ 0 & -1 & 0 \\ 0 & 0 & -1 \end{pmatrix} \cdot \begin{pmatrix} -1 & 0 & 0 \\ 0 & 1 & 0 \\ 0 & 0 & -1 \end{pmatrix} = \begin{pmatrix} 1 & 0 & 0 \\ 0 & -1 & 0 \\ 0 & 0 & 1 \end{pmatrix} \quad (2.14)$$

This means that if domain ‘ia’ is used as reference, domain ‘ib’ is related to domain ‘ia’ by twofold rotation parallel \mathbf{b} , domain ‘iia’ is related to domain ‘ia’ by the inversion center, and domain ‘iib’ is related to domain ‘ia’ by mirror plane perpendicular \mathbf{b} .

For domains ‘ia’ and ‘iib’ the mirror symmetry will transform \mathbf{a} to \mathbf{a} , \mathbf{b} to $-\mathbf{b}$ and \mathbf{c} to \mathbf{c} . The indices of the pair of overlapping reflections are related by,

$$\begin{pmatrix} h_{iib} \\ k_{iib} \\ l_{iib} \end{pmatrix} = \begin{pmatrix} 1 & 0 & 0 \\ 0 & -1 & 0 \\ 0 & 0 & 1 \end{pmatrix} \cdot \begin{pmatrix} h_{ia} \\ k_{ia} \\ l_{ia} \end{pmatrix} = \begin{pmatrix} h_{ia} \\ -k_{ia} \\ l_{ia} \end{pmatrix} \quad (2.15)$$

2.4 Diffuse scattering and disorder

A classical three-dimensional periodic crystal structure consists of a three-dimensional periodic array of identical units and modulated structures consists of units whose displacement from the basic lattice are argument of a periodic modulation function. In addition to sharp Bragg peaks diffraction pattern of crystals can have scattering weaker compared to Bragg peaks all across the diffraction pattern, certain parts of the diffraction pattern, layers which might or might not superpose on Bragg peaks. This type of scattering is known as diffuse scattering. Diffuse scattering occurs whenever a crystal contains disorder or better short range order

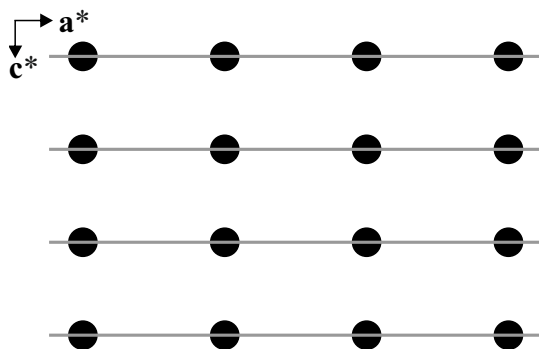


Figure 2.13: A schematic representation of diffuse scattering (grey) and Bragg reflections (black circles) in the diffraction pattern of one-dimensional disordered chain structures. Figure inspired from [Welberry \(2004\)](#).

and also due to thermal vibrations of atoms at finite temperatures ([Willis, 2006](#); [Jagodzinski and Frey, 2006](#); [Welberry, 2014](#); [Welberry and Weber, 2015](#)).

A brief description of diffuse scattering in layers in the context of Me_3SnOH and orientational disorder in the context of $\text{Co}(\text{sep})(\text{NO}_3)_3$ is presented. The descriptions follow the argumentations in [Jagodzinski and Frey \(2006\)](#), and references therein).

Disorder in chain structures

Diffuse scattering in layers in the diffraction pattern of disordered chain structures – Consider that chains are completely ordered internally running along \mathbf{c} . Each of these chains is slightly shifted with respect to each other along \mathbf{c} ; this means one-dimensional disorder. Since the diffraction is the Fourier transform of the crystal structure this one-dimensional disorder reciprocates diffuse layers uniformly distributed perpendicular to the \mathbf{c}^* -axis (Fig. 2.13).

Orientalional disorder

Disorder of orientation – Consider there are large voids in a crystal and a molecule considerably smaller in size in comparison to the voids is introduced. Due to large space, the molecule tends to fill up the vacant space and freeze at a number of different orientations in a single site. Another possibility is that the atoms in the molecule have large thermal vibration due to which the molecule is in a sort of frustration state at the equilibrium position. Such frustrations can also lead to

disorder of orientational nature.

Chapter 3

Superspace description of trimethyltin hydroxide at $T = 100 \text{ K}$ ¹

At low temperatures the metalorganic compound trimethyltin hydroxide, $(\text{CH}_3)_3\text{SnOH}$, possesses a commensurately modulated crystal structure, the modulation wave vector can be described as $\mathbf{q} = \frac{1}{2}\mathbf{c}^*$. The crystal structure is studied by analysing single-crystal X-ray diffraction data within the (3+1)-dimensional superspace approach and superspace group $P2_12_12(00\gamma)00s$. The corresponding twofold superstructure has space group symmetry $P2_12_12_1$. The structure is characterized by polymeric chains running along \mathbf{c} , generated by Sn–O–Sn bridges between neighbouring Sn atoms and packed in a distorted hexagonal pattern and linked *via* C–H \cdots O interstrand hydrogen bonds along the (orthorhombic) directions $[110]$ and $[\bar{1}\bar{1}0]$, but not along $[100]$.

3.1 Introduction

The study of modulated molecular (organic and metalorganic) compounds helps to better understand the reciprocity between intermolecular interactions and crystal

¹This Chapter has been published as: Dey, S., Schönleber, A., Mondal, S. and van Smaalen, S. (2016). Superspace description of trimethyltin hydroxide at $T = 100 \text{ K}$, *Z. Kristallogr.* **231**: 427-434.

packing in the solid state. It is not properly understood how the short-range intermolecular interactions between neighbouring molecules produces the long-range order in crystals. For example, computational approaches to crystal structures can predict the crystal structures of relatively simple molecular crystals provided these structures possess translational symmetry (Price, 2014). However, long range order can be periodic as well as aperiodic, resulting in a modulated crystal structure in the latter case (Schönleber, 2011; Siegler et al., 2012; Subashini et al., 2013; Schönleber et al., 2014; Pinheiro and Abakumov, 2015; Zhang et al., 2016).

Superstructures are quite interesting aspirants for that kind of investigation as they have an intermediate position between “classical” and aperiodic structures; they can be described both as (three-dimensional) periodic structures with large unit cells and as commensurately modulated structures applying the superspace approach to a small basic-structure unit cell with modulations (van Smaalen, 2012; Schönleber et al., 2003; Noohinejad et al., 2014). The title compound has drawn our attention as a suitable candidate for a description as modulated structure in superspace: trimethyltin hydroxide, $(\text{CH}_3)_3\text{SnOH}$, was reported to crystallize at room temperature in a superstructure with high Z' , either in an eightfold or in a $2 \times 2 \times 8 = 32$ -fold superstructure (Kasai et al., 1965; Anderson et al., 2011). With respect to the diffraction pattern, it exhibits a considerable amount of weak or even unobserved superlattice reflections (Kasai et al., 1965). Furthermore, Me_3SnOH assumes different molecular conformations in solution and in the solid state. In solution it has a dimeric structure in which two Sn–O groups form a four-membered ring with the $(\text{CH}_3)_3\text{Sn}$ groups having non-planar configuration (Okawara and Yasuda, 1964). In the solid state it is a linear polymer in which the planar $(\text{CH}_3)_3\text{Sn}$ groups are bridged by the O atoms (Okawara and Yasuda, 1964; Kriegsmann et al., 1962). Different conformations in different phases are also observed for biphenyl (Hargreaves and Hasan Rizvi, 1962) and might indicate frustration between intra- and intermolecular interactions in the crystal structure, serving as possible origin for the modulation (Cailleau et al., 1979). Upon cooling Me_3SnOH undergoes a first order phase transition at $T_c \approx 176$ K from the superstructure with high Z' towards a twofold superstructure with $Z' = 1$ (Anderson et al., 2011).

Trimethyltin hydroxide and related compounds have attracted attention because of the extraordinary chemistry. The molecules are not associated *via* hydrogen bonds, but *via* Sn–O–Sn bridges between neighbouring Sn atoms (Kasai et al., 1965;

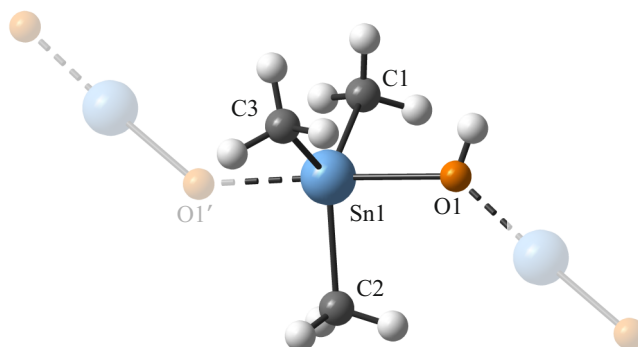


Figure 3.1: Molecular conformation of $(\text{CH}_3)_3\text{SnOH}$, in the crystalline state as part of a polymeric chain, and the atomic labelling scheme, showing the alternating distances $d_{\text{Sn-O}} = 2.20 \text{ \AA}$ and $d_{\text{Sn}\cdots\text{O}'} = 2.22 \text{ \AA}$ along the chain. The molecular graphics has been prepared with DIAMOND (Brandenburg and Putz, 2014).

Kriegsmann et al., 1962), forming a rather stable polymeric chain structure. Such polymeric structures are found also for triphenyltin hydroxide and triphenyllead hydroxide (Glidewell and Liles, 1978), triethyltin hydroxide (Deacon et al., 1993), trimethyltin methoxide (Domingos and Sheldrick, 1974), trimethyltin tetrafluoroborate (Hathaway and Webster, 1963) and trialkyltin formate (Okawara and Ohara, 1964). In a similar way the trimethyltin chloride and trimethyltin bromide form tin–halogen–tin bridges (Kriegsmann and Pischtschan, 1961).

The title compound belongs to the class of metalorganic compounds with a sp^2 hybridized metal centre (Stone and West, 1967). One molecule, or better one formula unit Me_3SnOH , consists of the tin atom bonded to three methyl groups and one hydroxy group. In the crystal structure the tin atom and the carbon atoms of the methyl groups form a trigonal planar conformation with the Sn–O bond being perpendicular to this plane (Fig. 3.1). The tin atoms of neighbouring molecules are associated *via* Sn–O–Sn bridges forming chains with almost equidistant Sn–O bonds ($d \approx 2.2 \text{ \AA}$), resulting in a slightly distorted trigonal bipyramidal coordination of the tin atom. These chains are along the crystallographic *c*–axis, the intensity distribution in the diffraction pattern proposes them to be 8_3 helix-like molecular chains. The Sn–O–Sn angles along the chains are about $\angle \approx 140^\circ$ (Anderson et al., 2011). The structure of the room temperature phase contains one or four such independent polymeric strands, depending on the model as an eightfold or as a 32-fold superstructure (Kasai et al., 1965; Anderson et al., 2011).

In 2004 a structural model for the low temperature structure at $T = 150$ K in orthorhombic non-centrosymmetric space group $P2_12_12_1$ was deposited as data base entry (Parsons et al., 2004) in the CAMBRIDGE STRUCTURAL DATABASE (Groom et al., 2016), but not further discussed. More recently, in 2011, a model in monoclinic centrosymmetric space group $P2_1/c$ for $T = 120$ K was published by another group (Anderson et al., 2011) as twofold superstructure. In contrast to the helical arrangement of the chains in the room temperatures phase, at low temperature the chains are reported to be planar (with respect to the tin and oxygen atoms, which form *zig-zag* chains) and twofold disordered in the monoclinic model.

In the present contribution the low temperature phase of trimethyltin hydroxide, $(\text{CH}_3)_3\text{SnOH}$, is considered and a structural model is proposed within the (3+1)-dimensional superspace approach (van Smaalen, 2012; Janssen et al., 2007). Describing a three-dimensional periodic superstructure as a commensurately modulated structure in superspace has the advantage of establishing a straightforward structural relation between phases at different temperatures (Schönleber et al., 2003; Noohinejad et al., 2014). The superspace model is refined against single-crystal X-ray diffraction data measured at $T = 100$ K with synchrotron radiation in orthorhombic superspace group $P2_12_12(00\gamma)00s$, No. 18.1.9.2 (Stokes et al., 2011; van Smaalen et al., 2013), resulting in space group $P2_12_12_1$ for the twofold superstructure. A superspace approach to the room temperature phase as well as the relation between both phases will be discussed elsewhere.

3.2 Experimental

3.2.1 Data collection

Single-crystals of Me_3SnOH were obtained from Alfa Aesar (98% purity). As the crystals are moisture sensitive, they were stored under Argon atmosphere at $T \approx 250$ K to prevent decomposition. For diffraction experiments the needle shaped crystals were used as received, no further treatment was applied to the samples.

Single-crystal X-ray diffraction experiments were performed at beamline F1, HASYLAB, DESY (Hamburg, Germany) on a four-cycle kappa geometry diffractometer with MAR-CCD area detector. A complete data collection was done by φ and ω scans with step width of $\Delta = 1^\circ$ per image, different detector settings and exposure

times of $t = 2$ or 16 s (Table 3.1). To keep radiation damage, which was reported by Anderson et al. (2011), as small as possible, to reduce absorption effects and to achieve a high resolution, a short wavelength of $\lambda = 0.55999 \text{ \AA}$ was used. Nevertheless, at the end of the data collection the crystal surface showed indications of decomposition. That the crystal quality suffered during measurement was also seen within the data integration process on the mosaicity correction, the corresponding parameter increased from 0.3 at the beginning to 0.5 at the end of measurement.

An open-flow nitrogen gas Oxford Cryostream cooling device was used to set the temperature of the crystal to $T = 100.0(3) \text{ K}$. Special care was taken while cooling down the crystal. With the phase transition being at $T_c \approx 176 \text{ K}$ a slow cooling rate of 0.5 K/min was chosen in the temperature range $190 \text{ K} > T > 160 \text{ K}$ and a higher rate of 3 K/min above and below this range.

A first inspection of the measured frames showed superstructure reflections of 1st order along the \mathbf{c}^* -axis and diffuse scattering in the planes parallel to the $(\mathbf{a}^*, \mathbf{b}^*)$ -plane defined by the main reflections (Fig. 3.2). As the satellite reflections are not split (Fig. 3.2, top) and as they are positioned on straight lines parallel to \mathbf{b}^* (Fig. 3.2, bottom), it hints towards $\mathbf{q} = \frac{1}{2}\mathbf{c}^*$.

The refinement of the lattice parameters and of the modulation wave vector components (Table 3.1) as well as intensity integration and data reduction were done with the software package EVAL15 (Schreurs et al., 2010). Empirical absorption correction was applied with SADABS (Bruker, 2008).

As the refined angles are equal to 90° within five s.u. and as the refined modulation wave vector components are equal to $(0, 0, \frac{1}{2})$ within five s.u., they point towards orthorhombic symmetry. The reflection conditions $(h, 0, 0, 0) : h = 2n$, $(0, k, 0, 0) : k = 2n$ and $(0, 0, l, m) : m = 2n$ indicate superspace group $P2_12_12(00\gamma)00s$, No. 18.1.9.2 (Stokes et al., 2011; van Smaalen et al., 2013). The averaged intensities $\langle I \rangle$ of the observed main and satellite reflections are in the ratio of $20 : 1$, the averaged significance $\langle I/\sigma(I) \rangle$ of $5 : 4$ indicating a pronounced modulation.

In addition also the orthorhombic setting of the data base entry in symmetry $P2_12_12_1$ (Parsons et al., 2004) and the monoclinic setting of the published superstructure in $P2_1/c$ (Anderson et al., 2011) were tested. The resulting lattice parameters are compared with the published ones in Table 3.2. For the orthorhombic lattice the refinement is based on 3180 reflections, for the monoclinic one it is based on 3202 reflections. In the orthorhombic setting 9607, 10220 (obs, all) reflections are

Table 3.1: Experimental and crystallographic data

Crystal data	
Chemical formula	$(\text{CH}_3)_3\text{SnOH}$
M_r	180.82
Crystal system	Orthorhombic
Superspace group	$P2_12_12(00\sigma_3)00s$
T (K)	100.0(3)
a (Å)	6.65189 (17)
b (Å)	10.6664 (2)
c (Å)	4.14518 (7)
V (Å ³)	294.106(14)
Z	2
Wavevector \mathbf{q}	$(0, 0, \frac{1}{2})$
Commensurate section	$t_0 = 0$
Supercell setting	$\mathbf{a} \times \mathbf{b} \times 2\mathbf{c}$
Supercell spacegroup	$P2_12_12_1$
Radiation type	Synchrotron
Wavelength λ (Å)	0.55999
μ (mm ⁻¹)	2.192
Crystal dimensions (mm ³)	$0.08 \times 0.08 \times 0.35$
Data collection	
Diffractometer	Huber kappa four circle with mar165 CCD
Absorption correction	Empirical, multiscan
T_{\min}, T_{\max}	0.3016, 0.4317
No. of meas., indep. and obs. [$I > 3\sigma(I)$] reflections	9774, 3273, 3174
Main reflections (obs, all)	1609, 1638
Satellite reflections (obs, all)	1565, 1635
R_{int} (obs, all)	0.0192, 0.0192
$(\sin(\theta)/\lambda)_{\max}$ (Å ⁻¹)	0.879
Refinement	
$R[F^2 > 2\sigma(F^2)], wR(F^2)$	0.0216, 0.0330
GoF	1.92
No. of reflections	3273
No. of parameters	50
No. of restraints	2
H-atom treatment	mixed
$\Delta\rho_{\max}, \Delta\rho_{\min}$ (e Å ⁻³)	1.57, -1.00
Twin volumes (1, 2)	0.70(4), 0.30(4)

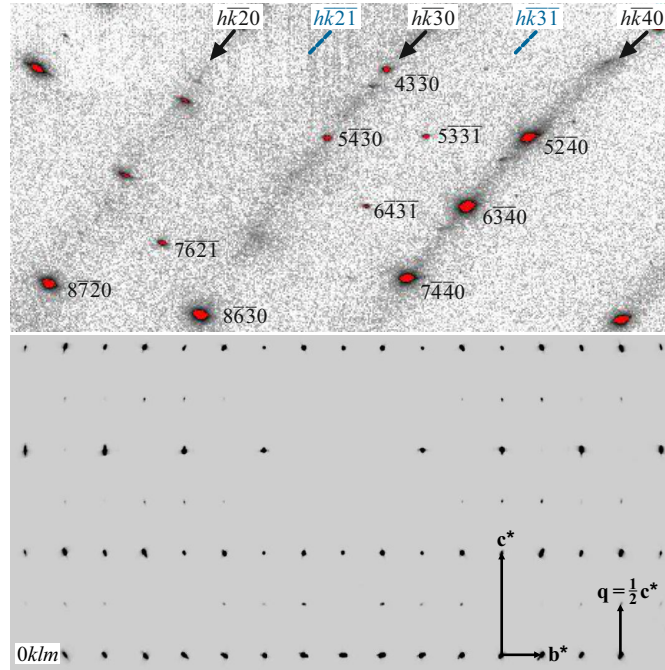


Figure 3.2: Sections of a measured frame (top) and of the reconstructed reciprocal layer $0klm$ (bottom) exhibiting strong main reflections ($hklm$ with $m = 0$) and weaker superstructure reflections ($|m| = 1$) between those along \mathbf{c}^* as well as pronounced diffuse scattering in the layers defined by the main reflections (top, indicated with black arrows). The reconstruction has been calculated with CRYBALISPRO (Rigaku Oxford Diffraction, 2015).

measured, 16, 74 (obs, all) reflections were rejected as systematically extinct in space group $P2_12_12_1$; averaging of the observed reflections results in $R_{\text{int}} = 0.0334$. In the monoclinic setting 9601, 10243 (obs, all) reflections are measured, 401, 537 (obs, all) reflections were rejected as systematically extinct in space group $P2_1/c$; averaging of the observed reflections results in $R_{\text{int}} = 0.0333$. As for the present data the monoclinic angle is equal 90° within one standard uncertainty (Table 3.2) and as a large number of observed reflections contradict to monoclinic symmetry $P2_1/c$, the treatment of the data as a twofold superstructure favours the orthorhombic model and supports the derived orthorhombic superspace group in higher-dimensional space.

Table 3.2: Lattice parameters for the different monoclinic and orthorhombic models at low temperature. For sake of comparison all data were transformed into a common setting.

	Anderson (Anderson et al., 2011)	this work	Parsons (Parsons et al., 2004)	this work
T [K]	120	100	150	100
Symmetry	$P2_1/c$	$P2_1/c$	$P2_12_12_1$	$P2_12_12_1$
a [Å]	6.6883(13)	6.6575(1)	6.6636(18)	6.6599(1)
b [Å]	10.793(2)	10.6755(2)	10.8181(19)	10.6797(1)
c [Å]	8.3828(17)	8.2969(1)	8.317(2)	8.3003(1)
α [°]	90.130(3)	89.9999(13)	–	–
V [Å ³]	605.1(2)	589.68(2)	599.6(2)	590.36(1)

3.2.2 Structure solution and refinement

The crystal structure was solved within the incommensurate approximation in (3+1)-dimensional superspace, by applying the charge flipping algorithm Palatinus (2013) with the program SUPERFLIP (Palatinus and Chapuis, 2007). In the resulting density map the position of the Sn atom was identified by the automatic peak search procedure performed with JANA2006 (Petricek et al., 2014) together with the parameters of a displacive modulation described by continuous atomic modulation functions (AMFs) with harmonic waves of first order. The refinement of this single-atom model with isotropic ADPs converged at $R_F^{\text{obs}}(\text{main}) = 0.0743$ for the main reflections and $R_F^{\text{obs}}(\text{sat}) = 0.3287$ for the satellite (or superstructure) reflections.

In the next step the O and C atoms were added applying Fourier synthesis and finding atomic positions and starting values for the AMFs by analysing the difference Fourier maps ($R_F^{\text{obs}}(\text{main}) = 0.0664$ and $R_F^{\text{obs}}(\text{sat}) = 0.2791$). However, any approach applying continuous harmonic waves as AMFs resulted in a non-converging refinement. As the four-dimensional Fourier maps of the O and C atoms indicated discontinuous atomic domains, the AMFs for all atoms were split along the phase of the modulation t into discrete atomic domains described by crenel functions (Petricek et al., 2016) with width $\Delta = 1/2$ along x_4 . Those crenel functions together with their symmetry equivalents along x_4 represent the two different atomic positions of the atoms in the twofold superstructure, the corresponding symmetry operation being the screw axis along internal space parallel \mathbf{c} : $(2^z, s) : -x_1, -x_2, x_3, x_4 +$

1/2. To keep the model chemically meaningful, the centres of the crenel functions were refined with the constraint to show the same phase of the modulation t by appropriate equations ($R_F^{\text{obs}}(\text{main}) = 0.0459$ and $R_F^{\text{obs}}(\text{sat}) = 0.0879$).

Then anisotropic ADPs were introduced for all atoms and H atoms with isotropic ADPs were attached to the C atoms *via* riding model at calculated positions, keeping tetrahedral geometry, $d_{\text{C-H}} = 0.96 \pm 0.01 \text{ \AA}$ and $U_{\text{H}}^{\text{iso}} = 1.5 U_{\text{C}}^{\text{eq}}$. The H atom of the hydroxyl group was added to the O atom at an arbitrary position, then this position was refined applying the distance and angle restraints $d_{\text{O-H}} = 0.82 \pm 0.01 \text{ \AA}$ and $\angle(\text{Sn} - \text{O} - \text{H}) = 110 \pm 1^\circ$, keeping again $U_{\text{H}}^{\text{iso}} = 1.5 U_{\text{O}}^{\text{eq}}$. The centres of the crenel functions of the H atoms were constrained to show the same phases of the modulation t as the parent atoms ($R_F^{\text{obs}}(\text{main}) = 0.0395$ and $R_F^{\text{obs}}(\text{sat}) = 0.0686$).

After having established the structural model within the incommensurate approximation, the model was changed to a commensurate setting, equivalent to a $[1 \times 1 \times 2]$ -fold superstructure. As a function of the initial phase of the modulation t_0 the resulting three-dimensional periodic superstructures show orthorhombic symmetry $P2_12_12_1$ for $t_0 = 0$ (or $1/2$) and $t_0 = 1/4$ (or $3/4$), or monoclinic symmetry $P2_1$ (\mathbf{c} -unique) for all other phases, *e.g.* $t_0 = 1/8$. This switching from incommensurate to commensurate resulted in a clear improvement of the statistical parameters (for $t_0 = 0$: $R_F^{\text{obs}}(\text{main}) = 0.0191$ and $R_F^{\text{obs}}(\text{sat}) = 0.0333$, see Table 3.3), providing strong proof for the commensurate character of the modulation. Refinement of the centres of the crenel functions resulted in singularities, therefore those values were fixed and not refined any further.

As seen in Table 3.3, the two refinements for $t_0 = 0$ and $t_0 = \text{general}$ ($= 1/8$) converged at similar statistical parameters; to verify which of both is the more suitable, a harmonic wave of first order for displacive modulation was superposed to the crenel functions in the model for $t_0 = 1/8$, which would define the monoclinic distortion in the structure in case that it is present. However, such refinement suffered from large correlations between parameters, resulting in an oscillating and non-converging refinement. Therefore the monoclinic model was discarded from further analysis.

Finally, due to non-centrosymmetric space group symmetry inversion twinning was tested, the twin volume ratio refined to $0.70(4)/0.30(4)$. As the effect of twinning was marginal, the refinement converged at $R_F^{\text{obs}}(\text{main}) = 0.0191$ and $R_F^{\text{obs}}(\text{sat}) = 0.0328$. Any attempt to refine the isotropic extinction parameter re-

Table 3.3: Statistical parameters for the refinement with different structural models [criterion of observability: $I > 3\sigma(I)$]. For sake of comparison the reflections are processed in monoclinic symmetry for all models, resulting in a total of 5924, 6140 (obs, all) reflections, 3000, 3074 main and 2924, 3066 satellite reflections of first order.

	inc.	$t_0 = 0$	$t_0 = \frac{1}{8}$	$t_0 = \frac{1}{4}$
Space group	–	$P2_12_12_1$	$P2_1$	$P2_12_12_1$
GoF(all)	4.02	1.77	1.77	14.90
R_{obs}	0.0473	0.0235	0.0235	0.1381
$R_{obs,main}$	0.0423	0.0211	0.0211	0.0796
$R_{obs,sat}$	0.0694	0.0339	0.0339	0.3966
$\Delta\rho_{max}$ ($\text{e}\text{\AA}^{-3}$)	2.56	1.56	1.55	14.80
$\Delta\rho_{min}$ ($\text{e}\text{\AA}^{-3}$)	-4.65	-1.01	-1.01	-14.10

sulted in a negative value which is why this correction was not applied in the final refinement.

3.3 Discussion

In the model with commensurate modulation only two points along x_4 have a physical meaning and are related by the screw axis along internal space parallel \mathbf{c} : $(2^z, s) : -x_1, -x_2, x_3, x_4 + 1/2$. The initial phase of the modulation t_0 is chosen as $t_0 = 0$. The AMFs are described by crenel functions with width $\Delta = 1/2$ and the modulation wave vector components are $\alpha = \beta = 0$ and $\gamma = 1/2$. Therefore the relation between x_4 and t simplifies to

$$x_4 = t_0 + \mathbf{q}\mathbf{r} = 1/2z \quad (3.1)$$

The resulting values for the fractional coordinate along the additional dimension $x_{4,\text{Sn1}} = 0.0880$, $x_{4,\text{O1}} = -0.1627$, $x_{4,\text{C1}} = 0.1666$ and the ones for the symmetry equivalent atoms shifted by $1/2$ are indicated in the corresponding higher-dimensional Fourier maps along x_4 (Figs. 3.3 – 3.5) as small open circles. Note that those positions are close to but do not exactly coincide with the centres of the crenel functions, as the latter ones are not refined but fixed to some “arbitrary” values ($x_{4,0} = -0.1600$ for O1 and then correspondingly 0.0907 for Sn1 and 0.1694

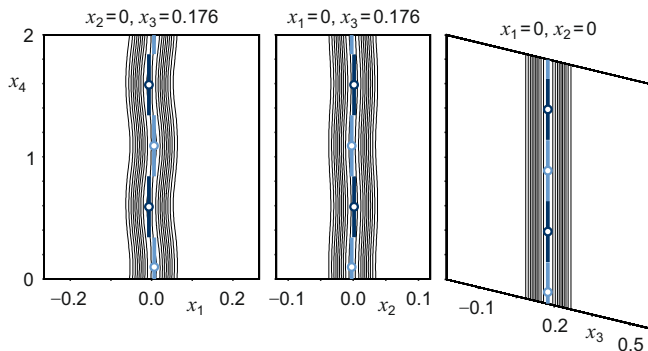


Figure 3.3: Fourier maps along x_4 for atoms Sn1 (light blue) and Sn1^{*i*} (dark blue) with symmetry code (*i*) $-x_1, -x_2, x_3, x_4 + 1/2$. The contour line is $7.5 \text{ e}\text{\AA}^{-3}$, the width of the maps is 3.5 \AA for (x_1, x_4) , 2.5 \AA for (x_2, x_4) and 3.3 \AA for (x_3, x_4) . The higher-dimensional Fourier maps are calculated with JANA2006.

for C1).

Choosing $t_0 = 0$ the resulting twofold superstructure has orthorhombic space group symmetry $P2_12_12_1$ with one formula unit Me_3SnOH in the asymmetric unit and four formula units in the supercell, resulting in two polymeric chains in the unit cell as shown in Fig. 3.6. The chains are separated by van der Waals gaps, the hydrogen distances being with $d_{\text{H-H}} \geq 2.5 \text{ \AA}$ (Table 3.5) clearly above the limit of $d_{\text{min}} \approx 2.2 \text{ \AA}$ for closest $\text{H}\cdots\text{H}$ interactions Rowland and Taylor (1996), and they are related to each other *via* the $(2_1, 0)$ screw axes along **a** and **b**. Each chain shows true screw rotation along internal space parallel **c**: $(2^z, s)$ in the superspace model, corresponding to a 2_1 screw axis along **c** in the twofold superstructure.

With respect to the sp^2 hybridisation of the Sn atom, its configuration should be trigonal bipyramidal with the Sn and the three C atoms defining the basal plane and the O atoms defining the apical corners. However, this trigonal pipyramid is distorted, the two interatomic distances Sn–O deviate from each other by about 0.02 \AA , as the Sn atom is shifted out of the plane defined by the C atoms towards the O atom. All atomic distances and angles are close to but slightly deviate from ideal values (Table 3.4).

The angles $\angle(\text{O}'\cdots\text{Sn}-\text{O})$ are with 177.5° almost linear, while the angles $\angle(\text{Sn}-\text{O}\cdots\text{Sn}'')$ are 139.4° , generating the *zig-zag* arrangement of Sn and O atoms along **c**-axis (Figs. 3.1 and 3.6). Those values are comparable to the ones for triphenyl hydroxide with 177.6° and 137.8° (Glidewell and Liles, 1978) and for triethyl

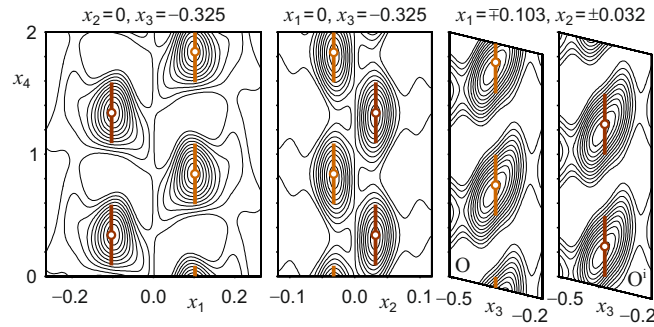


Figure 3.4: Fourier maps along x_4 for atoms O1 (orange) and O1^{*i*} (brown) with symmetry code (*i*) $-x_1, -x_2, x_3, x_4 + 1/2$. The contour line is $0.5 \text{ e}\text{\AA}^{-3}$, the width of the maps is 3.5 \AA for (x_1, x_4) , 2.5 \AA for (x_2, x_4) and 1.5 \AA for (x_3, x_4) . The higher-dimensional Fourier maps are calculated with JANA2006.

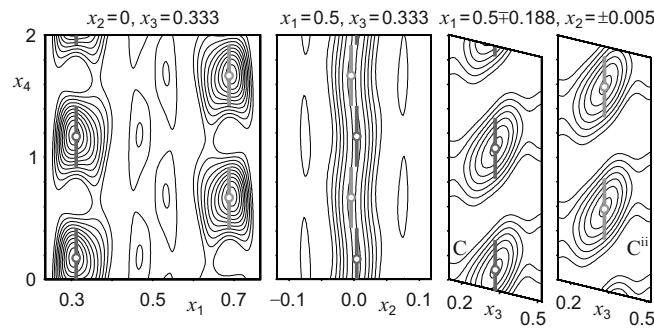


Figure 3.5: Fourier maps along x_4 for atoms C1 (dark gray) and C1^{*ii*} (light gray) with symmetry code (*ii*) $-x_1 + 1, -x_2, x_3, x_4 + 1/2$. The contour line is $0.5 \text{ e}\text{\AA}^{-3}$, the width of the maps is 3.5 \AA for (x_1, x_4) , 2.5 \AA for (x_2, x_4) and 1.5 \AA for (x_3, x_4) . The higher-dimensional Fourier maps are calculated with JANA2006.

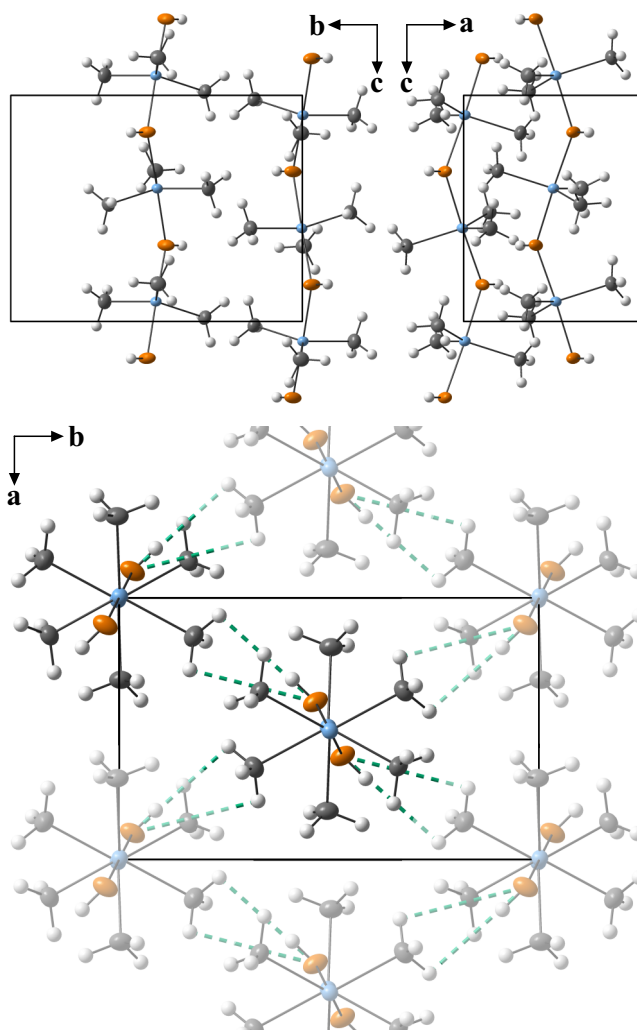


Figure 3.6: Packing of the two polymeric chains in the supercell. Anisotropic ADPs of the non-H atoms are shown at 60% probability ellipsoids. The molecular graphics has been prepared with DIAMOND.

Table 3.4: Interatomic distances (\AA), torsion angles ($^\circ$) and angles ($^\circ$) illustrating the slight distortion of the trigonal bipyramidal co-ordination polyhedron of the tin atom.

Sn–O	2.1985(9)	O–Sn–O ^{<i>i</i>}	177.46(4)
Sn–O ^{<i>i</i>}	2.2229(9)	O–Sn–C1	90.93(4)
Sn–C1	2.1355(13)	O–Sn–C2	89.85(5)
Sn–C2	2.1262(14)	O–Sn–C3	90.62(5)
Sn–C3	2.1343(14)	O ^{<i>i</i>} –Sn–C1	91.32(4)
		O ^{<i>i</i>} –Sn–C2	88.02(5)
C1–C2–C3–Sn1	-0.94(5)	O ^{<i>i</i>} –Sn–C3	89.32(5)
C2–C3–C1–Sn1	-0.91(4)	C1–Sn–C2	119.90(6)
C3–C1–C2–Sn1	-0.92(4)	C1–Sn–C3	118.84(6)
		C2–Sn–C3	121.24(6)

Symmetry operation: (*i*) $-x, -y, z + 1$.

hydroxide with 177.9° and 145.5° (Deacon et al., 1993).

The polymeric strands are forming a two-dimensional pseudo-hexagonal pattern on the (**a**,**b**)-plane (Fig. 3.6, bottom). However, at $b/a = 1.604$ the ratio of the lattice parameters is far from the ideal value of $\sqrt{3} = 1.732$ for the orthohexagonal unit cell, which is reflected in the distances between chains along [110] and [100]. The former are shorter, $d_{\text{Sn-Sn}^i} = 6.415 \text{ \AA}$ and $d_{\text{Sn-Sn}^{ii}} = 6.490 \text{ \AA}$, the latter are longer, $d_{\text{Sn-Sn}^{iii}} = 6.651 \text{ \AA}$ (symmetry codes: (*i*) $x + 1/2, -y - 1/2, -z$; (*ii*) $x + 1/2, -y + 1/2, -z$; (*iii*) $x + 1, y, z$). It is also seen in the shortest H–H distances with $d_{\text{H-H}} = 2.471 \text{ \AA}$ along [110] and $d_{\text{H-H}} = 2.481 \text{ \AA}$ along [100] (Table 3.5). One might explain the orthorhombic distortion by C–H \cdots O hydrogen bonding (Desiraju, 1996; Gu et al., 1999), which can be observed along the directions [110] and $[1\bar{1}0]$, but not along [100] (Fig. 3.7 and Table 3.6).

The diffuse scattering is found in planes perpendicular to the **c**-axis, which is the axis of the polymeric *zig-zag* chains. The origin of this diffuse scattering can be lack of complete order between the chains. For example, different chains might be shifted with respect to each other by different amounts along **c**. Another possibility of disorder might be an arbitrary direction of the *zig-zag*.

Table 3.5: The shortest H–H distances (Å) within a chain [(*i*), (*ii*)] and between chains along **a**-axis [(*iii*)] and along diagonal [(*iv*), (*v*), (*vi*)].

H1c2–H3c3 ^{<i>i</i>}	2.53025(5)	H1o1–H3c3 ^{<i>iv</i>}	2.471(16)
H1o1–H3c2 ^{<i>i</i>}	2.625(12)	H1o1–H1c3 ^{<i>iv</i>}	2.607(15)
H2c1–H2c3 ^{<i>ii</i>}	2.63859(4)	H3c1–H2c3 ^{<i>iv</i>}	2.64190(1)
H1c1–H2c2 ^{<i>iii</i>}	2.4815(2)	H2c2–H3c2 ^{<i>v</i>}	2.5913(2)
H3c1–H1c3 ^{<i>iii</i>}	2.6122(2)	H3c2–H1c3 ^{<i>vi</i>}	2.63348(3)

Symmetry operations: (*i*) $-x, -y, z - 1$; (*ii*) $-x, -y, z + 1$; (*iii*) $x + 1, y, z$; (*iv*) $x + 1/2, -y - 1/2, -z$; (*v*) $x - 1/2, -y + 1/2, -z$; (*vi*) $-x - 1/2, y + 1/2, -z + 1$.

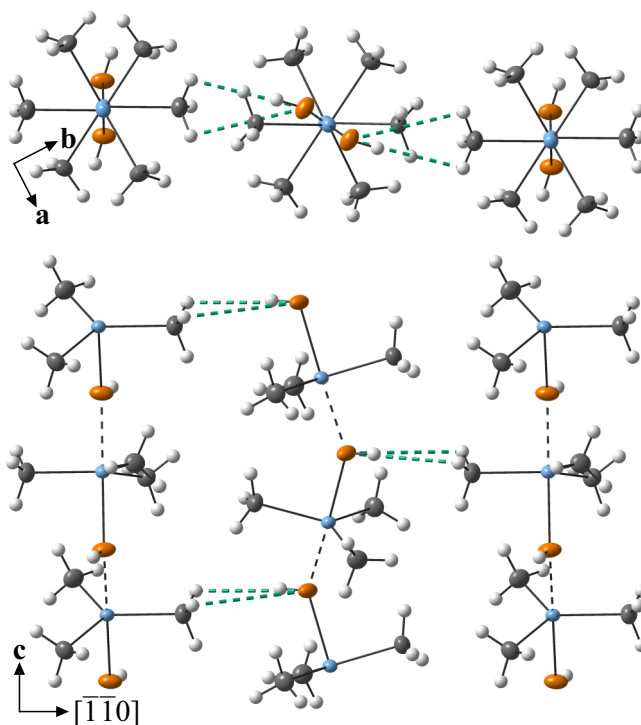


Figure 3.7: The C–H···O interstrand interaction scheme along direction [110]; view above towards plane (001) and below towards ($6\bar{5}\bar{2}$), compare with Figs. 3.1 and 3.6. The molecular graphics has been prepared with DIAMOND.

Table 3.6: Distances [\AA] and angles [$^\circ$] in the interstrand C–H \cdots O hydrogen bonds. The hydrogen positions were calculated *via* riding models to the C atom.

C	H	O	C–H	H \cdots O	C–O	$\angle(\text{CHO})$
C3	H1c3	O1 ^{<i>vii</i>}	0.96	3.2943(1)	3.5650(1)	98.502 (1)
C3	H3c3	O1 ^{<i>vii</i>}	0.96	3.2867(1)	3.5650(1)	98.981 (1)

Symmetry operations: (*vii*) $x - 1/2, -y - 1/2, -z$.

3.4 Conclusion

The twofold superstructure of trimethyltin hydroxide at $T = 100$ K has successfully been described within the superspace approach. In contrast to the recent publication with a monoclinic structure model (Anderson et al., 2011) our data shows orthorhombic symmetry as it was also applied in the earlier data base entry (Parsons et al., 2004).

Next to the H \cdots H van der Waals interactions between the chains (Table 3.5) C–H \cdots O interstrand hydrogen bonds (Fig. 3.7) could be identified, serving as possible force for the packing and the (planar) *zig-zag* arrangement of the polymeric chains.

3.5 Acknowledgements

Assistance of Carsten Paulmann in the diffraction experiments at beamline F1 of Hasylab at DESY, Hamburg is gratefully acknowledged. Financial support has been obtained from the German Science Foundation (DFG) under grant number SCHO 830/3-1.

Chapter 4

Modulated inter-strand C–H···O bonds in the high Z' superstructure of trimethyltin hydroxide

The crystal structure of trimethyltin hydroxide, $(\text{CH}_3)_3\text{SnOH}$ at room temperature has previously been described as a $2\mathbf{a}\times 2\mathbf{b}\times 8\mathbf{c} = 32$ -fold superstructure ([Anderson et al., 2011](#)). Here we report a redetermination of the crystal structure of $(\text{CH}_3)_3\text{SnOH}$ at $T = 220$ K (ambient conditions phase). While the superlattice reflections were observed along \mathbf{c}^* , diffuse scattering was observed at positions of possible superlattice reflections along \mathbf{a}^* and \mathbf{b}^* . Therefore we propose an eightfold, $\mathbf{a}\times\mathbf{b}\times 8\mathbf{c}$ superstructure. The orthorhombic symmetry (space group $P2_1cn$) of this superstructure then leads to $Z' = 4$. The $(\text{CH}_3)_3\text{SnOH}$ monomers are linked *via* Sn–O bonds of nearly equal distances ($2.18 \sim 2.24$ Å) in a chain along \mathbf{c} . In contrast to the proposed 8_3 -helical arrangement of the individual chains in the published superstructure we have found a distorted zigzag arrangement. The origin of this distortion can be explained by steric hindrance between the hydroxy groups and the methyl groups of adjacent $(\text{CH}_3)_3\text{Sn}$ groups. Inter-strand C–H···O hydrogen bonds are found with large variations in H···O distances ($3.15 \sim 3.59$ Å) and C–H···O angles ($95.83 \sim 128.45$ deg).

4.1 Introduction

The origin of multiple copies of a molecule in the asymmetric unit of a molecular crystal ($Z' > 1$ structures) is often argued to be frustrated intermolecular interactions. Intermolecular interactions which lead to competitions in the crystal packing are referred to as ‘synthon frustrations’ (Desiraju, 1995; Anderson et al., 2008). Such frustrations occur when intermolecular interactions favour certain orientations and conformations of the molecules while intramolecular interactions favour another conformation (Brock and Dunitz, 1994; Brock, 1996; Steed, 2003; Desiraju, 2007; Hao et al., 2005; Ramirez-Montes et al., 2014; Taylor et al., 2016). In order to understand the origin of low Z' and high Z' structures arising from variation of reaction conditions and/or phase transitions as function of thermodynamic conditions (Steed, 2003; Desiraju, 2007; Zentner et al., 2015; Reddy et al., 2016; Steed and Steed, 2015) and also to understand possible frustrations, a complete crystal-chemical analysis is very important. Such an analysis can be done in an elegant way by describing the superstructures as commensurately modulated structures within the higher-dimensional superspace approach (Janssen et al., 2007; Wagner and Schönleber, 2009; Schönleber, 2011; van Smaalen, 2012; Pinheiro and Abakumov, 2015). The latter describes the crystal structure by a periodic modulation of the content of a small unit cell. With one molecule in the basic structure unit cell, the modulation describes different modifications to the molecular structure for the independent copies of this molecule in the corresponding supercell. The superspace approach has the advantage that it establishes unique relations between different phases of a compound and also between different compounds which are isomorphous (Schönleber et al., 2003; van Smaalen, 2012; Noohinejad et al., 2015; Dey et al., 2016a), and that it often removes correlations between structural parameters (van Smaalen, 1987; Harris et al., 1994). On the other hand, it is not established that all high Z' structures can necessarily be described as modulated structures (Steed and Steed, 2015).

Trimethyltin hydroxide, $(\text{CH}_3)_3\text{SnOH}$ (Fig. 4.1), exists as a dimer in solution and it is a polymeric compound in the solid state (Kriegsmann et al., 1962). It attracted our attention as the room-temperature phase is reported to crystallize in a 32-fold superstructure ($2\mathbf{a} \times 2\mathbf{b} \times 8\mathbf{c}$ supercell) with monoclinic space group Pn (\mathbf{b} -unique) and $Z' = 32$ (Anderson et al., 2011; Kasai et al., 1965). The published superstructure model (Anderson et al., 2011) consists of four crystallographically

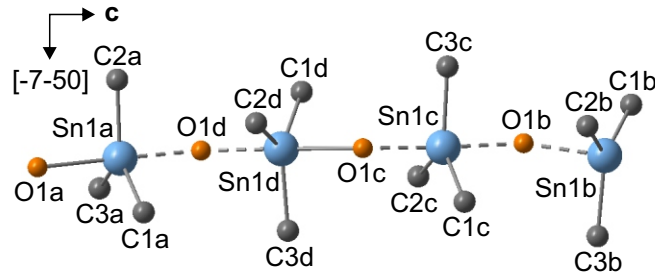


Figure 4.1: Four independent formula units of $(\text{CH}_3)_3\text{SnOH}$ in a chain with the atomic labels derived from the superspace model. Viewing direction along $[2-10]$. Hydrogen atoms are omitted. The molecular graphics has been prepared with DIAMOND (Brandenburg and Putz, 2014).

independent chains, each containing eight independent molecules $(\text{CH}_3)_3\text{SnOH}$, resulting in $Z' = 32$. The chains are slightly distorted with respect to each other. The chains are formed by connecting $(\text{CH}_3)_3\text{Sn}$ groups through oxygen resulting in Sn–O–Sn–O infinite chains with nearly equal Sn–O bond lengths. It was proposed that the molecular conformations within a single chain show 8_3 -helical rotation. (Anderson et al., 2011).

We have performed single-crystal X-ray diffraction experiments at $T = 220$ K. Careful analysis of the diffraction images revealed the absence of superlattice reflections along \mathbf{a}^* and \mathbf{b}^* . Instead, pronounced diffuse scattering has been observed in planes perpendicular to \mathbf{c} containing main reflections. Strong superlattice reflections are observed along \mathbf{c}^* . Hence our data support an eightfold, $\mathbf{a} \times \mathbf{b} \times 8\mathbf{c}$ superlattice. The superstructure is described as a commensurately modulated structure within the (3+1)-dimensional $[(3+1)\text{D}]$ superspace approach. The symmetry is given by the orthorhombic superspace group $P2_1mn(00\sigma_3)0s0$, No. 31.1.9.7 (Stokes et al., 2011; van Smaalen et al., 2013), resulting in the orthorhombic space group $P2_1cn$ for the corresponding eightfold superstructure (Fig. 4.1). The fourfold smaller unit cell together with the higher symmetry result in a reduction of Z' from published (Anderson et al., 2011) 32 towards presently 4. A complete crystal-chemical analysis is done to understand the origin of modulation (distortion) in the chains and the interaction between the chains.

4.2 Experimental

4.2.1 Diffraction experiment and data integration

Single crystals of $(\text{CH}_3)_3\text{SnOH}$ have been obtained from Alfa Aesar (98 % purity). They were used as purchased for our experiments. The crystals were stored in argon atmosphere at $T = 250$ K, because they were found to decompose in air at ambient conditions. Single-crystal X-ray diffraction experiments were performed at beamline F1, Hasylab, DESY, Hamburg, employing a four-circle kappa diffractometer with a MAR-CCD area detector and radiation of wavelength $\lambda = 0.56000$ Å (Table 4.1).

The temperature of the crystal was maintained at $T = 220.0$ (3) K by an open-flow nitrogen-gas cryostat by Oxford Cryosystems. This temperature has been chosen to prevent decomposition of the crystal while still being well above the transition temperature ($T_c \approx 176$ K (Anderson et al., 2011)) towards the low-temperature phase. A complete data collection of diffracted intensities was done by φ and ω scans at different detector positions maintaining a crystal-to-detector distance of $D = 150$ mm (Table 4.1).

Data processing has been performed with the software EVAL15 (Schreurs et al., 2010). In order to reproduce the published $2\mathbf{a} \times 2\mathbf{b} \times 8\mathbf{c}$ superstructure (Anderson et al., 2011), diffraction peaks were indexed on a primitive monoclinic superlattice with refined lattice parameters $2a = 13.2347$ (9) Å, $2b = 22.1139$ (8) Å and $8c = 33.0642$ (15) Å and $\beta = 89.978$ (4) deg. Only 30 observed reflections (with intensities $I > 3\sigma(I)$) were found among 19009 integrated superlattice positions (hkl) with $h = 2n + 1$, and only 75 observed reflections existed among 39896 superlattice positions (hkl) with $k = 2n + 1$. All these 105 observed reflections have $l = 8n$, *i.e.* they occur within the diffuse planes perpendicular to \mathbf{c} containing the main reflections (Fig. 4.2 and supplementary material). These features suggest that these 105 reflections actually are part of the structured diffuse scattering, and they were not used in the further analysis. Superlattice reflections have been found at positions (hkl) with $h = 2n$, $k = 2n$, and $l \neq 8n$ ($l = 8n$ are main reflections; Fig. 4.2 and supplementary material).

In order to describe the eightfold superstructure as a commensurately modulated structure within the (3+1)D superspace approach, diffraction peaks were alternatively indexed by four integers ($hklm$) (Fig. 4.2). This indexing is based on the unit cell defined by \mathbf{a} , \mathbf{b} and \mathbf{c} , and the modulation wave vector $\mathbf{q} = (0, 0, \frac{3}{8})$.

Table 4.1: Experimental and crystallographic data.

Crystal data	
Chemical formula	(CH ₃) ₃ SnOH
M_r	180.82
Crystal dimensions (mm ³)	0.07×0.07×0.30
Crystal system	Orthorhombic
Superspace group	$P2_1mn(00\sigma)0s0$
T (K)	220.0 (3)
a (Å)	6.61986 (19)
b (Å)	11.06277 (31)
c (Å)	4.13537 (15)
V (Å ³)	302.93 (3)
Z	2
Wavevector \mathbf{q}	(0, 0, $\frac{3}{8}$)
Commensurate section	$t_0 = 0$
Supercell	$\mathbf{a} \times \mathbf{b} \times 8\mathbf{c}$
Supercell space group	$P2_1cn$
Radiation type	Synchrotron
Wavelength (Å)	0.56000
μ (mm ⁻¹)	2.128
Diffraction data	
$[\sin(\theta)/\lambda]_{\max}$ (Å ⁻¹)	0.81311
$\Delta\varphi, \Delta\omega$ (deg)	1
Exposure time (s)	2, 16
Crystal-to-detector (mm)	150
Absorption correction	empirical, multiscan
Criterion of observability	$I > 3\sigma(I)$
Unique reflections	
All (obs/all)	5119/10600
$m = 0$ (obs/all)	1180/1377
$m = \pm 1$ (obs/all)	1629/2542
$m = \pm 2$ (obs/all)	1158/2757
$m = \pm 3$ (obs/all)	743/2545
$m = -4$ (obs/all)	409/1379
R_{int} (obs/all)	0.0183/0.0225
Refinement	
GoF (obs/all)	2.16/1.67
$R_{\text{obs}}/wR_{\text{all}}$	
All (obs/all)	0.0438/0.0573
$m = 0$ (obs/all)	0.0270/0.0347
$m = \pm 1$ (obs/all)	0.0484/0.0458
$m = \pm 2$ (obs/all)	0.0880/0.0940
$m = \pm 3$ (obs/all)	0.1143/0.1348
$m = -4$ (obs/all)	0.0711/0.0787
No. of parameters	194
H-atom treatment	mixed
Absolute structure parameter(Flack, 1983)	0.5
$\Delta\rho_{\min}/\Delta\rho_{\max}$ (e/Å ³)	-1.91/1.97

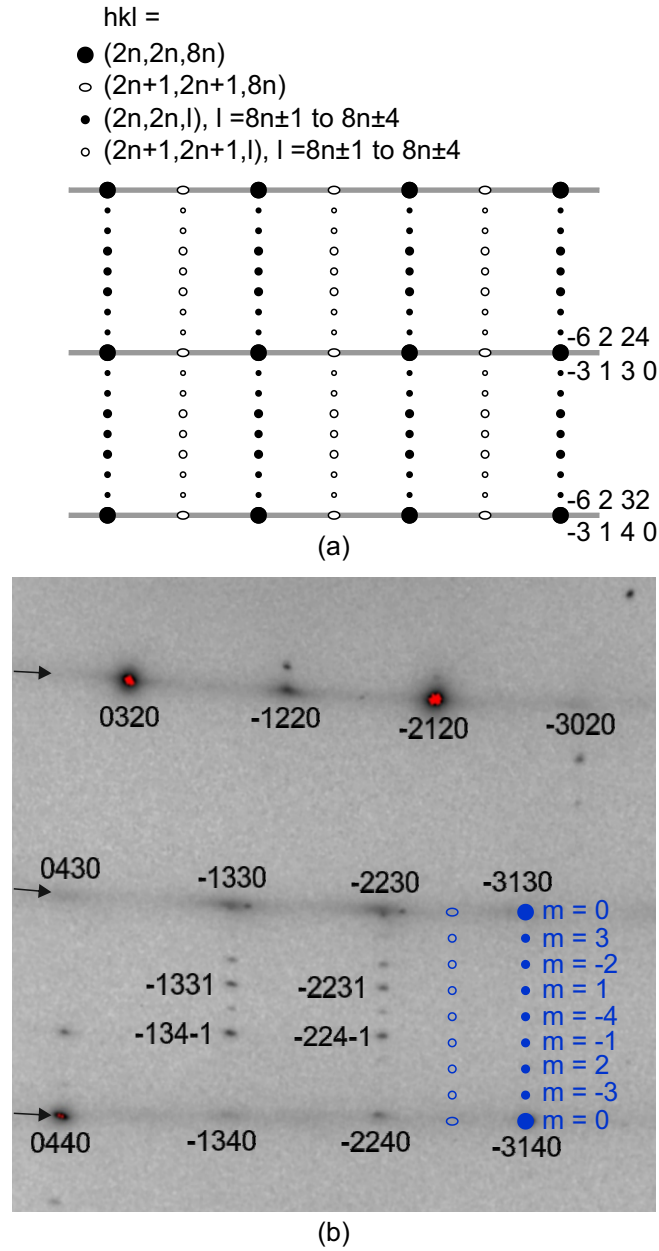


Figure 4.2: (a) Schematic representation of the diffraction image indexed in $2\mathbf{a} \times 2\mathbf{b} \times 8\mathbf{c}$ supercell. Black circles represent observed reflections while open circles and ellipses unobserved ones. The horizontal grey layer represents the diffuse scattering. (b) Section of a measured frame with strong main reflections $((hkl)0)$ and weaker superstructure reflections $(hklm$ with $m = \pm 1, \pm 2, \pm 3, -4)$ indexed in $\mathbf{a} \times \mathbf{b} \times \mathbf{c}$ cell with $\mathbf{q} = \frac{3}{8}\mathbf{c}^*$ along with pronounced diffuse scattering in the layers (shown by arrows) defined by main reflections. (The complete measured frame can be found in the supplementary material).

Free refinement of the lattice parameters led to all angles equal to 90 deg within three times their standard uncertainties, while the non-zero component of \mathbf{q} refined towards 0.374971(10), which is equal to $\frac{3}{8}$ within three standard uncertainties.

Integrated intensities of diffraction peaks were obtained by EVAL15. Absorption correction was performed by SADABS (Bruker, 2008), employing Laue symmetry mmm . The ratio of the average intensities of main and superlattice reflections is $\langle I \rangle_{|m|=0} : \langle I \rangle_{|m|=1} : \langle I \rangle_{|m|=2} : \langle I \rangle_{|m|=3} : \langle I \rangle_{|m|=4} \approx 160 : 16 : 4 : 3 : 8$ and of the average significance is $\langle I/\sigma(I) \rangle_{|m|=0} : \langle I/\sigma(I) \rangle_{|m|=1} : \langle I/\sigma(I) \rangle_{|m|=2} : \langle I/\sigma(I) \rangle_{|m|=3} : \langle I/\sigma(I) \rangle_{|m|=4} \approx 25 : 20 : 9 : 8 : 15$ which indicates a pronounced modulation.

Lattice parameters, modulation wave vector and reflection conditions are consistent with the orthorhombic superspace group $P2_1mn(00\sigma)0s0$, No. 31.1.9.7 (Stokes et al., 2011; van Smaalen et al., 2013) (see supplementary material for details).

4.2.2 Structure solution and refinement

The structure was solved in (3+1)-dimensional superspace by applying charge flipping algorithm based on main and satellite reflections (Palatinus, 2013) using the program SUPERFLIP (Palatinus and Chapuis, 2007). The resulting higher-dimensional electron density map revealed the position of the tin (Sn1) atom along with initial values for its atomic modulation functions (AMFs). The asymmetric unit consists of a half tin atom which is centred on the mirror plane perpendicular \mathbf{b} . Structure refinement was done with software package JANA2006 (Petricek et al., 2014) (detailed information on the structure refinement strategy is given in the supplementary material). Positions of the oxygen and carbon atoms were determined along with initial values of their AMFs from difference Fourier maps. The oxygen atom (O1) and the carbon atom (C1) were found centred on the mirror plane perpendicular \mathbf{b} and the second carbon atom (C2) is in a general position. The asymmetric unit possesses half of a formula unit ($Z' = 0.5$). Up to four harmonic waves for displacive modulation for all atoms were introduced into the model. Refinement was found to diverge due to large correlations between parameters and anisotropic ADPs of light atoms were found to be non-positive definite. Analysis of the (3+1)-dimensional Fourier maps revealed that the amplitude of the AMFs (displacive) of the oxygen and carbon atoms required to describe the electron densities around them are significantly larger than that of the tin atom. Therefore in an alternate model, crenel (block-wave) functions (Petricek et al., 2016) were introduced for all atoms

by splitting the displacive AMFs along the internal dimension into eight parts with equal width $\Delta x_4 = 0.125$ (Fig. 4.3 and supplementary material). Hydrogen atoms were added to the carbon atoms by a riding model. Hydrogen atoms attached to the oxygen atoms were added on arbitrary positions and refined applying distance and angle restraints $d(\text{O-H}) = 0.82 \pm 0.01 \text{ \AA}$ and $\angle(\text{Sn-O-H}) = 106 \pm 1 \text{ deg}$, using the ADP constraints $U_{\text{iso}}(\text{H}) = 1.5U_{\text{eq}}(\text{O})$. In the final model all non-hydrogen atoms were described with anisotropic ADPs and the refinement converged without any non-positive definite ADPs at $R_F^{\text{obs}}(m = 0) = 0.0402$, $R_F^{\text{obs}}(m = \pm 1) = 0.0524$, $R_F^{\text{obs}}(m = \pm 2) = 0.0992$, $R_F^{\text{obs}}(m = \pm 3) = 0.1310$, $R_F^{\text{obs}}(m = -4) = 0.1638$. The description of the two models (crenel function and continuous harmonic wave) are equivalent in terms of the total number of parameters (=193).

To find out the origin along the internal dimension (initial phase of the modulation, t_0) and the corresponding symmetry of the corresponding three-dimensional eightfold superstructure, structure refinements were performed as function of t_0 ($t_0 = 0$ and $t = \frac{1}{16}$, space group orthorhombic $P2_1cn$ and for a general t_0 value, space group monoclinic **b**-unique Pc for the corresponding eightfold superstructure). Refinement showed that the model at $t_0 = 0$ fits best to the diffraction data (see Table A.1 in supplementary material). Hence, the $t_0 = \frac{1}{16}$ and monoclinic models were discarded from further analysis. The description of the commensurate model at $t_0 = 0$ and its corresponding superstructure are equivalent in terms of number of parameters (=193). Since the superspace group is non-centrosymmetric, inversion twin was tested. Refinement of the twin volumes resulted in a value of 0.5 within its standard uncertainty (absolute structure parameter (Flack, 1983) = 0.42 (12)) and hence was fixed to 0.5 (Table 4.1). Isotropic extinction parameter was introduced and refined with marginal improvement to the statistical parameters.

In the final (3+1)-dimensional superspace model the asymmetric unit consists of one half formula unit. Positions of the atoms Sn1, O1 and C1 which are on special positions (m^y, s): $x_1, -x_2, x_3, x_4 + \frac{1}{2}$ are split each into four positions and their AMFs are described by crenel functions along the internal dimension, x_4 of equal width $\Delta x_4 = 0.125$ (Sn1 into Sn1a, Sn1b, Sn1c, Sn1d; same holds for O1 and C1) (Fig. 4.3 and supplementary material). Position of the C2 atom which is a general position is split into eight and AMFs described by crenel functions of equal width $\Delta x_4 = 0.125$ (C2 to C2a, C2b, C2c, C2d, C3a, C3b, C3c and C3d) (see supplementary material for Fourier maps of all atoms).

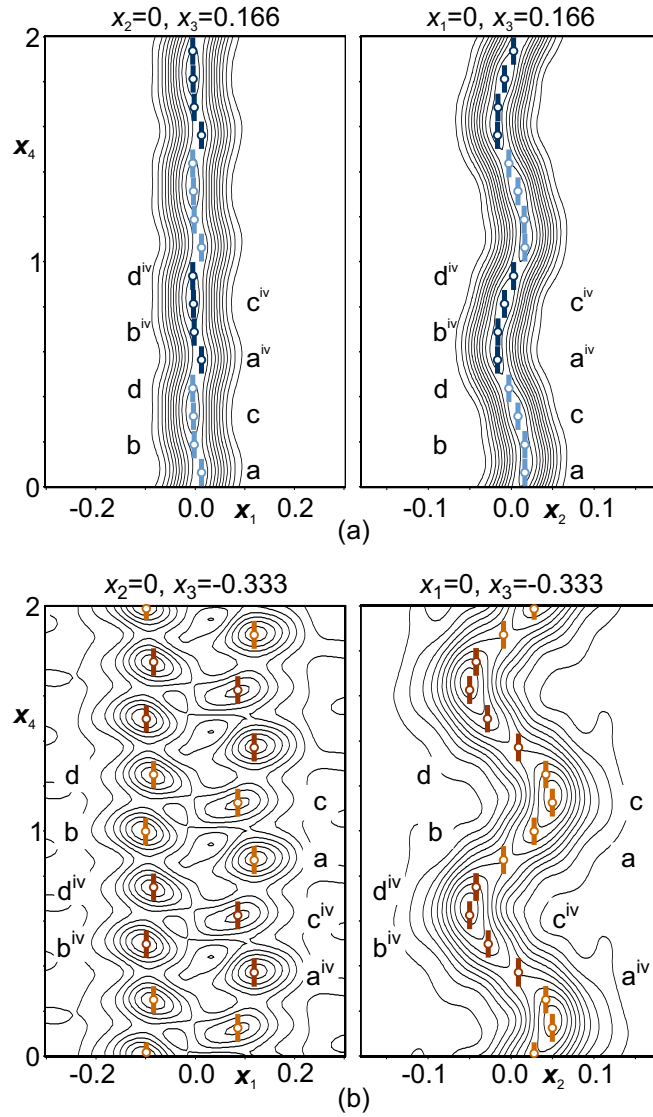


Figure 4.3: Fourier maps along x_4 for atoms (a) Sn1 (light blue) and Sn1^{iv} (dark blue), (b) O1 (orange) and O1^{iv} (dark brown). Symmetry code: (iv) $x_1, -x_2, x_3, x_4 + \frac{1}{2}$. Positions of the relevant t -values are shown by open circles. The step of the contour line is (a) $5 \text{ e}/\text{\AA}^3$, (b) $0.25 \text{ e}/\text{\AA}^3$. The width of the maps are 4 \AA . Fourier maps of all sections for all atoms can be found in supplementary material.

4.3 Results and discussion

The eightfold superstructure (space group $P2_1cn$) is derived from the (3+1)-dimensional superspace model by sampling the modulation wave at eight equidistant points ($t = 0, \frac{1}{8}, \frac{2}{8}, \frac{3}{8}, \frac{4}{8}, \frac{5}{8}, \frac{6}{8}$ and $\frac{7}{8}$, since the origin is chosen to be $t_0 = 0$). The glide plane (m^y, s) relates the t -sections 0 with $\frac{4}{8}$, $\frac{1}{8}$ with $\frac{5}{8}$, $\frac{2}{8}$ with $\frac{6}{8}$ and $\frac{3}{8}$ with $\frac{7}{8}$. In the eightfold superstructure four formula units $(CH_3)_3SnOH$ are in the asymmetric unit. The chain is completed by four more molecules generated by the c -glide plane perpendicular to the \mathbf{b} -axis in a chain along \mathbf{c} -axis. The second chain in the unit cell follows from the 2_1 and n operations (Fig. 4.4).

4.3.1 Symmetry relation to the low temperature structure

Following our model, the crystal symmetry of the compound is orthorhombic in both phases above and below $T_c = 176$ K (present structure and our earlier work (Dey et al., 2016b)) in contrast to the published structures with monoclinic symmetry (Anderson et al., 2011). Space group symmetries of the present eightfold superstructure ($P2_1cn$) above T_c and the twofold superstructure below T_c ($P2_12_12_1$) do not have group-subgroup relations. The two phases can be understood as two ground states of a hypothetical phase with centrosymmetric space group symmetry $Pm\bar{c}n$. The same argument holds also for the symmetry of the models within higher dimensional superspace approach as commensurately modulated structures. Superspace group symmetry $P2_1mn(00\sigma)0s0$ (present structure) and $P2_12_12(00\sigma)00s$ (Dey et al., 2016b) are subgroups of the centrosymmetric superspace group $Pm\bar{m}n(00\sigma)0s0$ No. 59.1.9.2 (Stokes et al., 2011; van Smaalen et al., 2013).

4.3.2 Conformation of the strands

The Sn atoms are shifted out of the planes defined by the three carbon atoms (C1, C2 and C3) by 0.006 to 0.018 Å towards the nearest oxygen atom depending on the shorter Sn–O bond ($d_{Sn-O} = 2.18 - 2.24$ Å). Sn–C distances are unequal ($d_{Sn-C} = 2.06 - 2.14$ Å) while angles $\angle(C-Sn-C)$ are 117.4 to 123.4 deg and $\angle(C-Sn-O)$ are 86.5 to 93 deg thus rendering individual C_3SnO groups distorted trigonal pyramidal configuration (interatomic distance and angles tabulated in supplementary material). The angles $\angle(O-Sn-O)$ are 175.5 to 178.3 deg which are almost linear and

$\angle(\text{Sn-O-Sn})$ are 139.2 to 143.1 deg are in good agreement with related structures (Clark et al., 1964; Schlemper and Britton, 1966; Domingos and Sheldrick, 1974; Sheldrick and Taylor, 1977; Glidewell and Liles, 1978; Deacon et al., 1993). The arrangement of Sn and O oxygen atoms thus generate zigzag along the **c**-axis (Fig. 4.4) in contrast to the proposed 8_3 helical arrangement in the published model (Anderson et al., 2011). Also the symmetry element *c*-glide which relates the formula units within the chain contradicts helical symmetry. However, the zigzag arrangement is not flat in comparison to the structural model in the low temperature phase (Dey et al., 2016b). Distortions of the torsion angles between adjacent oxygen atoms in the chain are 4.20 – 32.89 deg from an ideal 180 deg (Fig. 4.4).

The present structural model is ordered. However, diffuse scattering is observed in the present data as well as at $T = 100$ K (Dey et al., 2016b). This scattering is concentrated in planes perpendicular to the **c**-axis due to orthorhombic symmetry which is also the direction of the zigzag chains. The origin of the diffuse scattering can be due to lack of complete order between chains. This can be understood by different chains shifted along the **c**-axis with respect to each other which describes one-dimensional disorder (Welberry, 2004; Willis, 2006). In support of our argument, in the published $2\mathbf{a} \times 2\mathbf{b} \times 8\mathbf{c}$ supercell (Anderson et al., 2011) the authors considered weak superlattice reflections along \mathbf{a}^* and \mathbf{b}^* (which we found to be diffuse scattering) and found four independent chains to be shifted with respect to each other along **c**-axis. The zigzag arrangement of the chain is not aligned along any of the planes (**b**, **c**) and (**a**, **c**). This arbitrary orientation of the zigzag can also result in the origin of diffuse scattering.

4.3.3 Intra-strand and inter-strand interactions

In the low temperature phase, the shortest distance between hydrogen atoms is $d_{\text{CH}\cdots\text{HC}} = 2.53$ Å for methyl groups of adjacent molecules, and $d_{\text{OH}\cdots\text{HC}} = 2.63$ Å between neighboring hydroxy groups and methyl groups of a single chain (Dey et al., 2016b). In the 220 K model, the chains are compressed (**c** is shorter by 0.01 Å as compared to the low temperature phase) with angle $\angle(\text{Sn-O-Sn})$ as large as 143.1 deg. As result of the larger bending of the Sn-O-Sn bridges, shortest distances are $d_{\text{CH}\cdots\text{HC}} = 2.19$ Å and $d_{\text{OH}\cdots\text{HC}} = 2.26$ Å (Fig. 4.5 and Table 4.2). They indicate steric hindrance within the chains (twice van der Waals radii for hydrogen atom is 2.2~2.4 Å (Rowland and Taylor, 1996)). In order to avoid short H \cdots H contacts the

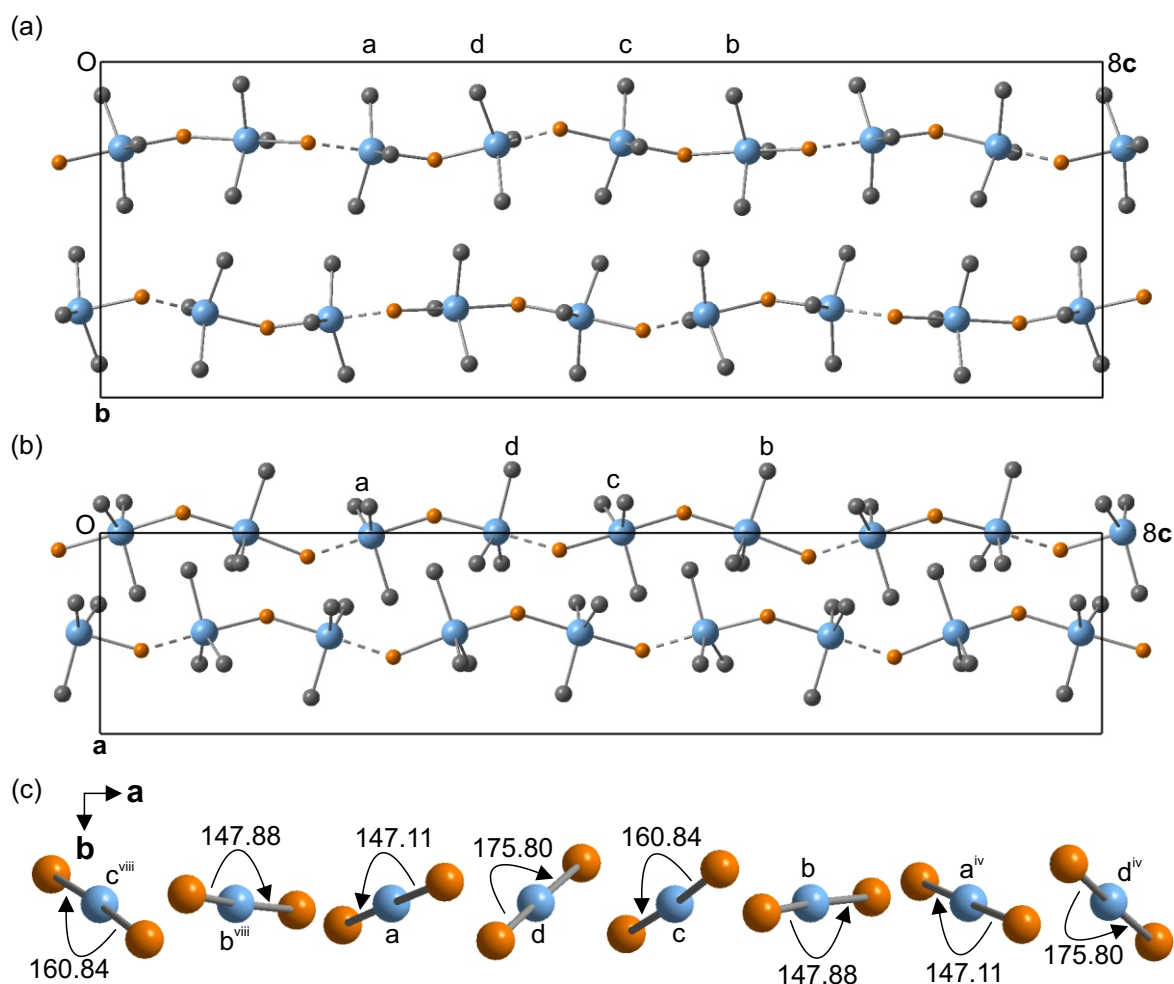


Figure 4.4: Unit cell of the eight-fold superstructure viewed along (a) $-\mathbf{a}$ and (b) \mathbf{b} . The short Sn–O bonds ($d(\text{Sn}-\text{O}) = 2.18$ and 2.19 \AA) are drawn by solid lines and the long Sn–O bonds ($d(\text{Sn}-\text{O}) = 2.23$ and 2.24 \AA) by dashed lines. (c) Eight O–Sn–O groups viewed along \mathbf{c} -axis showing the torsion angles between adjacent oxygen atoms. $\mathbf{a}, \mathbf{b}, \mathbf{c}$ and \mathbf{d} are the independent positions. H-atoms are not shown. Symmetry code: (iv) $x, -y, z + \frac{1}{2}$; (viii) $x, -y, z - \frac{1}{2}$. The molecular graphics has been prepared with DIAMOND (Brandenburg and Putz, 2014). (Superstructure with thermal ellipsoids and hydrogen atoms is given in supplementary material).

Table 4.2: Distances between hydrogen atoms of the hydroxy groups and methyl groups and between methyl groups of two adjacent $(\text{CH}_3)_3\text{Sn}$ groups within a chain close to and shorter than 2.4 Å (a t -plot for the distances is given in supplementary material).

Reference	Atom groups	Distance (Å)
O1a–H1o1a	O1a–H1o1a⋯H3c1a–C1a	2.42
(Fig. 4.5(a))	O1a–H1o1a⋯H3c2b ^{viii} –C2b ^{viii}	2.42
O1b–H1o1b	O1b–H1o1b⋯H2c2c–C2c	2.26
(Fig. 4.5(b))		
O1c–H1o1c	O1c–H1o1c⋯H2c3c–C3c	2.39
(Fig. 4.5(c))	C2c–H3c2c⋯H2c1d–C1d	2.19
O1d–H1o1d	O1d–H1o1d⋯H3c1d–C1d	2.30
(Fig. 4.5(d))		
<i>Symmetry code</i> : $(viii) x, -y, z - \frac{1}{2}$		

hydroxy groups must displace away from $(\text{CH}_3)_3\text{Sn}$ groups. This displacement is not possible as each oxygen atom is bonded to two tin atoms and can only twist and turn which explains the distortion of the zigzag from ideal 180 deg.

In the present structure, distortions of the “so called” planar zigzag chains have major consequences on the inter-strand C–H⋯O interaction scheme. These inter-strand distances $d_{\text{H}\cdots\text{O}}$ are in between 3.13 and 3.94 Å and the inter-strand angles $\angle(\text{C–H}\cdots\text{O})$ are in between 87.42 and 128.45 deg (Table 4.3). Since these interactions are on the longer side of reported C–H⋯O bonds a cut-off for the angles is hard to set (Steiner and Desiraju, 1998; Desiraju and Steiner, 2001). As weak hydrogen bonds are electrostatic in nature (Dannenberg et al., 1999; Desiraju and Steiner, 2001) C–H⋯O angles close to 90 deg and smaller can be discarded. This leaves six out of the eight C–H⋯O contacts which fulfill the condition of a C–H⋯O bond (Table 4.3). In order to achieve complete formation of the C–H⋯O bonds the chains must come closer to each other but that is prevented by short C3–H⋯H–C3 and C3–H⋯H–C2 contacts between different chains shorter than 2.4 Å (Table 4.4 and Fig. 4.6).

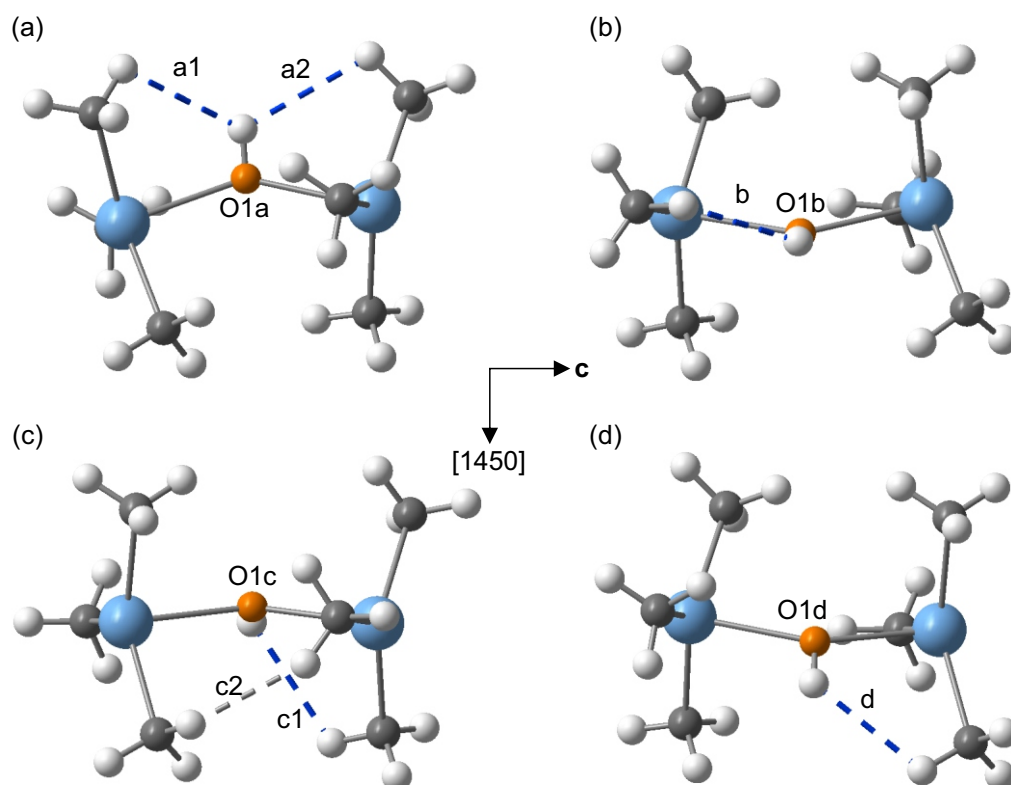


Figure 4.5: Interaction of the hydroxy groups (a) O1a–H1o1a, (b) O1b–H1o1b, (c) O1c–H1o1c and (d) O1d–H1o1d with the methyl groups. O–H...H–C (dashed blue) and C–H...H–C (dashed grey) equal to and shorter than 2.4 Å are shown. Viewing direction along $[-110]$. $a1 = \text{H1o1a} - \text{H3c2b}^{viii}$, $a2 = \text{H1o1a} - \text{H3c1a}$; $b = \text{H1o1b} - \text{H2c2c}$; $c1 = \text{H1o1c} - \text{H2c3c}$, $c2 = \text{H3c2c} - \text{H2c1d}$; $d = \text{H1o1d} - \text{H3c1d}$. The molecular graphics has been prepared with DIAMOND (Brandenburg and Putz, 2014).

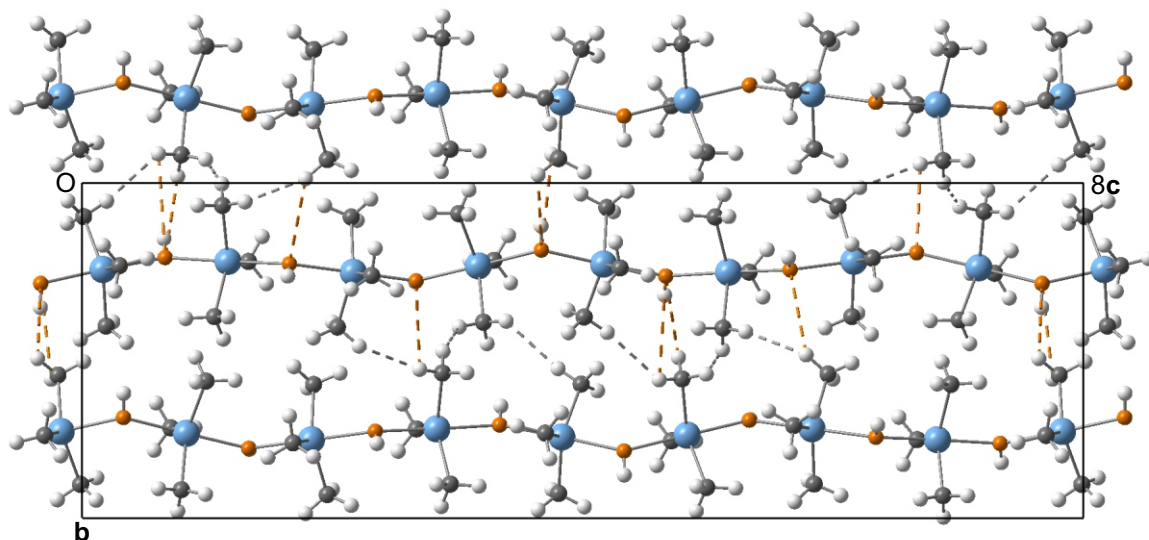


Figure 4.6: Supercell packing showing the inter-strand C–H \cdots O bonds (dashed orange) and short H \cdots H contacts (dashed grey) between the chains. Viewing direction along $-a$. The molecular graphics has been prepared with DIAMOND (Brandenburg and Putz, 2014).

Table 4.3: Distances (\AA) and angles (deg) in the inter-strand C–H \cdots O bonds (a t -plot for the distances is given in supplementary material).

C–H \cdots O	C–H	H \cdots O	C–O	$\angle(\text{C–H}\cdots\text{O})$
C3a–H1c3a \cdots O1a ^{vii}	0.96	3.94	4.0171	87.42
C3a–H3c3a \cdots O1a ^{vii}	0.96	3.35	4.0171	128.45
C3b–H2c3b \cdots O1d ⁱⁱ	0.96	3.15	3.6212	111.91
C3b–H3c3b \cdots O1d ⁱⁱ	0.96	3.46	3.6212	91.81
C3c–H1c3c \cdots O1c ^{vi}	0.96	3.28	3.5344	97.34
C3c–H3c3c \cdots O1c ^{vi}	0.96	3.29	3.5348	96.90
C3d–H1c3d \cdots O1b ⁱⁱ	0.96	3.55	3.8112	98.69
C3d–H3c3d \cdots O1b ⁱⁱ	0.96	3.59	3.8112	95.83

Symmetry code : (ii) $x + \frac{1}{2}, -y + \frac{1}{2}, -z + \frac{1}{2}$; (vi) $x - \frac{1}{2}, -y - \frac{1}{2}, -z + \frac{1}{2}$; (vii) $x - \frac{1}{2}, y + \frac{1}{2}, -z$

Table 4.4: Inter-strand distances (\AA) between hydrogen atoms of methyl groups shorter than 2.4 \AA (a t -plot for the distances is given in supplementary material).

Atom groups	Distance
C3a–H3c3a \cdots H2c3b v –C3b v	2.34
C3b–H3c3b \cdots H2c3d v –C3d v	2.36
C3d–H3c3d \cdots H2c2c ii –C2c ii	2.37

Symmetry code : (ii) $x + \frac{1}{2}, -y + \frac{1}{2}, -z + \frac{1}{2}$; (v) $x - \frac{1}{2}, -y + \frac{1}{2}, -z + \frac{1}{2}$

4.4 Conclusion

The eightfold superstructure of trimethyltin hydroxide has been successfully described as commensurately modulated structure within the (3+1)-dimensional superspace approach. Description of the atomic domains using a basic cell ($Z' = 0.5$) and modulation functions defined by crenel functions enabled a stable refinement of the crystal structure and a complete structural model is established with physically meaningful anisotropic ADPs of all the atoms and chemically meaningful hydroxy groups. The corresponding eightfold superstructure has four independent formula units ($Z' = 4$).

The $(\text{CH}_3)_3\text{Sn}$ groups are bridged by Sn–O bonds and exhibit distortion of the zigzag planes defined by the oxygen atoms of adjacent formula units as compared to the low temperature phase (Dey et al., 2016b) deviating from ideal 180 deg by 4.2 to 32.89 deg. This distortion within the chains is caused by steric interactions between the hydroxy groups and the methyl groups ($d_{\text{O-H}\cdots\text{C-H}} < 2.4 \text{\AA}$). The oxygen atoms are, on the other hand, bonded to two tin atoms which allows only twist and turn of the hydroxy groups. Hence, the present superstructure is as a result of competition between the dense packing of the formula units within the chain and optimal conformation of the hydroxy groups.

Large variations in the distortion of the zigzag planes within the chain have severe effects on the inter-strand C–H \cdots O hydrogen bonds which are either not completely formed or not formed at all. For complete formation of the C–H \cdots O bonds the chains should pack denser which is prevented by short C–H \cdots H–C distances, shorter than 2.4 \AA .

Chapter 5

The $Z' = 12$ superstructure of Λ -cobalt(III) sepulchrates trinitrate governed by C–H...O hydrogen bonds ¹

Λ -Cobalt(III) sepulchrates trinitrate crystallizes in $P6_322$ with $Z = 2$ ($Z' = 1/6$) at room temperature. Slabs perpendicular to the hexagonal axis comprise molecules Co(sepulchrates) alternating with nitrate groups A and B. Coordinated by six sepulchrates molecules, highly disordered nitrate groups C are accommodated between the slabs. Here we report the fully ordered, low-temperature crystal structure of Co(sep)(NO₃)₃. It is found to be a high- Z' structure with $Z' = 12$ of the 12-fold $6a_h \times \sqrt{3}b_h \times c_h$ superstructure with monoclinic symmetry $P2_1$ (c unique). Correlations between structural parameters are effectively removed by refinements within the superspace approach. Superstructure formation is governed by a densification of the packing in conjunction with ordering of nitrate group C, the latter assuming different orientations for each of the $Z' = 12$ independent copies in the superstructure. The Co(sep) moiety exhibits small structural variations over its 12 independent copies, while orientations of nitrate groups A and B vary less than the orientations of nitrate group C do. Molecular packing in the superstructure is found to be de-

¹This chapter has been published as: Dey, S., Schönleber, A., Mondal, S., Prathapa, S. J., van Smaalen, S. and Larsen, F. K. (2016). The $Z' = 12$ superstructure of Λ -cobalt(III) sepulchrates trinitrate governed by C–H...O hydrogen bonds, *Acta Crystallogr.* **B72**: 372–380.

temined by short C–H···H–C contacts, with H···H distances of 2.2–2.3 Å, and by short C–H···O contacts, with H···O distances down to 2.2 Å. These contacts presumably represent weak C–H···O hydrogen bonds, but in any case they prevent further densification of the structure and strenghtening of weak N–H···O hydrogen bonds with observed H···O distances of 2.4–2.6 Å.

5.1 Introduction

Macrobicyclic metal cage complexes are templating agents for the synthesis of silicates (Hondow et al., 2012) and zeolites (Garcia et al., 2001). These compounds also serve as catalysts enhancing electrochemical processes (Ritzert et al., 2013), as photosensitiser for the production of hydrogen from water (Pina et al., 1985) and as reducing agents in the field of bioelectrochemistry (Bernhardt et al., 2006). Crystal structures of these compounds are useful information, because applications of these compounds are correlated to their thermodynamic stability, stereochemistry, size and the nature of coordination inside the cages and the strong and weak interaction of the cages with the functional groups (Gahan and Harrowfield, 2015).

Λ -Cobalt(III) sepulchrates trinitrate, Co(sep)(NO₃)₃, (IUPAC name Λ -(1, 3, 6, 8, 10, 13, 16, 19-octaazabi-cyclo[6,6,6]eicosane)cobalt(III) trinitrate) is a sepulchrates cage complex. The sepulchrates moiety consists of a Co³⁺ cation sixfold coordinated by nitrogen atoms of the six amine groups ($N_{lig} = N21, N22, N23, N24, N25, N26$ in Fig. 5.1) of the sepulchrates molecule. The amine groups act as donors of lone pairs of electrons to the d^2sp^3 hybridized Co³⁺ cation conforming a distorted octahedron. The macrobicyclic cage is completed by three ethylene groups ($C_{en} = C31, C36; C33, C34; C32, C35$), six apical carbon atoms ($C_{ap} = C41, C42, C43, C44, C45, C46$) and two apical nitrogen atoms ($N_{ap} = N51, N52$ in Fig. 5.1).

The compound crystallizes in hexagonal symmetry with space group $P6_322$ at room temperature (phase I) (Dubicki et al., 1980; Schönleber et al., 2010). The Co(sep) cage and two symmetry related nitrate groups (nitrate groups A and B) are centred on threefold rotation axes. They have been reported to be connected *via* N–H···O hydrogen bonds (Dubicki et al., 1984). The third nitrate group (nitrate group C) is slightly displaced from the origin, exhibiting a six-fold orientational disorder (Schönleber et al., 2010).

A phase transition of Co(sep)(NO₃)₃ has been found to occur at $T_1 = 133$ K;

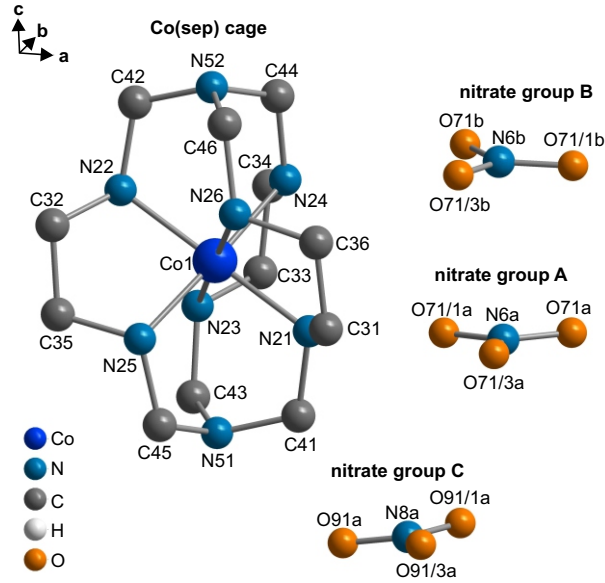


Figure 5.1: Molecular structure of Λ -cobalt(III) sepulchrate trinitrate along with the atomic numbering scheme. Hydrogen atoms have been omitted for clarity.

spectroscopic methods have indicated that below T_1 the crystals develop a domain structure, as it may appear due to a lowering of its symmetry (Dubicki et al., 1984). Single-crystal neutron diffraction experiments have revealed satellite reflections below T_1 . Their temperature dependence has indicated two further phase transitions, at $T_2 = 107$ K and $T_3 = 98$ K, respectively (Larsen et al., 1988). We have performed temperature-dependent single-crystal X-ray diffraction studies on $\text{Co}(\text{sep})(\text{NO}_3)_3$, which confirmed the existence of different phases at $T = 115$ K (phase II), 100 K (phase III) (chapter 6) and 95 K (phase IV). The two intermediate phases II and III possess incommensurately modulated crystal structures (Larsen et al., 1988).

The present X-ray diffraction experiments reveal the low-temperature phase (phase IV) to be a lock-in phase with a twelve-fold $6a_h \times \sqrt{3}b_h \times c_h$ superstructure of the room-temperature hexagonal structure. The phase transition from phase III to phase IV is identified as an incommensurate-to-commensurate transition accompanied by major changes of the modulation wave. Specifically, the disordered nitrate group C becomes fully ordered in phase IV, assuming different orientations at different sites within the 12-fold supercell. The order as well as the accompanying atomic displacements and molecular distortions are described by modulation

functions within the superspace approach (van Smaalen, 2012; Schönleber, 2011; Janssen et al., 2007). The origin of the modulation is discussed in terms of molecular conformations and intermolecular interactions, including the role of hydrogen bonding.

5.2 Experimental

5.2.1 Diffraction experiment and data integration

Single crystals of Co(sep)(NO₃)₃ were synthesized by the research team of Alan M. Sargeson (Creaser et al., 1982). The crystals are stable in air at ambient conditions. Single-crystal X-ray diffraction experiments were performed at beamline D3, HASYLAB DESY, Hamburg, employing radiation of a wavelength of $\lambda = 0.50917 \text{ \AA}$. The sample was mounted on a four-circle diffractometer in Euler geometry, and diffraction intensities were measured by a MAR-CCD area detector. A data set complete up to a resolution of $[\sin(\theta)/\lambda]_{\max} = 0.838 \text{ \AA}^{-1}$ was measured by ϕ and ω scans with several exposure times and different offsets of the detector, always maintaining a crystal-to-detector distance of 220 mm and using scans of 1 degree per image (Table 5.1).

Data processing has been performed with the software EVAL15 (Schreurs et al., 2010). Inspection of the frames revealed that main reflections are surrounded by satellite reflections of first order. Bragg reflections have been indexed using five integers $(h k l m_1 m_2)$ on a primitive hexagonal lattice and with modulation wave vectors

$$\begin{aligned} \mathbf{q}^1 &= (\sigma_h, \sigma_h, 0) \\ \mathbf{q}^2 &= (-2\sigma_h, \sigma_h, 0). \end{aligned} \quad (5.1)$$

Refinement of the hexagonal orientation matrix and the component of the modulation wave vector resulted in $2\sigma_h = 0.16726(10) = \frac{1}{6} + 0.00059(10)$, suggesting an incommensurate modulation. However, diffraction images exhibit diffraction maxima that appear as overlapping Bragg reflections from different domains rather than single peaks. Therefore, we have used an alternative indexing of the diffraction pattern on the C -centered $a_h \times \sqrt{3}b_h \times c_h$ orthohexagonal unit cell. In case of orthorhombic symmetry, each main reflection is composed of three different,

Table 5.1: Experimental and crystallographic data.

Crystal data	
Chemical formula	Co(C ₁₂ H ₃₀ N ₈)(NO ₃) ₃
M_r	531.4
Crystal dimensions (mm ³)	0.254 x 0.133 x 0.103
Crystal system	Monoclinic <i>c</i> -unique
Superspace group	$C2_1(\sigma_1\sigma_2)0$
T (K)	95.0 (3)
a (Å)	8.42830 (10)
b (Å)	14.59840 (10)
c (Å)	15.70570 (10)
γ (deg)	89.9943 (3)
V (Å ³)	1932.42 (3)
Z	4
Wavevector \mathbf{q}	($\frac{1}{6}$, 0, 0)
Commensurate section	$t_0 = 0$
Supercell	$6a \times b \times c$
Supercell space group	$P2_1$
Radiation type	Synchrotron
Wavelength (Å)	0.50917
μ (mm ⁻¹)	0.39
Diffraction data	
$[\sin(\theta)/\lambda]_{\max}$ (Å ⁻¹)	0.83777
$\Delta\varphi, \Delta\omega$ (deg)	1
Exposure time (s)	4, 10, 80
Absorption correction	empirical, multiscan
Criterion of observability	$I > 3\sigma(I)$
Unique reflections	
All (obs/all)	19292/59443
Main (obs/all)	7916/8468
Satellites (obs/all)	11376/50975
R_{int} (obs/all)	0.0183/0.0225
Refinement	
GoF (obs/all)	2.11/1.32
$R_{\text{obs}}/wR_{\text{all}}$	0.0493/0.0662
No. of parameters	865
H-atom treatment	mixed
Twin volumes (1, 2)	
(3, 4)	0.163 (2), 0.1480 (11)
(5, 6)	0.1845 (11), 0.1384 (11)
(5, 6)	0.1731 (11), 0.1932 (11)
Twin matrices (2)	
(3)	$-\frac{1}{2} \ -\frac{3}{2} \ 0 \ \frac{1}{2} \ -\frac{1}{2} \ 0 \ 0 \ 0 \ 1$
(4)	$-\frac{1}{2} \ \frac{3}{2} \ 0 \ -\frac{1}{2} \ -\frac{1}{2} \ 0 \ 0 \ 0 \ 1$
(5)	$1 \ 0 \ 0 \ 0 \ -1 \ 0 \ 0 \ 0 \ -1$
(6)	$-\frac{1}{2} \ \frac{3}{2} \ 0 \ \frac{1}{2} \ \frac{1}{2} \ 0 \ 0 \ 0 \ -1$
(6)	$-\frac{1}{2} \ -\frac{3}{2} \ 0 \ -\frac{1}{2} \ \frac{1}{2} \ 0 \ 0 \ 0 \ -1$
$\Delta\rho_{\text{min}}/\Delta\rho_{\text{max}}$ (e/Å ³)	-0.60/0.58

nearly coincident Bragg reflections from the three domains, while satellite reflections have contributions from a single domain only [Fig. 5.2(a)]. With respect to the orthohexagonal unit cell the satellite reflections are indexed by $\mathbf{q}^o = (\sigma_o, 0, 0)$ with $\sigma_o \approx 2\sigma_h$. In case of monoclinic symmetry, each main reflection is composed of six different, nearly coincident Bragg reflections from the six domains; satellite reflections now have contributions from two domains (Fig. 5.2). Each domain of monoclinic symmetry is modulated by a single modulation wave vector

$$\mathbf{q} = (\sigma_m, \sigma_2, 0) \quad (5.2)$$

with $\sigma_m \approx 2\sigma_h$ and $\sigma_2 \approx 0$.

Refinement with EVAL15 of the orthorhombic lattice parameters and the orientations of the six lattices resulted in a very small orthorhombic lattice distortion together with $\sigma_o = \frac{1}{6} - 0.000071$ (26). Further lowering of the symmetry to monoclinic resulted in a lattice distortion given by the angle $\gamma = 89.9943$ (3) deg and $\sigma_m = \frac{1}{6} - 0.000026$ (9). This value is much closer to the commensurate value $1/6$ than the value obtained with the hexagonal lattice and it differs from $1/6$ by less than three standard uncertainties. The discrepancies can be explained by the fact that the twinned refinement determines the position of the modulation wave vector with respect to the reciprocal lattice in its own domain, whereas the 2D modulation on the hexagonal lattice determines the average satellite position with respect to the average lattice of all domains. A non-zero value for σ_2 leads to instable refinements and a non-significant value for this parameter. Together, we take these refinements as experimental evidence for the commensurability of the modulation in phase IV.

The severe overlap of Bragg reflections from different domains prevents the determination of integrated intensities of individual reflections. Instead, accurate intensities can be obtained for each group of overlapping reflections. Furthermore, available software for absorption correction cannot simultaneously handle twinned and incommensurate data. Therefore, integrated intensities have been determined within the hexagonal setting, employing the two modulation wave vectors from Eq. 5.1. Integrated intensities have been obtained for main reflections, $(hkl00)$ and satellite reflections of first order, $(hkl\pm 10)$, $(hkl0\pm 1)$ and $(hkl\pm 1\mp 1)$, employing EVAL15. Absorption correction was determined by SADABS (Bruker, 2008). Throughout these calculations, monoclinic point symmetry $2/m$ (c unique) has been used. This is the minimum symmetry of the diffraction pattern in case of twin domains of unequal volume fractions. Only for equal volume fractions of the domains

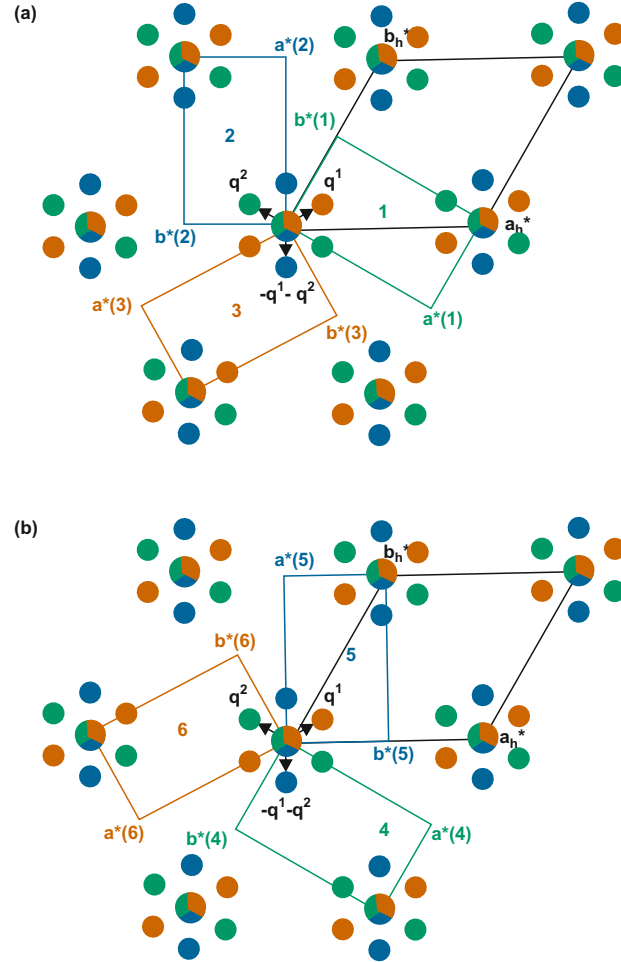


Figure 5.2: Schematic drawing of the diffraction pattern at $T = 95$ K exhibiting hexagonal to monoclinic six-fold twinning. (a) \mathbf{q}^2 , $\mathbf{q}^1 + \mathbf{q}^2$ and \mathbf{q}^1 belong to the green (1), blue (2) and red (3) orthorhombic or monoclinic domains, respectively. (b) Monoclinic twin domains 4 and 5 and 6 are generated by applying twofold rotation axes parallel \mathbf{a} to the twin domains 1, 2 and 3, respectively. The assignment of the \mathbf{q} -vectors to the twin domains has been chosen consistent with the *International Tables for Crystallography* Vols. A and C (Arnold, 2006; Janssen et al., 2006). The reconstructed reciprocal layer $hk\bar{2}$ is given as Fig. S1 in the Supplementary material.

the point symmetry can become higher, *e.g.* $6/mmm$ in case of all volume fractions being equal.

After data reduction, the dataset was split into one subset of main reflections (common to all twin domains) and three subsets of satellites reflections (for the three twin domains 1, 2 and 3; Fig. 5.2(a); twin matrices are given in Table 5.1). The indices were transformed from $(hklm_1m_2)$ to $(hklm)$ without changing h , k or l , and with $m = -m_2$ for twin domain 1, $m = m_1 + m_2$ for twin domain 2 and $m = -m_1$ for twin domain 3. The reflection indices were then transformed to the C centered orthohexagonal setting (Arnold, 2006), using the software JANA2006 (Petricek et al., 2014). The three additional monoclinic twin domains 4, 5 and 6 were described by applying a twofold rotation along \mathbf{a} to the domains 1, 2 and 3, respectively. In this way, satellite reflections of each of the three pairs of domains coincide with each other according to $(hklm)$ of domain 1 coincides with $(h-k-lm)$ of domain 4; main reflections of all six domains coincide. The ratio of the average intensities $\langle I \rangle$ between main and satellite reflections is approximately 60 : 1, while the average significance $\langle I/\sigma(I) \rangle$ has a ratio 4 : 1 between main and satellite reflections.

5.2.2 Structure solution and refinement

A model for the 12-fold superstructure of phase IV of Co(sep)(NO₃)₃ at $T = 95$ K has been developed within the superspace approach (van Smaalen, 2012). The basic structure is nearly identical to the crystal structure of phase I, but it has been described on the C -centered orthohexagonal unit cell (Table 5.1). Consideration of diffraction symmetry (Table 5.1) and reflection conditions has lead to space group $C2_1$ (\mathbf{c} -unique) for the basic structure, where the monoclinic unique axis is equal to the hexagonal axis of phase I. This space group is a non-standard setting of $P2_1$, No. 4 in the *International Tables for Crystallography, Vol. A*. The superspace group has been found as $C2_1(\sigma_1 \sigma_2 0)0$ with $\sigma_1 = \sigma_m = \frac{1}{6}$ and $\sigma_2 = 0$. This superspace group is a non-standard setting of $P2_1(\sigma_1 \sigma_2 0)0$, No. 4.1.2.1 in Stokes et al. (2011) and van Smaalen et al. (2013).

Formally, charge flipping does not apply to diffraction data from crystals twinned by (pseudo-)merohedry. Nevertheless, SUPERFLIP (Palatinus and Chapuis, 2007) applied to the present data allowed us to determine the positions of the cobalt atom along with initial values for its modulation parameters. Positions of the other non-hydrogen atoms were derived from the atomic positions of phase I (Schönleber et al.,

2010), employing JANA2006 for application of group–subgroup relations following the reduction of symmetry from $P6_322$ to $C222_1$ to $C2_1$. The low, monoclinic symmetry of the pseudo-hexagonal basic structure is responsible for large correlations between structural parameters. Therefore, restraints on interatomic distances and bond angles of the Co(sep) cage have been introduced in accordance with the crystal structure of phase I (Schönleber et al., 2010). The nitrate groups have been described as planar molecules with point symmetry 32, leaving the N–O distance as single refinable parameter. One nitrate molecule is placed in two independent positions corresponding to the nitrate groups A and B. A second nitrate molecule is used for nitrate group C. Each independent position is defined by three translational and three rotational parameters. The modulations of the nitrate groups were initially described by small values for the amplitudes of the first-order harmonic waves for modulation of translations and rotations. Displacement modulations of the other non-hydrogen atoms have been described by a single harmonic wave with initially small values for the parameters, except cobalt, for which the parameters obtained by SUPERFLIP have been used. Hydrogen atoms were added to all ligand and nitrogen atoms (N_{lig}), and all ethylene (C_{en}) and apical (C_{ap}) carbon atoms by a riding model, keeping tetrahedral geometries with distances $d(\text{N–H}) = 0.87 \text{ \AA}$ and $d(\text{C–H}) = 0.96 \text{ \AA}$. Atomic displacement parameters (ADPs) of hydrogen atoms follow from $U_{\text{iso}}(\text{H}) = 1.2 U_{\text{eq}}(\text{parent atom})$. Structure refinements of this (3+1)-dimensional superspace model have been performed with JANA2006. Employing isotropic ADPs and the incommensurate approximation, the refinement converged at $R_F^{\text{obs}}(\text{main}) = 0.1254$ and $R_F^{\text{obs}}(\text{sat}) = 0.1564$ for main and satellite reflections, respectively.

In the next step, anisotropic ADPs were introduced for the non-hydrogen atoms in the Co(sep) cage and TLS parameters (Schomaker and Trueblood, 1968) were applied to the nitrate groups. Refinement resulted in a much improved fit to the main reflections with $R_F^{\text{obs}}(\text{main}) = 0.0425$ and $R_F^{\text{obs}}(\text{sat}) = 0.1451$, and a large reduction of the features in the difference Fourier map, *viz* $\Delta\rho_{\text{min}}/\Delta\rho_{\text{max}}$ reduced from $-2.26/10.84$ to $-1.02/2.19 \text{ e/\AA}^3$. Subsequently, first-order harmonic waves have been introduced for modulation of ADPs of non-hydrogen atoms of the Co(sep) cage and for modulation of the TLS parameters of the nitrate groups. Refinement resulted in an improved fit to the satellite reflections with $R_F^{\text{obs}}(\text{main}) = 0.0389$ and $R_F^{\text{obs}}(\text{sat}) = 0.1052$.

The next step involved the introduction of first-order harmonic waves for the 3rd order Gram–Charlier parameters of the cobalt atom, while the basic 3rd order Gram–Charlier parameters were constrained to remain zero (Li et al., 2011). The fit to the diffraction data improved again at $R_F^{\text{obs}}(\text{main}) = 0.0376$ and $R_F^{\text{obs}}(\text{sat}) = 0.1002$. More importantly, ADPs of the ten atoms in the the Co(sep) cage, which were previously non-positive definite, become positive definite by this procedure.

In the final model constraints of the riding model on the fractional coordinates and modulation parameters of the hydrogen atoms attached to the six N_{lig} atoms were replaced by restraints on distances and angles. Restraint parameters are $d(\text{N–H}) = 0.87 \pm 0.02$ Å and $\angle(\text{H–N–Co}) = \angle(\text{H–N–C3}) = \angle(\text{H–N–C4}) = 109.47 \pm 1$ deg. Refinement resulted in an again improved fit, with $R_F^{\text{obs}}(\text{main}) = 0.0373$ and $R_F^{\text{obs}}(\text{sat}) = 0.0998$, and much reduced features in the difference Fourier map (Table 5.1). The plot of F_{obs} vs. F_{calc} shows an excellent match between these quantities (figure in the Supplementary material).

The commensurability of the modulation requires the selection of the correct value of the initial phase, t_0 , of the modulation wave (van Smaalen, 2012). For the 12-fold superstructure, the modulation wave is sampled at 12 equidistant points. Since only first-order satellite reflection have been observed (Fig. 5.3), this implies that different t_0 as well as the incommensurate model provide fits to the diffraction data of nearly equal quality. Table 5.2 gives partial R values for three different values of t_0 . We believe that the minor differences in R values are not sufficient to uniquely determine t_0 . Nevertheless $t_0 = \frac{1}{48}$ has slightly higher R values and represents a supercell structure with triclinic symmetry, while $t_0 = 0$ gives the lowest R values and corresponds to the highest supercell symmetry with space group $P2_1$ (a model with the same symmetry is obtained for $t_0 = \frac{1}{24}$). Evidence for lowering the symmetry to triclinic thus is lacking and we have chosen the monoclinic model with $t_0 = 0$ for further analysis.

The relatively high partial $R_F^{\text{obs}}(\text{sat})$ value for satellite reflections (Table 5.2) can be explained by rather weak reflections, as it is expressed by the magnitudes of partial R values for satellite reflections for the averaged standard uncertainty over intensity $R_\sigma(\text{sat}) = 0.1510$ and for averaging of equivalent reflections $R_{\text{int}}(\text{sat}) = 0.1420$. Further evidence for the final structure model has been obtained by establishing that the following variations of the model did not improve the fit to the diffraction data:

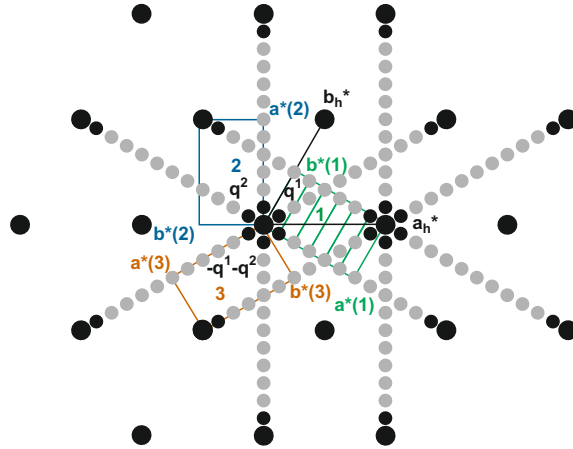


Figure 5.3: Schematic drawing of the diffraction pattern at $T = 95$ K. Positions are indicated of all possible commensurate satellite reflections. Black circles represent observed reflections while grey circles denote reflection positions unobserved in the present experiment. The sixfold supercell corresponding to the green domain in Fig. 5.2 is highlighted by thin lines.

- I. Treatment of nitrate group A and nitrate group B as different molecules lead to large correlations in the positions of their oxygen atoms without any significant changes in R -values.
- II. The Co(sep) cage was refined without distance and angle restraints and individual atoms were refined for the nitrate groups. This model results in improved statistical parameters of refinement ($R_F^{\text{obs}}(\text{main}) = 0.0335$ and $R_F^{\text{obs}}(\text{sat}) = 0.0975$), but the ADPs of four carbon atoms are non-positive definite and the geometries of the nitrate groups are outside the physically possible range.
- III. Since the symmetry is non-centrosymmetric, inversion twinning was introduced for all six twin domains. The refinement resulted in insignificant values of the inversion twin volumes.
- IV. Second-order harmonic waves were added for displacive modulation of the atoms but the resulting modulation functions showed ripples indicating fitting of the noise in the data.
- V. Isotropic secondary extinction correction resulted in a negative extinction parameter.

Table 5.2: Statistical parameters (R_F^{obs} and $wR_{F^2}^{\text{all}}$) of commensurate refinements of the final model with different values of the phase t_0 .

	$t_0 = 0$	$t_0 = \frac{1}{48}$	$t_0 = \frac{1}{24}$
Supercell	$P2_1$	$P1$	$P2_1$
space group			
R_F^{obs} (all)	0.0493	0.0496	0.0493
$wR_{F^2}^{\text{all}}$ (all)	0.0662	0.0665	0.0662
R_F^{obs} (main)	0.0374	0.0378	0.0374
$wR_{F^2}^{\text{all}}$ (main)	0.0490	0.0496	0.0490
R_F^{obs} (sat)	0.0998	0.1000	0.0998
$wR_{F^2}^{\text{all}}$ (sat)	0.1250	0.1252	0.1250
$\Delta\rho_{\text{min}}$ (e/Å ³)	-0.58	-0.61	-0.58
$\Delta\rho_{\text{max}}$ (e/Å ³)	0.60	0.59	0.60

5.3 Discussion

5.3.1 Variation of molecular conformations for $Z' = 12$

The crystal structure of the low-temperature phase (phase IV) of Co(sep)(NO₃)₃ is a high- Z' structure. Only a few crystal structures feature more independent molecules in the unit cell than the presently observed $Z' = 12$ (for example the amino acid *L*-tryptophan with $Z' = 16$ (Görbitz et al., 2012); see also the review article by Steed and Steed (2015) and references therein, as well as the HIGH Z' STRUCTURE DATA BASE by Steed (2016)). High- Z' structures usually suffer from severe correlations between parameters in structure refinements, and restrictions on the parameters beyond symmetry restrictions are necessary. An elegant way of imposing non-symmetry restrictions is the superspace approach (Schönleber, 2011; van Smaalen, 2012; Pinheiro and Abakumov, 2015). Parameters are separated into a relatively small subset of atomic coordinates describing the basic structure (one molecule Co(sep) and three nitrate ions) and parameters describing deviations from the basic structure. For Co(sep)(NO₃)₃ we have observed satellite reflections in the X-ray diffraction of first order only (Fig. 5.3), which implies that the superstructure

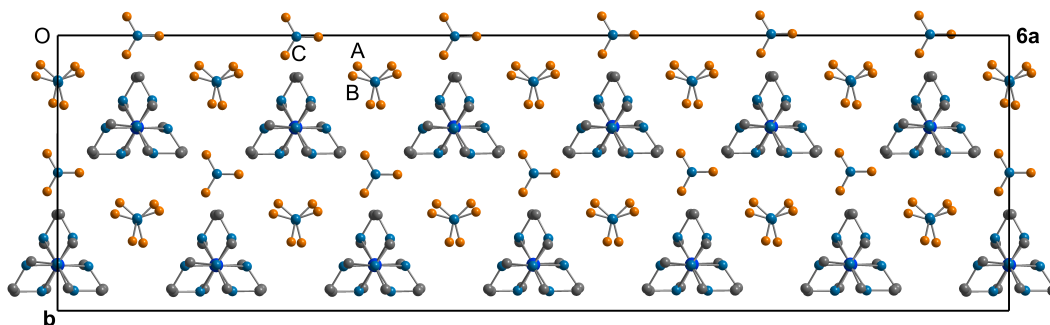


Figure 5.4: Unit cell of the superstructure projected onto (0 0 1). Atoms with $-0.05 < z < 0.45$ are shown (one layer; compare to Fig. 5.5). Hydrogen atoms are not shown.

is described by a single-harmonic modulation function for each independent parameter of the basic structure; higher harmonics cannot be determined (see the end of Section 5.2.2). Deviations from the basic structure are small indeed, as is easily seen by consideration of a plot of the superstructure, showing the 12 crystallographically independent, but nearly indistinguishable copies of the molecule (Figs. 5.4 and 5.5). The superspace approach reduces the number of independent parameters dramatically as compared to the 12-fold supercell. Nevertheless, the monoclinic superspace group of phase IV does not capture the pseudo-trigonal symmetry of the Co(sep) molecule, and further restrictions have turned out to be necessary. We have chosen to use rather narrow restraints on bond lengths and bond angles (Section 5.2.2). They are justified in hindsight by the good fit to the diffraction data of the thus refined structure model (Tables 5.1 and 5.2).

Unsurprisingly, the twelve crystallographically independent Co(sep) molecules in the 12-fold supercell feature similar values for each bond length and each bond angle. The variations are most favourably analysed by t -plots (van Smaalen, 2012), which provide the continuous dependence of each structural parameter on the phase t of the modulation wave. Values observed in the 12-fold superstructure with $t_0 = 0$ are the values $t = n/12$ for $n = 0, \dots, 11$. Figure 5.6 provides a t -plot of the distances between the Co atom and the 12 carbon atoms of the same molecule. It shows that these distances (not restrained in the refinement) have but minor variations between the twelve molecules. The (small) elongation of one Co–C bond is compensated by shortening of another Co–C bond, in complete agreement with the behavior of other modulated compounds. Presently, distances towards the three

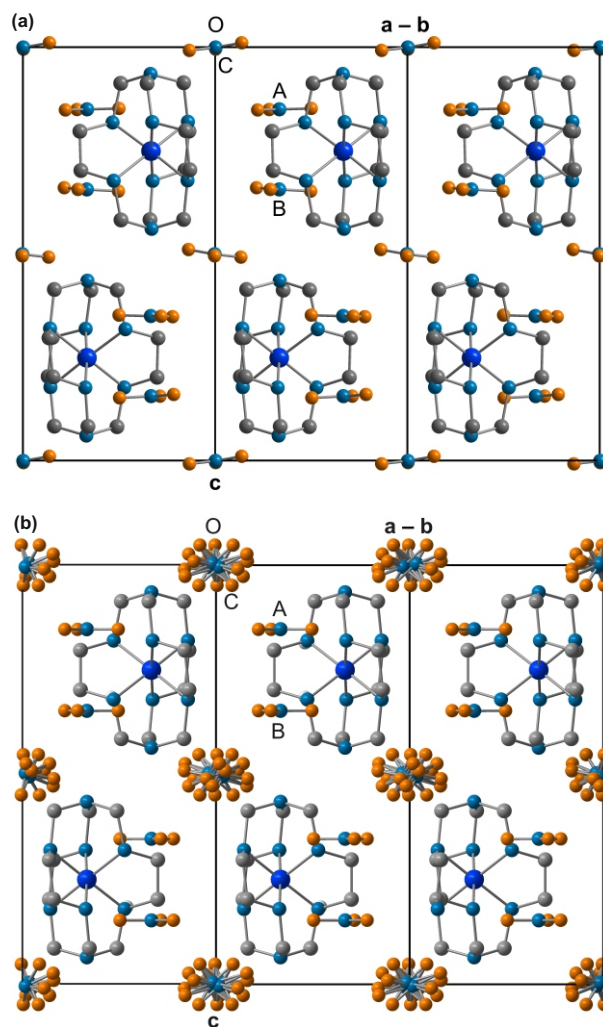


Figure 5.5: (a) The basic structure at $T = 95$ K (phase IV) projected onto (1 1 0) and (b) the disordered phase at room temperature (phase I; Schönleber et al. (2010)). Hydrogen atoms are not shown.

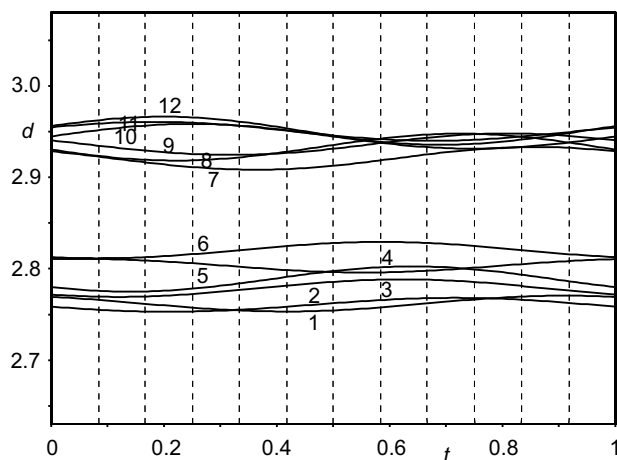


Figure 5.6: t -Plot of interatomic distances d (Å) between the Co atom and the C atoms of the same molecule. Vertical, dashed lines indicate t values corresponding to the distances in the 12-fold supercell. The twelve interatomic contacts are (compare Fig. 5.1): 1=Co1-C36, 2=Co1-C34, 3=Co1-C33, 4=Co1-C35, 5=Co1-C31, 6=Co1-C32, 7=Co1-C45, 8=Co1-C43, 9=Co1-C41, 10=Co1-C44, 11=Co1-C42, and 12=Co1-C46.

apical C atoms at the top of the molecule (Nrs. 10-12 in Fig. 5.6) are longer than average simultaneously with the distances towards the three apical C atoms at the bottom of the molecule being shorter than average (Nrs. 7-9). This reflects the largest modulation amplitude of Co being along c (Table S1 in the Supplementary material). Angles within the $\text{Co}(\text{N}_{lig})_6$ octahedron deviate more from their ideal values than in the structure of phase I (Schönleber et al., 2010), but their variation with t is again very small (see Supplementary material). Bond lengths and bond angles of all twelve independent $\text{Co}(\text{sep})$ molecules thus are similar to each other. The average molecule in phase IV has a slightly more distorted geometry than the structure of the molecule within the high-symmetry phase (Schönleber et al., 2010) as well as in other filled sepulchrate complexes (Bacchi et al., 1993; 1996; Gahan and Harrowfield, 2015).

Nitrate groups have been restricted to be flat with O–N–O angles of 120 deg and three equal N–O bond lengths (Fig. 5.1). Nitrate groups A and B have been described by a common molecule with a refined N–O bond length of 1.237 Å. The N–O bond in nitrate group C is shorter with $d(\text{N–O}) = 1.16$ Å. Major differences between the different copies of the nitrate groups A, B and C are the orientations

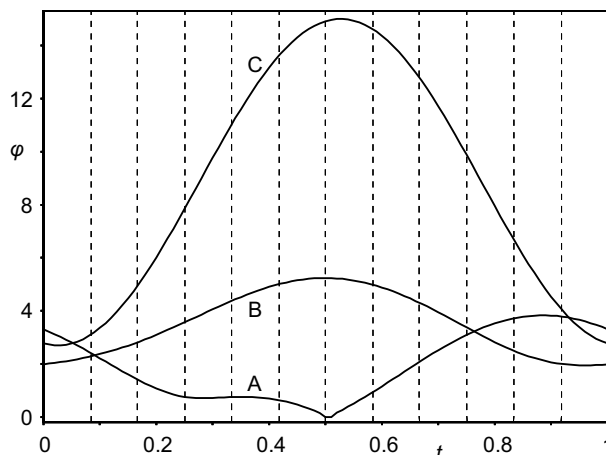


Figure 5.7: t -Plot of the angles φ (deg) between the \mathbf{a} , \mathbf{b} plane and the molecular planes of the nitrate groups A, B and C. Vertical, dashed lines indicate t values corresponding to the angles in the 12-fold supercell.

of these planar molecular anions (Fig. 5.7). We believe this part of the modulation to be at the origin of the complicated superstructure, as it is described in the next section.

5.3.2 Competing intermolecular interactions

In phase I, the nitrate groups A and B are parallel to the (\mathbf{a}, \mathbf{b}) -plane. In the present structure (phase IV), the planes of the 12 nitrate groups A and the 12 nitrate groups B make different angles with the (\mathbf{a}, \mathbf{b}) -plane, with values between 0 and 5 deg (Fig. 5.7). These small rotations are the result of optimizing the interactions between nitrate and sepulchrate moieties (see below). Nitrate group C is highly disordered in phase I (Fig. 5.5(b); Schönleber et al. (2010)). The increased packing density at lower temperatures forces each nitrate C into a single orientation. Orientations of the 12 crystallographically independent nitrate groups C exhibit a much larger variation than orientations of nitrate groups A and B (Fig. 5.7), again apparently the result of optimizing intermolecular interactions.

Nitrate groups A and B form N–H \cdots O hydrogen bonds with the sepulchrate cages (Fig. 5.8). Distances H \cdots O vary between ~ 2.4 and 2.6 Å for the six H \cdots O interactions about each nitrate group, but each contact exhibits but a small variation between the 12 independent nitrate groups A and B, as it is evidenced by the t -plot

of these distances (4–9 in Fig. 5.9). This implies that they are weak hydrogen bonds (Jeffrey, 1997), which are hardly affected by the modulation. One would expect the molecules to close in, in order to strengthen the N–H···O hydrogen bonds. However, this is prevented by the actually shortest interatomic distances between molecules.

Nitrate groups A and B are involved in C–H···O interactions, which are shorter than the N–H···O hydrogen bonds (Fig. 5.9). As short as 2.2 Å, these H···O distances are at the lower side of reported C–H···O hydrogen bonds (Desiraju, 1991; Desiraju et al., 1993; Steiner and Desiraju, 1998; Desiraju and Steiner, 2001; Munshi and Guru Row, 2005). It can thus be conjectured that even closer separations of these atoms would take them onto the repulsion part of the interaction curve, which would be energetically unfavourable. C–H···O interactions rather than N–H···O hydrogen bonds thus determine the packing in Co(sep)(NO₃)₃.

The shortest contacts between nitrate group C and the sepulchrate cage are between the oxygen atoms (atoms O9) and hydrogen atoms connected to the apical carbon atoms (atoms H2c41 through H2c46) (Fig. 5.10). The range of H···O distances of ~ 2.2–2.5 Å is similar to the distances of the C–H···O contacts of nitrate groups A and B (Fig. 5.11). Finally, short intermolecular interatomic distances are found between hydrogen atoms attached to apical carbon atoms on neighbouring sepulchrate molecules (Fig. 5.12). Again, these contacts prevent a denser packing of the molecules.

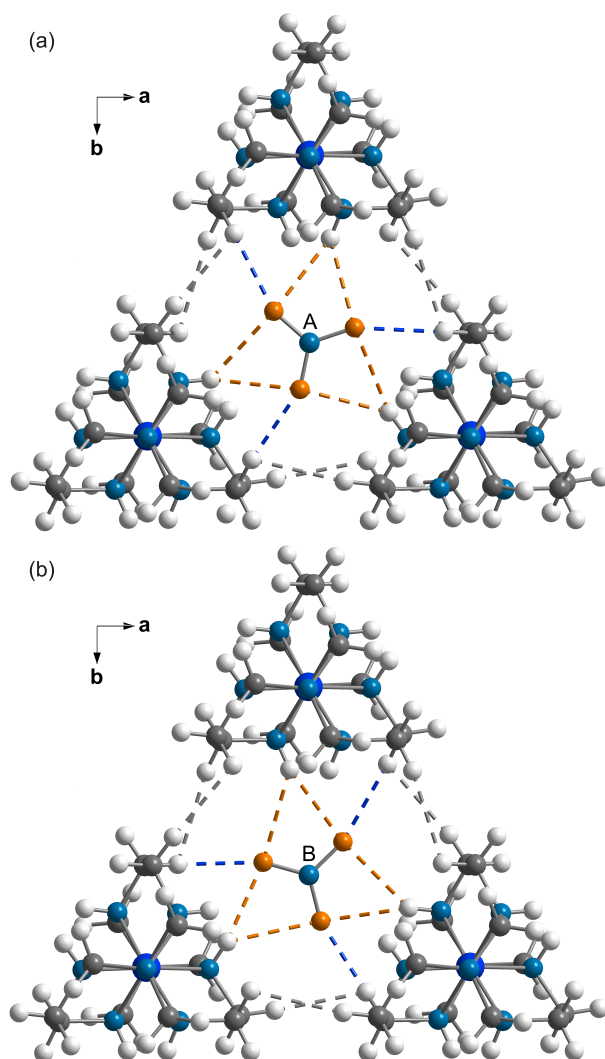


Figure 5.8: Environments of the nitrate groups A and B in a view along (0 0 1). Dashed lines indicate N-H \cdots O hydrogen bonds (orange), C-H \cdots O hydrogen bonds (blue) and short C-H \cdots H-C contacts between participating sepulchrate cages (grey). (a) Nitrate group A at $z = 0.15$; and (b) Nitrate group B at $z = 0.34$. Co(sep) cages are centered at $z = 1/4$ (Compare to Fig. 5.5).

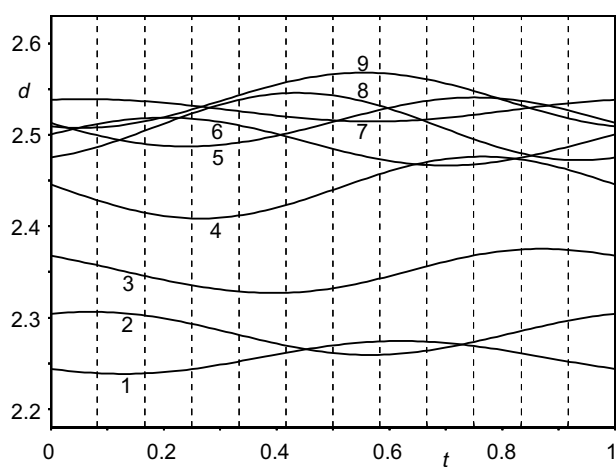


Figure 5.9: t -Plot of interatomic distances d (Å) between the O atom of nitrate A and hydrogen atoms of the sepulchate cage. Vertical, dashed lines indicate t values corresponding to the distances in the 12-fold supercell. Six N-H...O contacts (4–9) and three C-H...O contacts (1–3) are shown (compare Fig. 5.1): 1=O71/3a...H2c35, 2=O71a...H2c31, 3=O71/1a...H2c33, 4=O71/3a...H1n21, 5=O71/1a...H1n21, 6=O71a...H1n25, 7=O71/1a...H1n25, 8=O71/3a...H1n23, and 9=O71a...H1n23. A similar plot for nitrate group B is given as Fig. S9 in the Supplementary material.

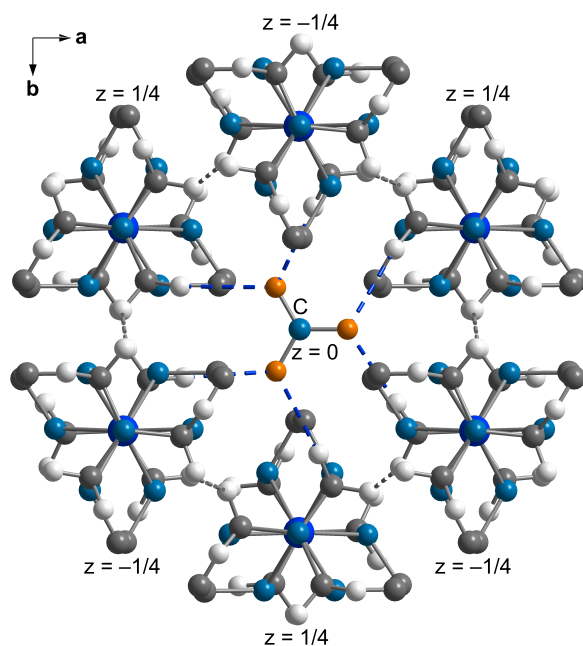


Figure 5.10: Projection onto (001) of nitrate group C at $z = 0$ and its six coordinating Co(sep) cages at $z = \pm 1/4$, as indicated. The shortest intermolecular contacts are C-H \cdots O hydrogen bonds (blue dashed lines) and C-H \cdots H-C contacts (grey dashed lines).

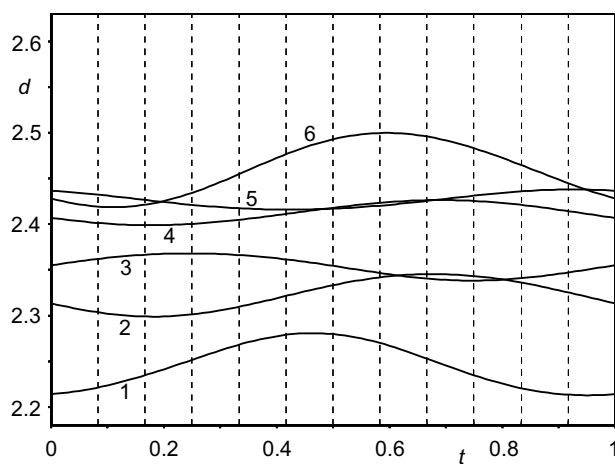


Figure 5.11: t -Plot of interatomic distances d (Å) between the O atom of nitrate C and hydrogen atoms of the sepulchate cage. Vertical, dashed lines indicate t values corresponding to the distances in the 12-fold supercell. Six C-H \cdots O contacts are shown (compare Fig. 5.1): 1=O91a \cdots H2c42, 2=O91/1a \cdots H2c44, 3=O91/3a \cdots H2c43, 4=O91/1a \cdots H2c45, 5=O91/3a \cdots H2c46, and 6=O91a \cdots H2c41.

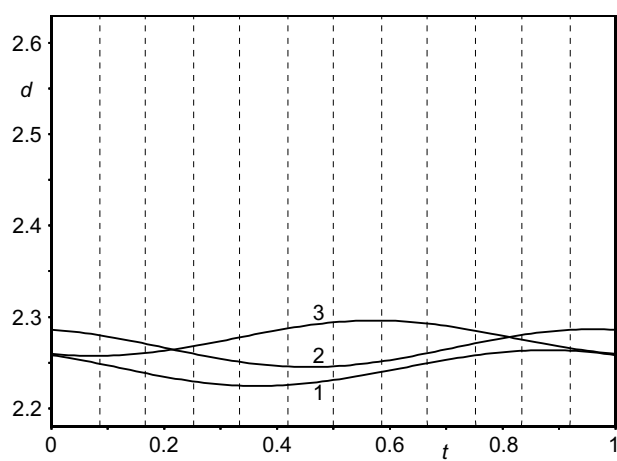


Figure 5.12: t -Plot of interatomic distances d (Å) between the hydrogen atoms attached to apical carbon atoms of neighbouring sepulchrate molecules. Vertical, dashed lines indicate t values corresponding to the distances in the 12-fold supercell. 1=H1c42··H1c43; 2=H1c41··H1c44; 3=H1c45··H1c46;

5.4 Conclusion

The 12-fold superstructure of Λ -cobalt(III) sepulchrate trinitrate at $T = 95$ K has successfully been described within the superspace approach. The superspace approach effectively removes correlations between crystallographically independent parameters of this high- Z' structure with $Z' = 12$.

Major difference between phase I—stable at ambient conditions—and phase IV—stable below 98 K—is the order of nitrate group C (Fig. 5.4). At room temperature nitrate group C exhibits at least sixfold orientational disorder, while in phase IV this nitrate group is fully ordered in 12 different orientations in the 12-fold supercell (Fig. 5.7).

The origin of the modulation is argued to lie in the avoidance of repulsive interactions rather than hydrogen bonding between neighbouring molecules. The shortest interatomic contacts are C–H···O weak hydrogen bonds (Figs. 5.9 and 5.11) and C–H···H–C intermolecular hydrogen atom contacts (Fig. 5.12). Intermolecular N–H···O hydrogen bonds do exist (Fig. 5.9), but they are long and weak, apparently prevented from full development by the short intermolecular contacts described above.

5.5 Acknowledgement

We thank Prof. Alan M. Sargeson for the donation of single crystals of Co(sep)(NO₃)₃. Assistance of Martin Tolkien in the diffraction experiments at beamline D3 of Hasylab at DESY, Hamburg is gratefully acknowledged. Financial support has been obtained from the German Science Foundation (DFG) under grant number SCHO 830/3-1.

Chapter 6

Intermediate low temperature phases of Λ -Co(III) sepulchrates trinitrate

In the course of this chapter the two intermediate low temperature phases II and III of Λ -Co(III) sepulchrates trinitrate are reported. Diffraction images collected at $T_1 = 115$ K (Phase II) and $T_2 = 100$ K (Phase III) are analysed to find out crystal symmetry in these phases. The incommensurately modulated structure in phase III is solved within the (3+1)-dimensional superspace approach. Crystal-chemical analysis is done to understand relations between phase I (room temperature phase), phase III and phase IV (low temperature lock-in phase)

6.1 Single-crystal X-ray diffraction

Single crystal X-ray diffraction experiments were performed at $T_1 = 115$ K (phase II) using a four circle *K*appa geometry diffractometer at beamline F1 and at $T_2 = 100$ K (phase III) using a four circle Euler geometry diffractometer at beamline D3 in Hasylab DESY, Hamburg. Data collection were done by φ and ω scans with several detector offsets and exposure times employing a radiation of wavelength, $\lambda = 0.60$ Å using MAR-CCD detectors (Table 6.1).

Table 6.1: Experimental data at $T = 100$ K, phase III.

Crystal data	
Chemical formula	[Co(C ₁₂ H ₃₀ N ₈)](NO ₃) ₃
M_r	531.4
Crystal dimensions (mm ³)	0.30 x 0.15 x 0.10
Crystal system	Monoclinic c -unique
Superspace group	$C2_1(\sigma_1\sigma_2)0$
T_2 (K)	100.0 (3)
a, b, c (Å)	8.4181(3), 14.5950(2), 15.6886(2)
γ (deg)	89.9958(10)
V (Å ³)	1927.54(8)
Modulation wave-vector, \mathbf{q}	0.176679(21) a *
Z	4
Data collection	
Radiation type	Synchrotron
Wavelength (Å)	0.60
μ (mm ⁻¹)	0.61
$[\sin(\theta)/\lambda]_{\max}$ (Å ⁻¹)	0.77
$\Delta\varphi, \Delta\omega$ (deg)	1, 1
Exposure times (s)	10, 20, 30, 40, 60, 120
Absorption correction	empirical, multiscan
Criterion of observability	$I > 3\sigma(I)$
$R_{\text{int}}, R_{\sigma}$	
all reflections (obs/all)	0.0371/0.0446, 0.0541/0.1017
$m = 0$	0.0235/0.0235, 0.0439/0.0449
$m = \pm 1$	0.0970/0.1081, 0.0916/0.1793
$m = \pm 2$	0.1629/0.3903, 0.1978/1.3526

6.1.1 Data integration and analysis of diffracted peaks

In chapter 5 section 5.2, we have briefly discussed the loss of symmetry from hexagonal to monoclinic in phase IV of $\text{Co}(\text{sep})(\text{NO}_3)_3$. Here we discuss in more detail the symmetry lowering of the crystal in phases II and III.

Data processing has been performed with the software EVAL15 (Schreurs et al., 2010). From the first inspection of the frames collected in phase II and III, main reflections were found regularly surrounded by satellite reflections up to second order. All reflections could be uniquely indexed using five integers ($hklm_1m_2$) on a primitive hexagonal lattice and with modulation wave vectors \mathbf{q}^1 , \mathbf{q}^2 and their linear combination \mathbf{q}^3 (eq. 6.1)

$$\begin{aligned}\mathbf{q}^1 &= (\sigma_h, \sigma_h, 0) \\ \mathbf{q}^2 &= (-2\sigma_h, \sigma_h, 0) \\ \mathbf{q}^3 &= -\mathbf{q}^1 - \mathbf{q}^2 = (\sigma_h, -2\sigma_h, 0)\end{aligned}\tag{6.1}$$

Absorption correction was performed with program SADABS (Bruker, 2008). Lattice parameters ($a_h = b_h$ and $\alpha = \beta = 90$ deg, $\gamma = 120$ deg) and reflection conditions ($00l00$): $l = 2n$ indicate the superspace group $P6_322(\sigma\sigma 0)000(-2\sigma\sigma 0)000$ No. 182.2.83.4 (Stokes et al., 2011; van Smaalen et al., 2013). Upon averaging all reflections using this superspace group symmetry, internal agreement factors for the observed first and second order satellite reflections are found to be unusually large (for phase II $R_{\text{int}}(m = 0) = 0.0301$, $R_{\text{int}}(m = \pm 1) = 0.2915$, $R_{\text{int}}(m = \pm 2) = 0.4485$ and for phase III $R_{\text{int}}(m = 0) = 0.0348$, $R_{\text{int}}(m = \pm 1) = 0.2383$, $R_{\text{int}}(m = \pm 2) = 0.3433$).

Data analysis revealed that the intensities of satellite reflections referring to the modulation wave vectors \mathbf{q}^1 , \mathbf{q}^2 and \mathbf{q}^3 are unequal. The ratio of the average intensities of the satellite reflections are $I_{\mathbf{q}^1}:I_{\mathbf{q}^2}:I_{\mathbf{q}^3} \approx 12:14:13$ for phase II and $I_{\mathbf{q}^1}:I_{\mathbf{q}^2}:I_{\mathbf{q}^3} \approx 10:14:15$ for phase III. Such difference in intensity is not allowed in hexagonal symmetry as these satellite reflections are related by six-fold rotation axis. In addition, satellite reflections of mixed second order were not observed in the diffraction pattern. These mixed second order satellite reflections run along directions which are along diagonals of \mathbf{q}_1 and $-\mathbf{q}_2$, \mathbf{q}_2 and $-\mathbf{q}_3$ and \mathbf{q}_3 and $-\mathbf{q}_1$ in a hexagonal cell (Fig. 6.1).

In an alternate setting, diffraction pattern was indexed using three C -centered $a \times \sqrt{3}b \times c$ orthohexagonal unit cells (see schematic representation of orthohexagonal

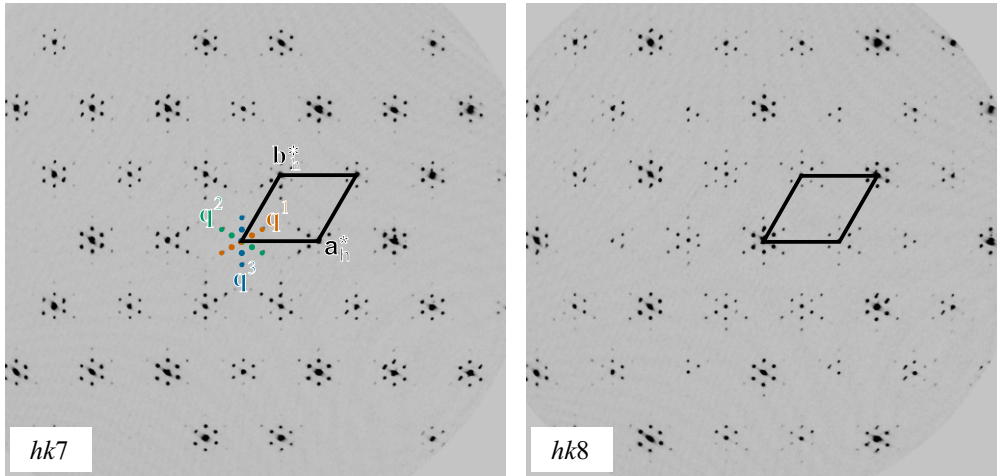


Figure 6.1: ($hk7$) and ($hk8$) layer of the diffraction pattern in phase II. Main reflections are regularly surrounded by satellite reflections up to second order. Mixed second order satellite reflections in hexagonal cell are missing. Further explanation in text.

cell in Fig. 5.2 in chapter 5). These three orthorhombic domains are rotated by 120 deg with respect to each other. Main reflections of all three domains superpose while satellite reflections are from a single domain. Applying the orthohexagonal transformation the modulation wave vector of the orthorhombic domains transforms to $\mathbf{q} = (\sigma_o, 0, 0)$ with $\sigma_o = 2\sigma_h$.

The description of the modulated structure reduces from (3+2)-dimensions to (3+1)-dimensions. Data integration has been performed within the hexagonal setting employing two modulation wave-vectors to get accurate intensities of the overlapped reflections and also because the program SADABS is not compatible for both twinned and modulated dataset.

Analysis of the reflection conditions for the data in phase II, ($hklm$) : $k + l = 2n$; ($00lm$) : $m = 2n$; ($h000$) : $h = 2n$ points towards orthorhombic superspace group $C222_1(\sigma_o00)s00$ No. 20.1.13.4 (standard setting $A2_122(00\sigma_o)00s$ in Stokes et al. (2011); van Smaalen et al. (2013)). Upon averaging all reflections using this superspace group, internal agreement factors for observed first and second order satellite reflections are still found to be large ($R_{\text{int}}(m = 0) = 0.0159$, $R_{\text{int}}(m = \pm 1) = 0.2277$, $R_{\text{int}}(m = \pm 2) = 0.3360$). The average significance ($\langle I/\sigma I \rangle$) of the satellites are significantly lower ($R_{\sigma}(m = 0) = 0.0249$, $R_{\sigma}(m = \pm 1) = 0.0696$, $R_{\sigma}(m = \pm 2) = 0.1437$).

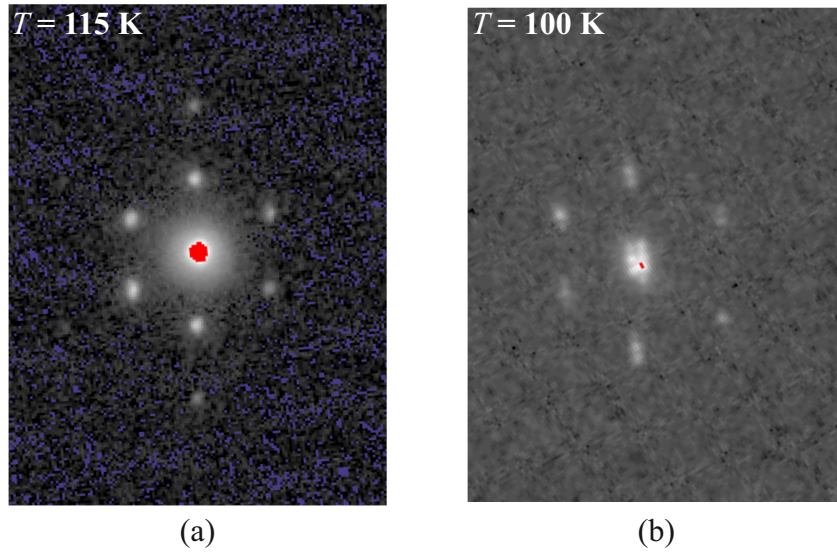


Figure 6.2: Section of measured frames for (a) phase II and (b) phase III. In (a) the main reflection and the satellite reflections appear to be single spots. In (b) six diffraction maxima appear at position of the main reflections and two maxima at the positions of satellite reflections.

Careful inspection of the frames collected in phase III shows that at positions of main reflections, reflections from six domains appear to overlap and at positions of the satellite reflections, reflections from two domains appear to overlap (Fig. 6.2(b)). This feature of the diffraction pattern is a hint of monoclinic symmetry of the crystal in phase III. Also, refinement of the lattice parameters using six pseudo-orthohexagonal cells against diffraction peaks resulted in $\gamma = 90 - 0.0042(10)$ which means that the measure of obliqueness of the monoclinic angle is larger than three times its standard uncertainties.

Based on our observations in phase III, reflections in phase II were also averaged against the superspace group monoclinic \mathbf{c} -unique $C2_1(\sigma_1\sigma_2)0$, ($\sigma_1 = \sigma_o$ and $\sigma_2 = 0$) No. 4.1.2.1 (standard setting $P2_1(\sigma_1\sigma_2)0$ in Stokes et al. (2011); van Smaalen et al. (2013)). This monoclinic superspace group is a subgroup of the orthorhombic superspace group. The agreement between the internal agreement factors and average significance of the satellite reflections are much closer now ($R_{\text{int}}(m = 0) = 0.0159$, $R_{\text{int}}(m = \pm 1) = 0.1148$, $R_{\text{int}}(m = \pm 2) = 0.1474$ and $R_{\sigma}(m = 0) = 0.0252$, $R_{\sigma}(m = \pm 1) = 0.0723$, $R_{\sigma}(m = \pm 2) = 0.1519$).

We propose that the symmetry of the crystal in both phases II and III is monoclinic. Structural analysis of phase II is in progress. Here we present the results of phase III.

6.1.2 Structure solution and refinement of phase III

Structure solution using the software SUPERFLIP (Palatinus and Chapuis, 2007) failed to converge due to presence of pseudo-merohedral twin domains. Structure refinements have been performed using the software JANA2006 (Petricek et al., 2014). Refinement using the model of phase IV as starting model against the present dataset failed to converge due to large correlations between structural parameters.

We overcame this problem by refining the basic structure of phase IV with isotropic ADPs for atoms as average structure against main reflections of the present dataset ($R_F^{\text{obs}}(m=0) = 0.1427$). In this model, the Co(sep) cage is defined by individual atoms while rigid body description was used for the nitrate groups. Nitrate groups A and B were considered a single rigid group at two different positions while a second rigid group was used to describe nitrate group C.

Small initial values for the first harmonic of displacive modulation for all atoms in the cage and rotational and translation modulation for the rigid groups were introduced. Refinement was performed against main and first order satellite reflections. Distance and angle calculations revealed that trigonal planar symmetry is not satisfied for the nitrate group C (unequal N–O distances and $\angle(\text{O–N–O}) \neq 120$ deg for all t -sections) but for nitrate groups A and B. The reason is that the nitrate group C is strongly modulated which under the rectilinear approximation of rigid body approach in JANA2006 cannot guarantee rigid conditions. Hence, the nitrate group C was treated as an atomic model with distance and angle restraints. Like for the Co(sep) cage small initial values for the first harmonic of displacive modulation were introduced for the atoms of nitrate group C. Refinement against main and first order satellite reflections converged with improved fit to the main reflections ($R_F^{\text{obs}}(m=0) = 0.0795$ and $R_F^{\text{obs}}(m = \pm 1) = 0.1051$).

In the next step, second harmonic for displacive modulation were added for all atoms in the Co(sep) cage and nitrate group C along with second harmonic for translation and rotation of nitrate groups A and B. Second order satellite reflections were included and refinement resulted in improved fit to main and first order satellite reflections ($R_F^{\text{obs}}(m=0) = 0.0783$, $R_F^{\text{obs}}(m = \pm 1) = 0.0966$ and

Table 6.2: Crystallographic data at $T = 100$ K, phase III.

Refinement	
No. of reflections used (obs/all)	20504/67028
GoF (obs/all)	2.04/1.27
$R_F^{\text{obs}}/wR_F^{\text{all}}$	
(all reflections)	0.0684/0.0822
$ m = 0 $	0.0496/0.0605
$ m = 1 $	0.0814/0.0834
$ m = 2 $	0.1222/0.1860
Twin volumes	
1/2/3/	0.1859(18)/0.2122(9)/0.1096(8)/
4/5/6	0.1813(9)/0.1881(8)/0.1229(8)
No. of parameters	661
H-atom treatment	mixture of restraints and constraints
$\Delta\rho_{\text{min}}/\Delta\rho_{\text{max}}$ ($\text{e}/\text{\AA}^3$)	-1.71/1.52

$R_F^{\text{obs}}(m = \pm 2) = 0.1372$). Fit to the diffraction data improved significantly after refining the model described by anisotropic ADP parameters for all non-hydrogen atoms and TLS parameters (Schomaker and Trueblood, 1968) for the rigid groups ($R_F^{\text{obs}}(m = 0) = 0.0528$, $R_F^{\text{obs}}(m = \pm 1) = 0.0821$ and $R_F^{\text{obs}}(m = \pm 2) = 0.1256$).

Analysis of the structural model revealed that eight non-hydrogen atoms including the Co atom inside the cage have non-positive definite ADPs. This problem was partially solved after introducing the first harmonic for the modulation of the ADPs of the Co atom with little improvement of the statistical parameters for refinement (three atoms including the Co atom still have non-positive definite ADPs). Refinement of the structural model after having introduced the first harmonic for the modulation of the third order anharmonic ADPs solved this problem completely with significant improvement of the fit to main reflections ($R_F^{\text{obs}}(m = 0) = 0.0496$, $R_F^{\text{obs}}(m = \pm 1) = 0.0816$ and $R_F^{\text{obs}}(m = \pm 2) = 0.1215$). Finally, isotropic secondary extinction correction improved the fit to the diffraction data further (Table 6.2).

6.2 Discussion

We have used the same restraints for the atoms inside the Co(sep) cage as for the model in phase IV (chapter 5). Treatment of the nitrate groups A and B as rigid groups are also same as in phase IV (refined distances $d_{\text{N-O}} = 1.24 \text{ \AA}$). An alternate free atom model for nitrate C with distance and angle restraints is justified in the sense of stable refinement of the model and chemically meaningful chemistry of this nitrate group (refined distances $d_{\text{N-O}} = 1.20 \text{ \AA}$).

Variation of distances between non-bonded atoms in the present model are larger than that in phase IV. Maximum variation in distances between Co1 and N_{ap} (N_{ap} = N51, N52) is 0.062 \AA (Fig. 6.3(a)) as compared to 0.030 \AA in phase IV. For the distances $d_{\text{Co1-C}_{\text{en}}}$ (C_{en} = C31 through to C36)) maximum variation is 0.082 \AA (0.027 \AA in phase IV) and for distances $d_{\text{Co1-C}_{\text{ap}}}$ (C_{en} = C41 through to C46) the maximum variation is 0.067 \AA (Fig. 6.3(b)) (0.030 \AA in phase IV).

In between the rigid groups the variations in distances is largest for that of the centers of the cage and nitrate group C (compare Fig. 6.4(b) to (a)).

The remarkable difference of the present model to the model in phase IV is observed in the N_{lig}-Co-N_{lig} angles (non-restrained) of the Co(N_{lig})₆ distorted octahedron. The variations are as large as 4.20 deg (Fig. 6.5) as compared to 0.95 deg in phase IV. The variation of $\Delta\angle(\text{N21-Co1-N26}) = 4.2 \text{ deg}$ and $\Delta\angle(\text{N21-Co1-N23}) = 3.8 \text{ deg}$ are complementary (Fig. 6.5) which indicates flexing and contraction nature of the Co(N_{lig})₆ distorted octahedron in the present model.

The effect of modulation is largest at the site of the nitrate group C. The rotation of its plane out of the (**a**, **b**)-plane ranges from 3.8 to 36.9 deg (Fig. 6.6) (rotation range 2.8 – 14.9 deg in phase IV).

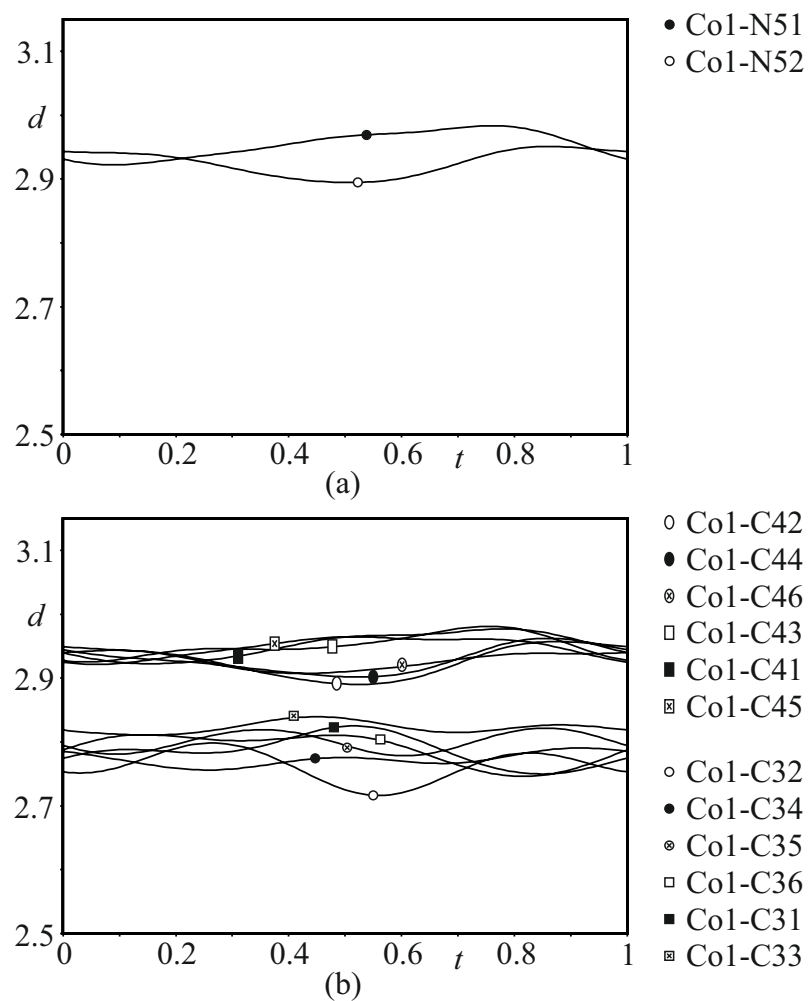


Figure 6.3: t -Plots of distances between the Co1 atom and (a) capping nitrogen atoms N_{ap} (N51, N52), (b) ethylene carbon atoms C_{en} (C31 to C36) and apical carbon atoms C_{ap} (C41 to C46).

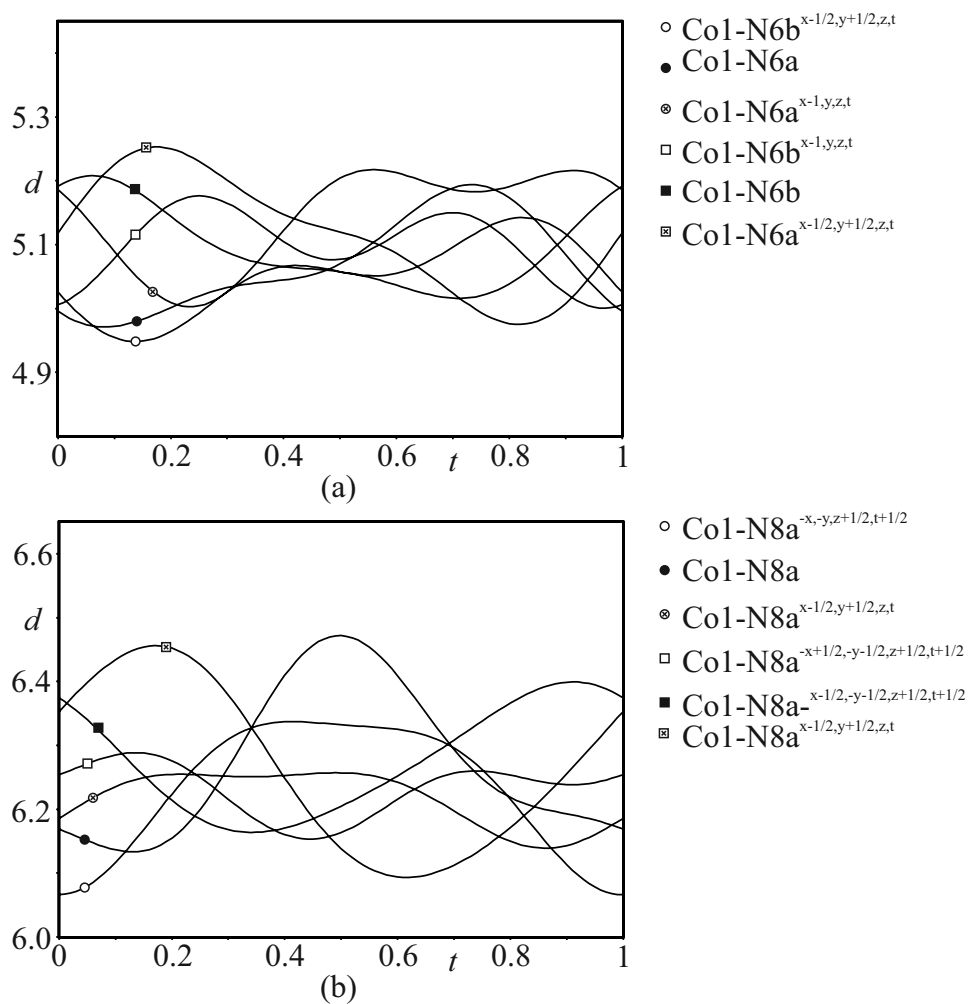


Figure 6.4: t -Plots of distances between the Co1 atom and (a) nitrogen atoms of nitrate group A (N6a) and B (N6b) and (b) nitrogen atom of nitrate group C (N8a).

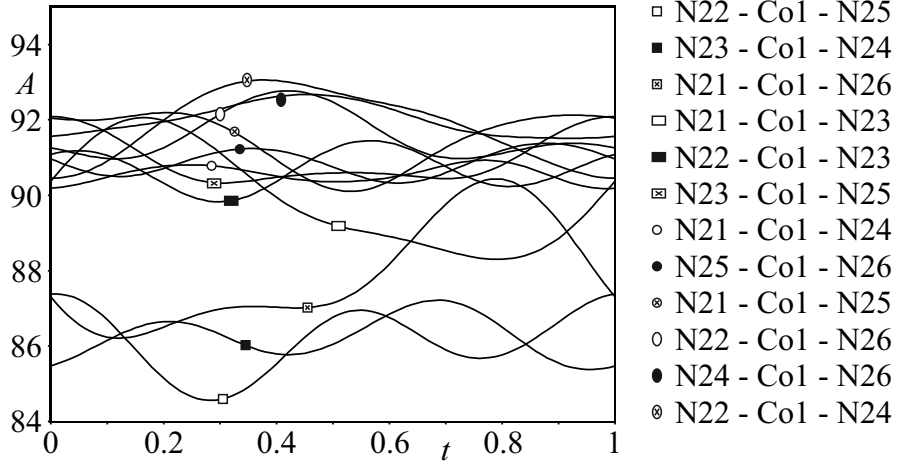


Figure 6.5: t-Plot of angles $N_{\text{lig}}-\text{Co1}-N_{\text{lig}}$ (deg), involving the six coordinating nitrogen atoms N_{lig} (N21 through to N26).

6.2.1 Monoclinic distortion

The monoclinic angle is $\gamma \simeq 90$ deg. Monoclinic twin volume sets of a single orthohexagonal domain also have values which are more or less equal to each other (compare twin volumes 1 and 4, 2 and 5, 3 and 6 in Table 6.2).

The modulations being pronounced can be used to justify the monoclinic distortion of the lattice. Consider that the lattice is orthorhombic and the superspace group symmetry is $C222_1(\sigma 00)s00$. Under the symmetry two-fold rotation axis parallel \mathbf{b} -axis the phase of the modulation wave is inverted, $\epsilon = -1$. (eq. 6.2)

$$\begin{pmatrix} -1 & 0 & 0 \\ 0 & 1 & 0 \\ 0 & 0 & -1 \end{pmatrix} \cdot \begin{pmatrix} \sigma \\ 0 \\ 0 \end{pmatrix} = \begin{pmatrix} -\sigma \\ 0 \\ 0 \end{pmatrix} \quad (6.2)$$

In the hypothetical case of orthorhombic lattice nitrate groups A and B are related by this symmetry operator $(2_y, \bar{1})$. Due to the phase inversion intrinsic shift along \mathbf{a}_{s4} associated with $(2_y, \bar{1})$ has to be zero. Consider that the origin lies on the symmetry element $(2_y, \bar{1})$ which implies that the origin-dependent translation is also zero. The symmetry operator in superspace is then given by its Seitz symbol $\{2_y, \bar{1}|0,0,0\}$. Coordinates of nitrate group A ($\mathbf{x}_s(\text{A})$) are transformed to coordinates of nitrate group B ($\mathbf{x}_s(\text{B})$) as (van Smaalen, 2012):

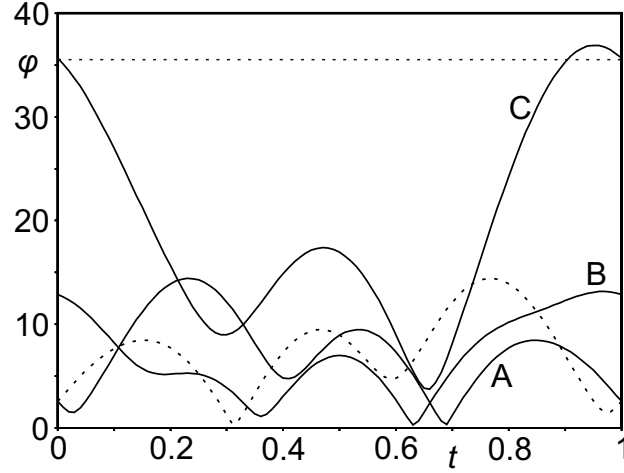


Figure 6.6: (a) t -plot of the angles of rotation of the planes of (a) nitrate group A (b) nitrate group B (c) nitrate group C out of the (\mathbf{a}, \mathbf{b}) -plane. Horizontal dashed line at $\varphi = 35.6$ deg show the angle of rotation of nitrate group C at room temperature while that for A and B is 0 deg. Dashed curve shows the angle of rotation of nitrate group B in orthorhombic symmetry.

$$\begin{pmatrix} x_{s1}(B) \\ x_{s2}(B) \\ x_{s3}(B) \\ x_{s4}(B) \end{pmatrix} = \begin{pmatrix} -1 & 0 & 0 & 0 \\ 0 & 1 & 0 & 0 \\ 0 & 0 & -1 & 0 \\ 0 & 0 & 0 & -1 \end{pmatrix} \cdot \begin{pmatrix} x_{s1}(A) \\ x_{s2}(A) \\ x_{s3}(A) \\ x_{s4}(A) \end{pmatrix} = \begin{pmatrix} -x_{s1}(A) \\ x_{s2}(A) \\ -x_{s3}(A) \\ -x_{s4}(A) \end{pmatrix} \quad (6.3)$$

The displacive modulation of nitrate A, \mathbf{u}^A transforms to that of B, \mathbf{u}^B as (van Smaalen, 2012):

$$\begin{pmatrix} u_1^B(x_{s4}) \\ u_2^B(x_{s4}) \\ u_3^B(x_{s4}) \end{pmatrix} = \begin{pmatrix} -1 & 0 & 0 \\ 0 & 1 & 0 \\ 0 & 0 & -1 \end{pmatrix} \cdot \begin{pmatrix} u_1^A(\epsilon^{-1}x_{s4}) \\ u_2^A(\epsilon^{-1}x_{s4}) \\ u_3^A(\epsilon^{-1}x_{s4}) \end{pmatrix} = \begin{pmatrix} -u_1^A(-x_{s4}) \\ u_2^A(-x_{s4}) \\ -u_1^A(-x_{s4}) \end{pmatrix} \quad (6.4)$$

The relations in the case of the hypothetical orthorhombic symmetry being established the monoclinic distortion will be explained considering the rotational property of the nitrate groups A and B out of the (\mathbf{a}, \mathbf{b}) -plane in the present phase III (Fig. 6.6). In this case, displacive modulation of these nitrates can be neglected along \mathbf{c} . Displacive modulation along \mathbf{b} should be equal (eq. 6.4) With $x_{s4}(A) = t + \sigma x_1(A)$

and $x_{s4}(B) = -t - \sigma x_1(B) = -t + \sigma x_1(A)$, displacement of B along **a** in section $-t$ should be opposite to the displacement of A along **a** in section t . The amplitude of rotation should follow the equality condition: $\varphi_A(t = t') = \varphi_B(t = 1 - t')$. This condition is not fulfilled in the present phase III (Fig. 6.6). Deviation of this equality condition is maximum at $t = 0.71$, $\Delta\phi = 10.7$ deg (Fig. 6.6).

6.2.2 Intermolecular interactions

In phase IV, the nitrate groups were found rotated out of the (**a**, **b**)-plane to a maximum of 5 deg (chapter 5). In the present model these rotations are larger (0.4 to 14.4 deg for A and 0.3 to 13.3 deg for B) (Fig. 6.6) Distances $d_{H...O}$ involving the N–H...O bonds are in the range 2.24 to 2.72 Å (Fig. 6.7) which shows they are in both weaker and moderate side of reported N–H...O bonds (Gilli and Gilli, 2009; Jeffrey, 1997, and references therein) and the variation are larger than in phase IV ($d_{H...O}$ in the range 2.4 – 2.6 Å). Also the variations in distances $d_{H...O}$ involving the C–H...O bonds are in the range 2.17 to 2.45 Å which are on the shorter side of reported C–H...O bonds (Desiraju and Steiner, 2001, and references therein) and these variations are larger than in phase IV ($d_{H...O} = 2.2 - 2.35$ Å)

The nitrate group C is ordered (disordered in phase I (Schönleber et al., 2010) and ordered in phase IV (chapter 5). This can be interpreted as six disordered orientations of this nitrate group in phase I gains more degrees of freedom by loss of higher hexagonal symmetry and freezes at the site of the six twin domains inside the crystal in phase III and in phase IV. From crystal-chemical analysis we found the ordering of the nitrate group C is due to increased packing density of the Co(sep) cages in the co-ordination sphere of this nitrate group which forces this nitrate group to freeze at only one site within each of the monoclinic twin domains. The evidence of such dense packing lies in short $C_{ap}-H...H-C_{ap}$ distances of ~ 2.25 Å (Fig. 6.8) between neighboring Co(sep) in the co-ordination sphere of this nitrate group. These nitrate groups too are involved in C–H...O bonds with the Co(sep) cages (Fig. 6.8). The variations in H...O distances are in range 2.16 to 2.67 Å. Dense packing of the Co(sep) cage neighbors has a strong effect on the modulation of the nitrate group C. The rotation of its plane out of the (**a**, **b**)-plane is as large as 36.9 deg. This feature of this nitrate group C is interesting owing to the value of 35.6 deg in phase I (Schönleber et al., 2010) which shows that it retains some property of phase I.

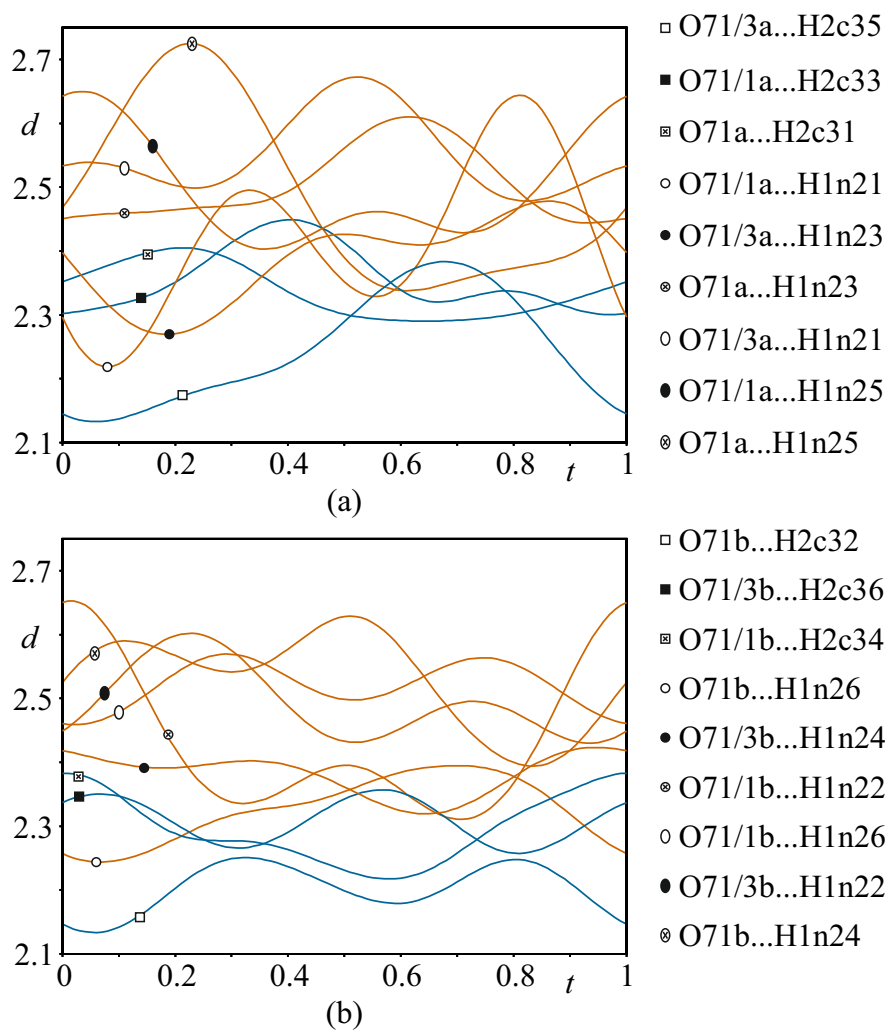


Figure 6.7: t -Plot of interatomic distances d (Å) between the O atom of nitrate (a) A and (b) B and hydrogen atoms of the sepulchrates cage. (see the environment of these nitrate groups in chapter 5).

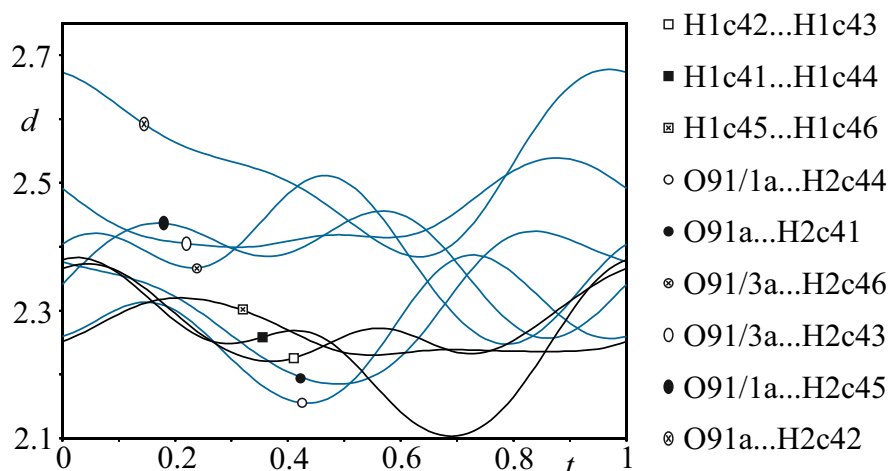


Figure 6.8: t -Plot of interatomic distances d (Å) between the O atom of nitrate C and hydrogen atoms of the sepulchrate cage and hydrogen atoms of different sepulchrate cages.

6.3 Conclusion

In phases II and III the crystal consists of six twin domains of transformation nature with monoclinic symmetry.

Variations in non-bonded distances between the atoms are larger than those in phase IV. The N–H \cdots O bonds between the Co(sep) cage and nitrate groups A and B show tendency of strengthening with H \cdots O distances as short as 2.24 Å as compared to phase I ($d_{\text{H}\cdots\text{O}} = 2.46$ Å (Schönleber et al., 2010)). Competition between the formation of N–H \cdots O bonds ($d_{\text{H}\cdots\text{O}} = 2.24 \sim 2.72$ Å) and the avoidance of repulsive C–H \cdots O interactions ($d_{\text{H}\cdots\text{O}} = 2.17 \sim 2.45$ Å) are stronger compared to that in phase IV where the variations are smaller (for the C–H \cdots O bonds $d_{\text{H}\cdots\text{O}} = 2.2 - 2.35$ Å and for the N–H \cdots O bonds $d_{\text{H}\cdots\text{O}} = 2.4 - 2.6$ Å).

Nitrate group C is strongly modulated as a result of optimizing its interactions with the Co(sep) cages. It appears that in such a dense environment of the nitrate group C, in phase III the rigid group rotates in order to avoid possible repulsions which are unfavourable for crystal packing.

Chapter 7

Summary

In this thesis, crystal structures of the two organic molecular compounds trimethyltin hydroxide (Me_3SnOH) and Λ -Co(III) sepulchrate trinitrate ($\text{Co}(\text{sep})(\text{NO}_3)_3$) are reported for different temperatures. Interplay between intermolecular and intramolecular forces and between different intermolecular forces are found to be the origin of modulation in these crystal structures. Employing the (3+1)-dimensional superspace formalism unique phase relations have been established between non-modulated phases and different modulated phases. Description of high Z' superstructures (where Z' is the number of molecules in the asymmetric unit) as commensurately modulated structures within the superspace formalism helped in removing correlations between structural parameters and in establishing complete physically and chemically meaningful structural models which are often problems in three-dimensional descriptions.

Me_3SnOH undergoes a phase transition from high Z' phase to low Z' phase upon cooling. Crystal structures of the low Z' phase and high Z' phase have been redetermined. Single-crystal X-ray diffraction experiments have been performed at $T_1 = 100$ K and $T_2 = 220$ K employing synchrotron radiation. One of the major discoveries is observation of diffuse scattering in layers in the diffraction pattern in both phases. Based on this observation the description of the high Z' phase reduced from 32-fold superstructure to eightfold superstructure in contrast to literature published earlier. Crystal structures of both phases have been described within (3+1)-dimensional superspace formalism as commensurately modulated structures using basic cell with $Z' = \frac{1}{2}$. Due to orthorhombic symmetry the description of the corresponding $\mathbf{a} \times \mathbf{b} \times 2\mathbf{c}$ superstructure reduces to $Z' = 1$ and of the $\mathbf{a} \times \mathbf{b} \times 8\mathbf{c}$ superstructure reduces to Z'

= 4. In the $Z' = 1$ superstructure inter-strand C–H...O bonds are discovered. These weak hydrogen bonds serve as pivot for the crystal packing and zigzag arrangement of the polymeric chains. The origin of multiple formula units ($Z' = 4$) in the eight-fold superstructure in the high Z' phase is argued to lie in the competition between dense packing of the formula units within the chain and optimal conformation of the hydroxy groups. This frustration within the polymeric chain is responsible for the distortion of zigzag planes. Intra-strand competitive forces and inter-strand H...H interactions prevent the formation of long range order in inter-strand C–H...O bonds. The disorder in both forms is proposed as shift of the chains with respect to another and arbitrary direction of the zigzag chains.

Complete scheme of phase transitions of $\text{Co}(\text{sep})(\text{NO}_3)_3$ is investigated. Single crystal X-ray diffraction experiments have been performed at $T_1 = 115$ K, $T_2 = 100$ K and $T_3 = 95$ K. Phases II ($\Delta T = 133$ – 107 K) and III ($\Delta T = 107$ – 98 K) are found incommensurately modulated and phase IV ($T < 98$ K) is commensurately modulated. The hexagonal symmetry of the high temperature phase is reduced in phase II, III and IV and six monoclinic twin domains are found in the crystal. The incommensurately modulated structure in phase III and commensurately modulated structure in phase IV are described within (3+1)-dimensional superspace approach using (monoclinic **c**-unique) superspace group $C2_1(\sigma_1\sigma_2)0$. The corresponding three-dimensional structure in phase IV is found to be a twelvefold superstructure ($Z' = 12$) of the room temperature hexagonal structure. Employing the superspace approach large correlations between structural parameters could be removed and save $\approx \frac{1}{5}$ of refinable parameters in comparison to the three-dimensional superstructure model. Crystal structures in phase III and in phase IV are completely ordered owing to dense packing of the cations and anions in contrast to the room temperature structure. The origin of modulation is argued to lie in the avoidance of repulsive C–H...O interactions rather than formation of attractive N–H...O bonds between $\text{Co}(\text{sep})$ cages and two nitrate groups. The effect of modulation is largest at the site of the third nitrate group driven by C–H...H–C interactions between $\text{Co}(\text{sep})$ cages in the co-ordination sphere and C–H...O bonds between this nitrate group and $\text{Co}(\text{sep})$ cages.

Chapter 8

Zusammenfassung

Diese Arbeit berichtet über die Kristallstrukturen der metallorganischen Verbindungen Trimethylzinnhydroxid (Me_3SnOH) und Λ -Co(III)-sepulchrat-trinitrat ($\text{Co}(\text{sep})(\text{NO}_3)_3$) in ihren jeweils modulierten Phasen. Das Zusammenspiel von intra- und intermolekularen Kräften und verschiedenen intermolekularen Kräften wurde als Ursache der Modulation in diesen Strukturen gefunden. Durch Anwendung der (3+1)-dimensionalen Superraummethode wurden eindeutige Beziehungen zwischen nicht modulierten und verschiedenen modulierten Phasen gefunden. Die Beschreibung von Überstrukturen mit hohem Z' (Z' stellt die Anzahl von Molekülen in der asymmetrischen Einheit) als kommensurabel modulierte Strukturen mit der Superraummethode half Korrelationen zwischen Strukturparametern zu reduzieren und sowohl chemisch als auch physikalisch sinnvolle Strukturmodelle zu etablieren, was oft schwierig ist.

Beim Abkühlen durchläuft Me_3SnOH eine Phasenumwandlung von einer Überstruktur mit hohem Z' zu einer mit niedrigem Z' . Die Kristallstruktur von beiden Phasen wurde neu bestimmt. Einkristallbeugungsexperimente wurden bei $T_1 = 100$ K und $T_2 = 220$ K mit Hilfe von Synchrotronstrahlung durchgeführt. Eine der wesentlichsten Entdeckungen dieser Arbeit war die Beobachtung von diffuser Streuung in Schichten in den Beugungsbildern der beiden Phasen. Gestützt auf diese Beobachtung wurde die Beschreibung der Überstrukturen mit hohem Z' von einer 32-fachen Überstruktur zu einer achtfachen reduziert und damit wurde von der literaturbekannten Strukturbeschreibung abgewichen. Die Strukturen von beiden Phasen wurden mit der (3+1)-dimensionalen Superraummethode beschrieben indem eine Basiszelle mit $Z' = \frac{1}{2}$ verwendet wurde. Durch die orthorhombische Symme-

trie reduziert sich die Beschreibung der entsprechenden $\mathbf{a} \times \mathbf{b} \times 2\mathbf{c}$ Überstruktur zu $Z' = 1$ und die der $\mathbf{a} \times \mathbf{b} \times 8\mathbf{c}$ Überstruktur zu $Z' = 4$. In der $Z' = 1$ Überstruktur wurden zwischen den Ketten C–H...O-Bindungen entdeckt. Diese schwachen Wasserstoffbrücken wirken als Angelpunkt für die Kristallpackungen und die Zickzack-Anordnung in polymeren Ketten. Die Ursache für mehrere Formeleinheiten ($Z' = 4$) in der achtfachen Überstruktur wird damit begründet, dass ein Wettstreit zwischen dem Erreichen einer möglichst dicht gepackten Struktur in den Ketten und dem Ermöglichen der optimalen Hydroxylgruppenkonformation besteht. Diese Frustration innerhalb der polymeren Kette ist verantwortlich für die Deformation der Zickzack-Ebenen. Konkurrierende Kräfte innerhalb der Stränge und H...H Wechselwirkungen zwischen den Strängen verhindern den Aufbau von langreichweitiger Ordnung in Zwischenstrang-C–H...O-Bindungen. Fehlordnung in beiden Formen wird als Verschiebung von Ketten gegeneinander jedoch in willkürlicher Richtung vorgeschlagen.

Das komplette Phasendiagramm von $\text{Co}(\text{sep})(\text{NO}_3)_3$ wurde bestimmt. Einkristallbeugungsexperimente wurden bei $T_1 = 115$ K, $T_2 = 100$ K und $T_3 = 95$ K bestimmt. Phasen II ($\Delta T = 133\text{--}107$ K) und III ($\Delta T = 107\text{--}98$ K) sind inkommensurabel moduliert und Phase IV ($T < 98$ K) ist kommensurabel moduliert. Die hexagonale Symmetrie der Hochtemperaturphase wird in den Phasen II, III und IV reduziert und sechs monokline Zwillingsdomänen wurden im Kristall gefunden. Die inkommensurabel modulierte Struktur in Phase III und die kommensurabel modulierte Struktur in Phase IV wurden mit der (3+1)-dimensionalen Superraummethode unter Zuhilfenahme der (monoklinen \mathbf{c} -unique) Raumgruppe $C2_1(\sigma_1\sigma_2)0$ beschrieben. Die entsprechende dreidimensionale Struktur der Phase IV wurde als zwölfache Überstruktur der bei Zimmertemperatur hexagonalen Struktur gefunden. Durch Anwendung der Superraummethode konnten starke Korrelationen zwischen Strukturparametern vermeiden und etwa ein fünftel der zu verfeinernden Parameter gegenüber des drei-dimensionalen Strukturmodells sparen. Im Gegensatz zur Struktur bei Zimmertemperatur sind die Strukturen in Phase III und IV durch eine dichte Packung von Kationen und Anionen vollständig geordnet. Als Ursache für die Modulation wird die Vermeidung von abstoßenden C–H...O Wechselwirkungen gegenüber der Bildung von anziehenden N–H...O-Bindungen zwischen $\text{Co}(\text{sep})$ Käfigen und zweier Nitratgruppen diskutiert. Am stärksten ist der Effekt der Modulation an der Stelle der dritten Nitratgruppe, was durch C–H...H–C Wechselwirkungen zwis-

chen Co(sep) Käfigen in der Koordinationssphäre und C–H...O-Bindungen zwischen dieser Nitratgruppe und Co(sep) Käfigen hervorgerufen wird.

Appendix A

Supplementary material: Trimethyltin hydroxide

Choice of superspace group

At first, main reflections were tested to find an appropriate three-dimensional space group for the basic structure. The lattice parameters and reflection conditions $(h, k, 0) : h + k = 2n$ and $(h, 0, 0) : h = 2n$ indicate an orthorhombic space group $P2_1mn$. This space group symmetry is a non-standard setting of $Pmn2_1$, No. 31 in the *International Tables for Crystallography, Vol. A*. An average structure at room temperature was described using this space group symmetry in the 1965 structure report [Kasai et al. \(1965\)](#).

In the next step satellite reflections were included. Lattice parameters, modulation wave vector and reflection conditions $(h, 0, l, m) : m = 2n$, $(h, k, 0, 0) : h + k = 2n$ and $(h, 0, 0, 0) : h = 2n$ point towards an orthorhombic non-centrosymmetric superspace group $P2_1mn(00\sigma)0s0$, No. 31.1.9.7 [Stokes et al. \(2011\)](#); [van Smaalen et al. \(2013\)](#).

A higher centrosymmetric superspace group symmetry $Pm\bar{m}n(00\sigma)0s0$, No. 59.1.9.2 ([Stokes et al., 2011](#); [van Smaalen et al., 2013](#)) follows the same reflection conditions $(h, 0, l, m) : m = 2n$, $(h, k, 0, 0) : h + k = 2n$ and $(h, 0, 0, 0) : h = 2n$. The non-centrosymmetric superspace group $P2_1mn(00\sigma)0s0$ is a subgroup of this centrosymmetric superspace group.

Structure refinements

The structure was solved in (3+1)-dimensional superspace by applying charge flipping algorithm ([Palatinus, 2013](#)) using the program SUPERFLIP ([Palatinus and Chapius, 2007](#)). The resulting electron density map revealed the position of the tin (Sn1) atom along with initial values for its atomic modulation function (AMF). The Sn1 atom was found to be centred on the mirror plane perpendicular to the \mathbf{a}_{s2} -axis.

Structure refinements have been performed using the software package JANA2006 ([Petricek et al., 2014](#)). In the beginning the incommensurate model was refined against main ($m = 0$) and first order satellite reflections ($m = \pm 1$) only. Refinement converged at $R_F^{\text{obs}}(m = 0) = 0.1306$ and $R_F^{\text{obs}}(m = \pm 1) = 0.1805$.

From the difference Fourier maps, positions of the oxygen and the carbon atoms were determined along with initial values of their AMFs. The oxygen atom (O1) and the carbon atom (C1) were found centred on the mirror plane perpendicular

b-axis and the second carbon atom (C2) in a general position. Refinement lead to an improved fit to the main reflections and first-order satellite reflections $R_F^{\text{obs}}(m = 0) = 0.1207$ and $R_F^{\text{obs}}(m = \pm 1) = 0.1474$. Average intensity $\langle I \rangle$ of the fourth-order satellite reflections are larger than those of the second and third-order satellite reflections (Fig. A.3) which hints that the contribution of the fourth harmonic of the AMFs to the structural model are probably larger in amplitude than second and third harmonic. Following this idea, fourth harmonic for displacive modulation were added for all the atoms. The model was refined against main, first and fourth-order satellite reflections which improved the fit to main and satellite reflections of first order ($R_F^{\text{obs}}(m = 0) = 0.1131$, $R_F^{\text{obs}}(m = \pm 1) = 0.1392$ and $R_F^{\text{obs}}(m = -4) = 0.3730$). In the next step, second and third harmonic were introduced and the model was refined including all the satellite orders. Refinement converged with improved fit to the main, first and fourth order satellite reflections ($R_F^{\text{obs}}(m = 0) = 0.1017$, $R_F^{\text{obs}}(m = \pm 1) = 0.1330$, $R_F^{\text{obs}}(m = \pm 2) = 0.1395$, $R_F^{\text{obs}}(m = \pm 3) = 0.2934$, $R_F^{\text{obs}}(m = -4) = 0.3406$). However, any attempts to refine the atomic displacement parameters (ADPs) anisotropic of the atoms led to non-positive definite ADPs for the light atoms. Also, refinement failed to converge when hydrogen atoms to the carbon atoms were added in fixed tetrahedral geometry with the Sn1 and carbon atoms. Analysis of the (3+1)-dimensional Fourier maps revealed that the electron densities of the oxygen and carbon atoms are discontinuous along x_4 . Sections (x_2, x_4) and (x_3, x_4) of the Fourier maps are continuous and the discontinuity is along (x_1, x_4) . On the other hand, electron density around the Sn1 atom is continuous (Fig. A.5).

This means that crenel (block-wave) functions are required to describe the electron densities of the atoms (Petricek et al., 2016). Positions of the atoms O1, C1 and Sn1 atoms were split each into four atomic positions (for example Sn1 is split to Sn1a, Sn1b, Sn1c and Sn1d) and the crenel functions describing the AMFs along x_4 are of equal width $\Delta x_4 = 0.125$. The position of the C2 atom was split into eight atomic positions (C2a, C2b, C2c, C2d, C3a, C3b, C3c, C3d). The centers of the crenel functions of the atoms Sn1a, O1a, C1a, C2a, C3a were restricted to be equal with respect to phase of modulation, t (center represented by t_{40} , see eq. A.1).

$$\begin{aligned}
t_{40}(\text{Sn1a}) &= t_{40}(\text{O1a}) \\
t_{40}(\text{C1a}) &= t_{40}(\text{O1a}) \\
t_{40}(\text{C2a}) &= t_{40}(\text{O1a}) \\
t_{40}(\text{C3a}) &= t_{40}(\text{O1a}) + 0.5
\end{aligned} \tag{A.1}$$

Same restrictions were also implemented for the atom codes ‘b’, ‘c’ and ‘d’. Occupation of the electron density along x_4 are completed by the intrinsic shift of $\frac{1}{2}$ associated with the mirror plane perpendicular \mathbf{a}_{s4} -axis (Symmetry code: $x_1, -x_2, x_3, x_4 + \frac{1}{2}$). Three hydrogen atoms to each of the carbon atoms were added by riding model in fixed tetrahedral geometry with the tin atom and their isotropic ADPs were constrained to be $U_{iso}(\text{H}) = 1.5U_{eq}(\text{C})$ of the parent carbon atom. Hydrogen atoms to the oxygen atoms were added applying distance and angle restraints $d(\text{O-H}) = 0.82 \pm 0.01 \text{ \AA}$ and $\angle(\text{Sn-O-H}) = 106 \pm 1 \text{ deg}$ and their isotropic ADPs were constrained to be $U_{iso}(\text{H}) = 1.5U_{eq}(\text{O})$. Refinement converged without any non-positive definite ADPs and improved fit to the main and satellite reflections ($R_F^{\text{obs}}(m = 0) = 0.0902$, $R_F^{\text{obs}}(m = \pm 1) = 0.1153$, $R_F^{\text{obs}}(m = \pm 2) = 0.1228$, $R_F^{\text{obs}}(m = \pm 3) = 0.1921$, $R_F^{\text{obs}}(m = -4) = 0.2304$). Finally all non-hydrogen atoms were described with anisotropic ADPs and the model was refined. Fit to the main and satellite reflections improved significantly ($R_F^{\text{obs}}(m = 0) = 0.0402$, $R_F^{\text{obs}}(m = \pm 1) = 0.0524$, $R_F^{\text{obs}}(m = \pm 2) = 0.0992$, $R_F^{\text{obs}}(m = \pm 3) = 0.1310$, $R_F^{\text{obs}}(m = -4) = 0.1638$).

To find out the correct symmetry of the equivalent three-dimensional eight-fold superstructure, the incommensurate model has to be transformed to commensurate and selecting a correct value of the initial phase of the modulation wave (t_0). The possible t_0 values are 0 and $\frac{1}{16}$ for a orthorhombic space group $P2_1cn$ of the equivalent superstructure. A general value of t_0 gives a monoclinic (**b**-unique) Pc of the equivalent superstructure. All three commensurate and the incommensurate models were refined using the dataset but with reflections averaged in monoclinic symmetry and the same number of parameters (=193). The model at $t_0 = 0$ and $t_0 = \frac{1}{32}$ (general value) fits best to the diffraction data and are significantly better than the incommensurate model. The model at $t_0 = \frac{1}{16}$ gives the worst statistical parameters (Table A.1). Both structural models at $t_0 = 0$ and $t_0 = \frac{1}{32}$ gives similar fit to the diffraction data. First harmonic for displacive modulation were superposed on the crenel functions describing the atoms for the $t_0 = \frac{1}{32}$ model which would then

describe the monoclinic distortion. However, refinement suffered from large correlations which resulted in a non-converging and oscillating refinement. Hence, the $t_0 = \frac{1}{32}$ model was discarded for further analysis.

In the next step, absorption correction was performed on the integrated dataset in orthorhombic point group symmetry (mmm), reflections were averaged in orthorhombic symmetry and the $t_0 = 0$ model was refined against the dataset. Refinement converged without significant changes in the statistical parameters ($R_F^{\text{obs}}(m = 0) = 0.0286$, $R_F^{\text{obs}}(m = \pm 1) = 0.0487$, $R_F^{\text{obs}}(m = \pm 2) = 0.0881$, $R_F^{\text{obs}}(m = \pm 3) = 0.1142$, $R_F^{\text{obs}}(m = -4) = 0.0706$). Isotropic secondary extinction correction was applied and fit to the main and satellite reflections improved marginally. The crystal is twinned by merohedry (inversion twin) Refinement of the twin volumes resulted in a value of 0.5 within its standard uncertainty (Flack parameter(Flack, 1983) = 0.42 (12)). Hence, the value was fixed to 0.5 and the final model was refined.

For the sake of comparison, free refinement of the three-dimensional superstructure model (equivalent of the $t_0 = 0$ commensurate model) was performed. Refinement suffered from large correlations between parameters for positions of the hydrogen atoms of the hydroxy groups. This problem was not encountered during refinement of the commensurate model because additional restrictions on the positions of the atoms in the internal dimension were used. This is not possible in superstructure refinement which demonstrates the advantage of superspace approach.

The following test was performed which is not considered for further analysis. Reflections were averaged against the centrosymmetric superspace group $Pm\bar{m}n(00\sigma)0s0$ and the incommensurate model was refined. Refinement suffered from oscillations due to large correlations between structural parameters and anisotropic ADPs of the non-hydrogen light atoms became non-positive definite. The fit to the diffraction data is worse ($R_F^{\text{obs}}(m = 0) = 0.0884$, $R_F^{\text{obs}}(m = \pm 1) = 0.5415$, $R_F^{\text{obs}}(m = \pm 2) = 0.3461$, $R_F^{\text{obs}}(m = \pm 3) = 0.6203$, $R_F^{\text{obs}}(m = -4) = 0.5584$). (Compare the statistical parameters for the incommensurate model in Table A.1) Refinement of the commensurate model ($t_0 = 0$, space group $Pm\bar{c}n$ of the equivalent 8-fold superstructure) suffered furthermore from singularities and a stable refinement was not achieved at all.

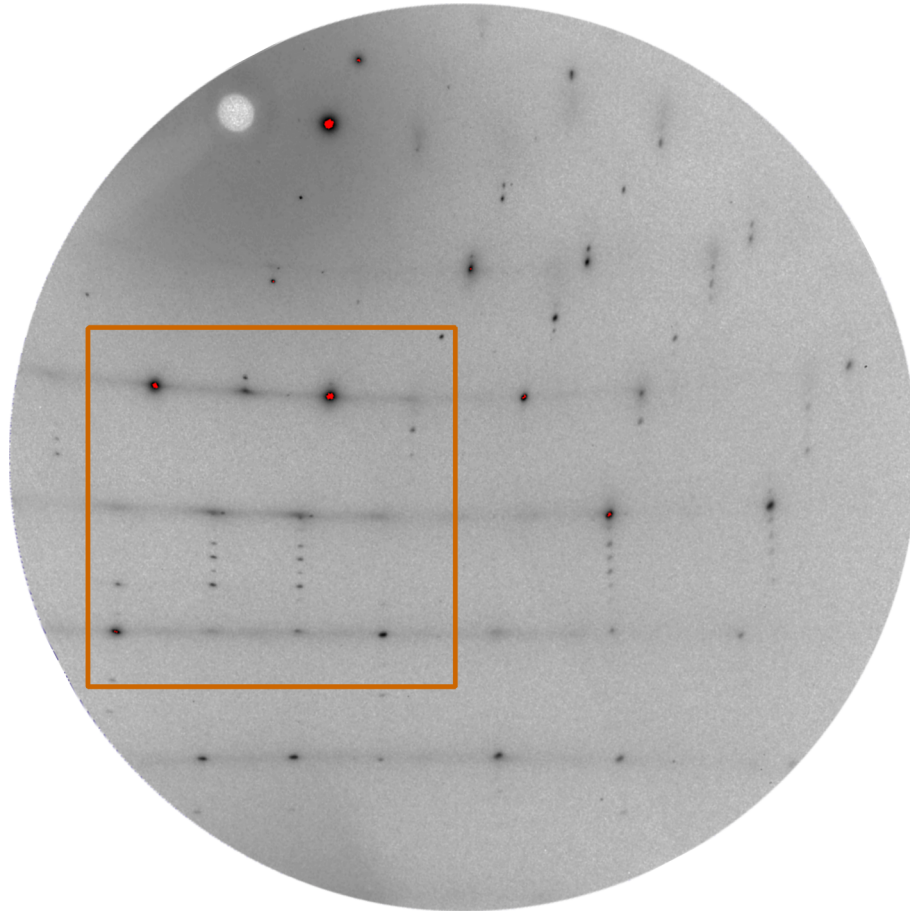


Figure A.1: A complete measured frame with part of it zoomed exhibiting strong main reflections ($hkl0$) and weaker superstructure reflections ($hkl \pm 1$, $hkl \pm 2$, $hkl \pm 3$ and $hkl \pm 4$) along with pronounced diffuse scattering in the layers defined by main reflections.

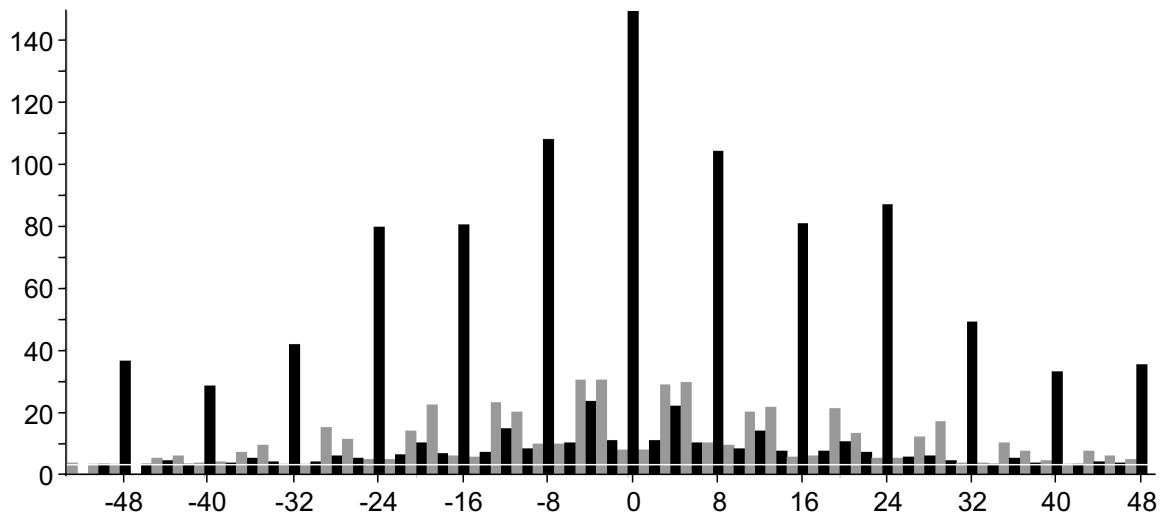


Figure A.2: Histogram plot of the average significance ($I/\sigma(I)$) as function of l -indices from data integration performed based on $2\mathbf{a} \times 2\mathbf{b} \times 8\mathbf{c}$ superstructure. $l = 0, \pm 8, \pm 16, \dots$ represents main reflections. From the plot, it is clearly visible that the the strongest satellites are at $\pm \frac{3}{8}l$ -indices in between the main reflections.

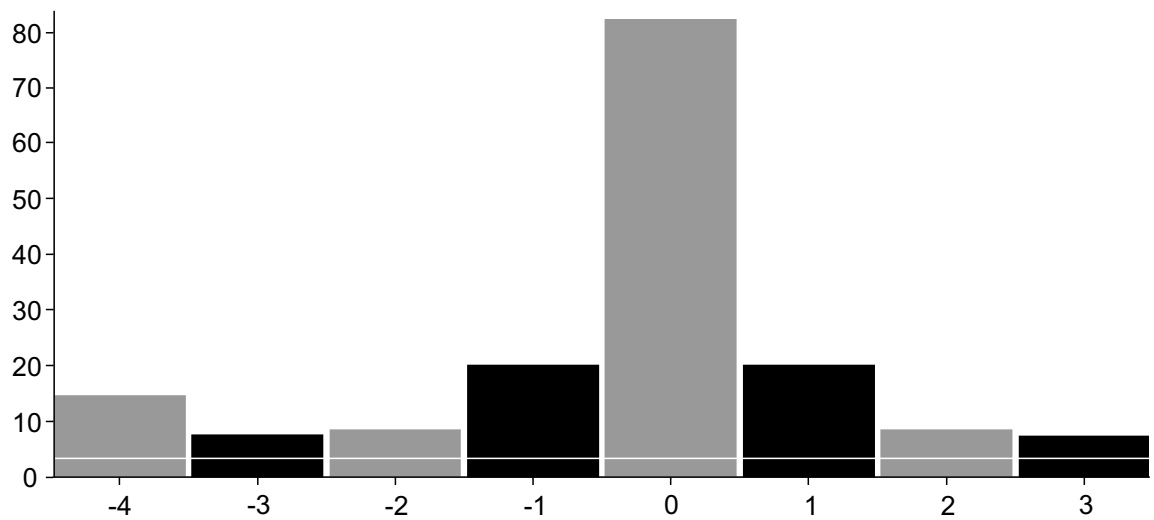


Figure A.3: Histogram plot of the average significance ($I/\sigma(I)$) as function of m -indices from data integration performed in $(3+1)$ -dimension superspace. \mathbf{q} -vector is chosen to be $\frac{3}{8}\mathbf{c}^*$. Intensity of the fourth order satellites are stronger than that of the second and third order.

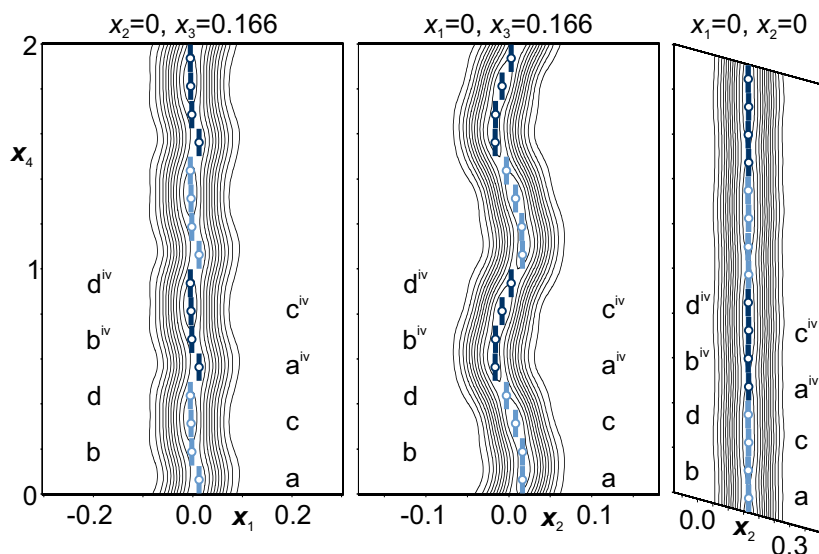


Figure A.4: Fourier maps along x_4 for atom Sn1 (light blue) and Sn1^{iv} (dark blue). Symmetry code: (iv) $x_1, -x_2, x_3, x_4 + \frac{1}{2}$. Positions of the relevant t -values are shown by open circles. The step of the contour line is $5 e/\text{\AA}^3$. The width of the maps are 4, 4 and 2 \AA .

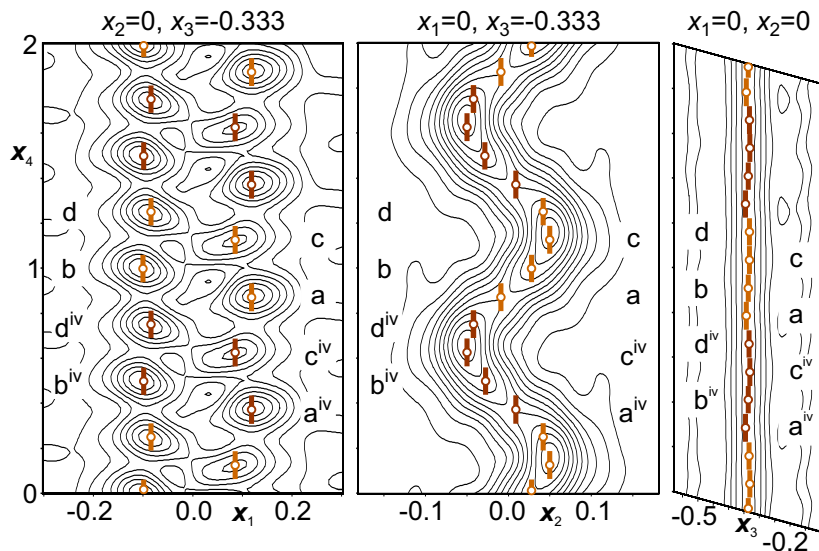


Figure A.5: Fourier maps along x_4 for atom O1 (orange) and O1^{iv} (dark brown). Symmetry code: (iv) $x_1, -x_2, x_3, x_4 + \frac{1}{2}$. Positions of the relevant t -values are shown by open circles. The step of the contour line is $0.25 e/\text{\AA}^3$. The width of the maps are 4, 4 and 2 \AA .

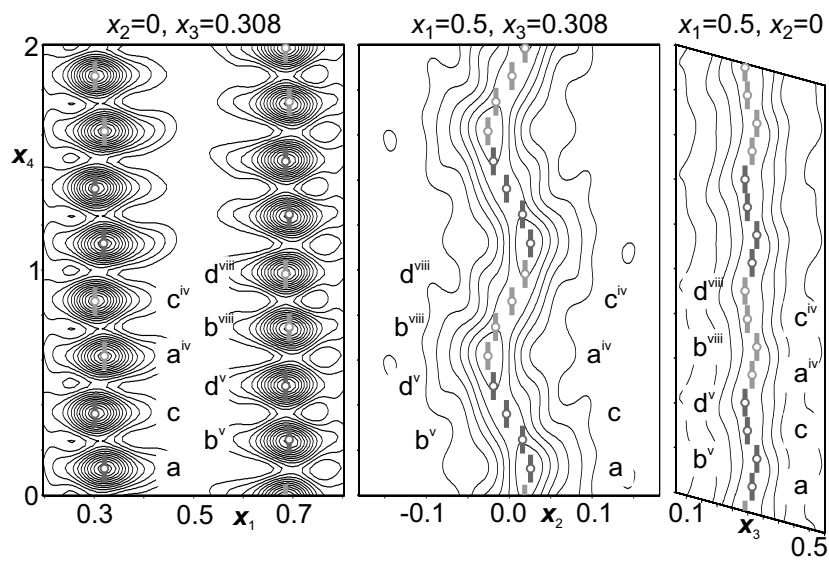


Figure A.6: Fourier maps along x_4 for atom C1, C1^v (dark grey) and C1^{iv} and C1^{viii} (light grey). Symmetry code: (iv) $x_1, -x_2, x_3, x_4 + \frac{1}{2}$, (v) $x_1 + 1, x_2, x_3, x_4$, (viii) $x_1 + 1, -x_2, x_3, x_4 + \frac{1}{2}$. Positions of the relevant t -values are shown by open circles. The step of the contour line is $5 \text{ e}/\text{\AA}^3$. The width of the maps are 4, 4 and 2 \AA

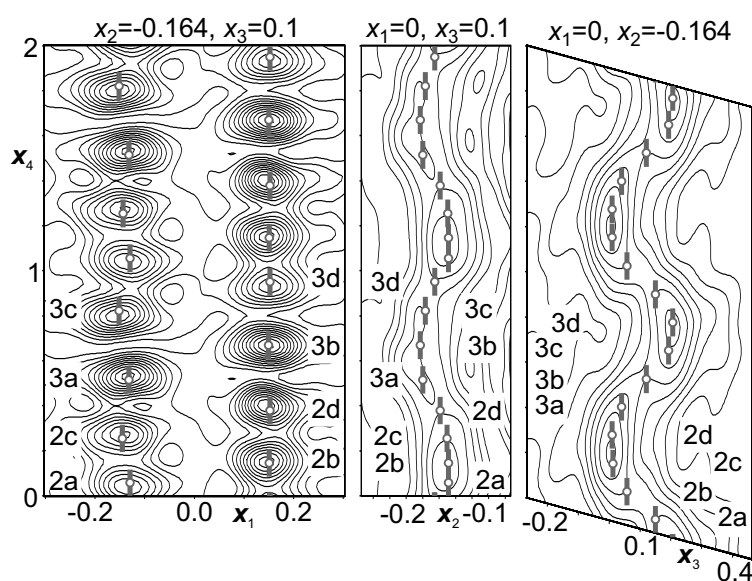


Figure A.7: Fourier maps along x_4 for atom C2 and C3. Positions of the relevant t -values are shown by open circles. The step of the contour line is $0.25 \text{ e}/\text{\AA}^3$. The width of the maps are 4, 2 and 3 \AA

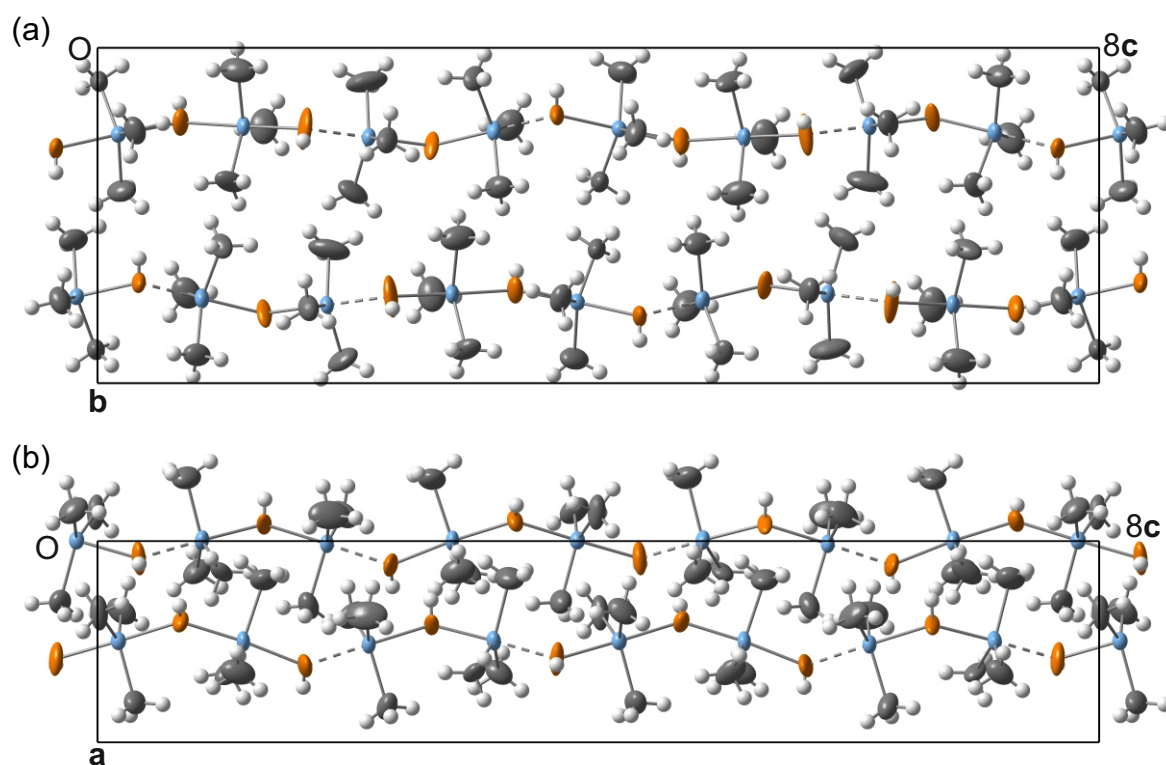


Figure A.8: Packing of the chains each containing eight formula units of $(\text{CH}_3)_3\text{SnOH}$ in the 8-fold supercell along directions (a) $[100]$ and (c) $[0-10]$ with temperature ellipsoids cut at 50 percent probability level. Twist of the chains are visible along the direction $[100]$ while direction $[0-10]$ shows a zigzag arrangement of the formula units. Intra-chain weak forces and inter-chain interactions are not shown.

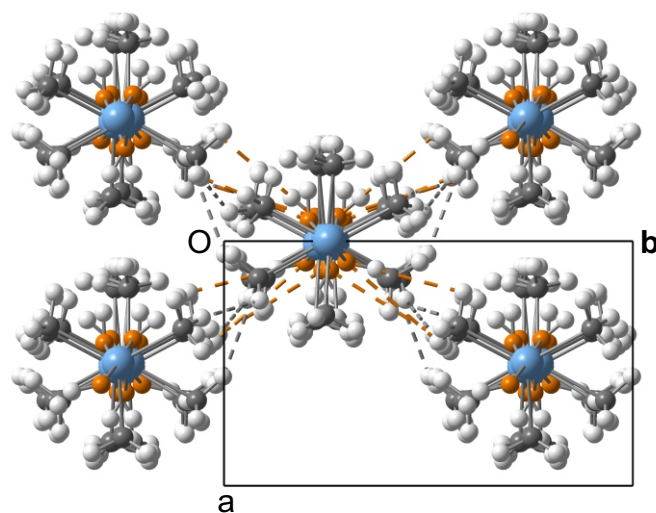


Figure A.9: Crystal packing scheme of the eight-fold superstructure showing inter-strand C–H...O interactions (dashed orange) and inter-strand C–H...H–C interactions (dashed grey). Viewing direction along **c**.

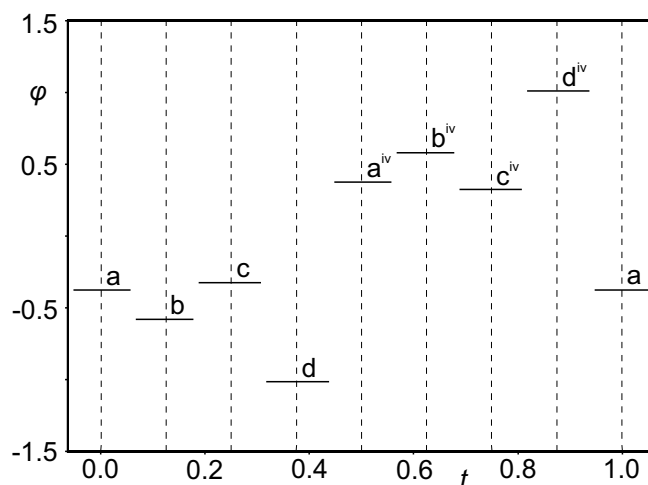


Figure A.10: t -plot of the torsion angles describing the distortion of the Sn atoms out of the planes described by C1, C2, C3 atoms. $a = C1a, C2a, C3a, Sn1a$; $b = C1b, C2b, C3b, Sn1b$; $c = C1c, C2c, C3c, Sn1c$ and $d = C1d, C2d, C3d, Sn1d$. The symmetry operation: (iv) $x_1, -x_2, x_3, t + \frac{1}{2}$. Vertical dashed lines represent the torsion angles in the eight-fold supercell.

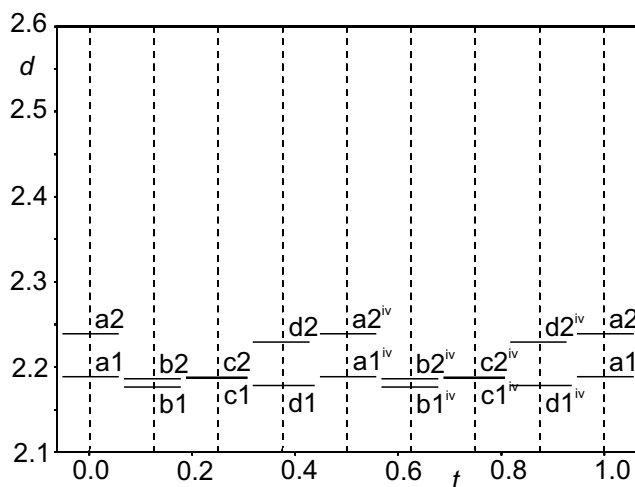


Figure A.11: t -plot of interatomic distances d (Å) between the Sn and O atoms within the chain. a_1 =Sn1a–O1a, a_2 =Sn1a–O1d, b_1 =Sn1b–O1b, b_2 =Sn1b–O1a, c_1 =Sn1c–O1c, c_2 =Sn1c–O1b, d_1 =Sn1d–O1d, d_2 =Sn1d–O1c. The symmetry operation: (iv) $x_1, -x_2, x_3, t + \frac{1}{2}$. Vertical dashed lines represent the distances in the eight-fold supercell.

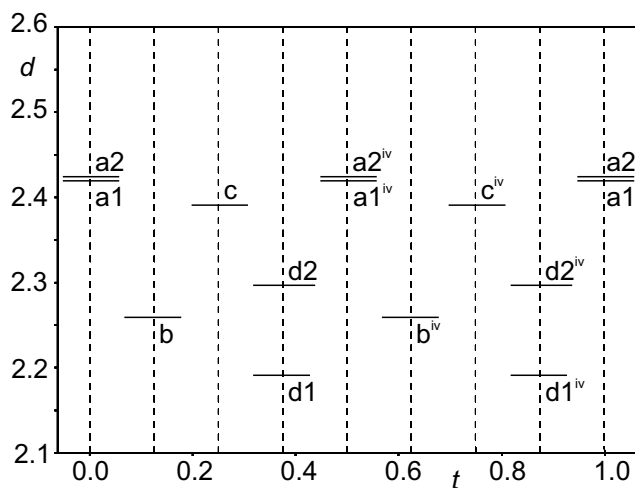


Figure A.12: t -plot of interatomic distances d (Å) between hydrogen atoms of methyl groups and hydrogen atoms of hydroxy groups and hydrogen atoms of adjacent methyl groups within a chain. a_1 =H1o1a–H3c2b, a_2 =H1o1a–H3c1a; b =H1o1b–H2c2c; c =H1o1c–H2c3c; d_1 =H2c1d–H3c2c, d_2 =H1o1d–H3c1d. The symmetry operation: (iv) $x_1, -x_2, x_3, t + \frac{1}{2}$. Vertical dashed lines represent the distances in the eight-fold supercell.

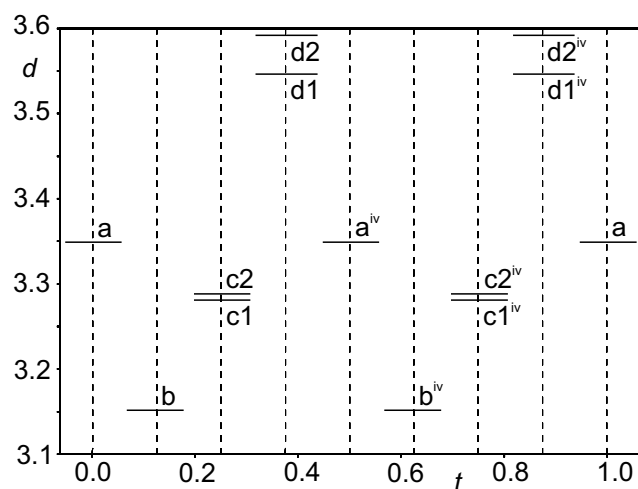


Figure A.13: t -plot of interatomic distances d (Å) between the hydrogen atoms of methyl groups and oxygen atoms of neighbouring chain involved in C-H...O bonds. $a=H3c3a-O1a$; $b=H2c3b-O1d$; $c1=H1c3c-O1c$, $c2=H3c3c-O1c$; $d1=H1c3d-O1b$, $d2=H3c3d-O1b$. The symmetry operation: (iv) $x_1, -x_2, x_3, t+\frac{1}{2}$. Vertical dashed lines represent the distances in the eight-fold supercell.

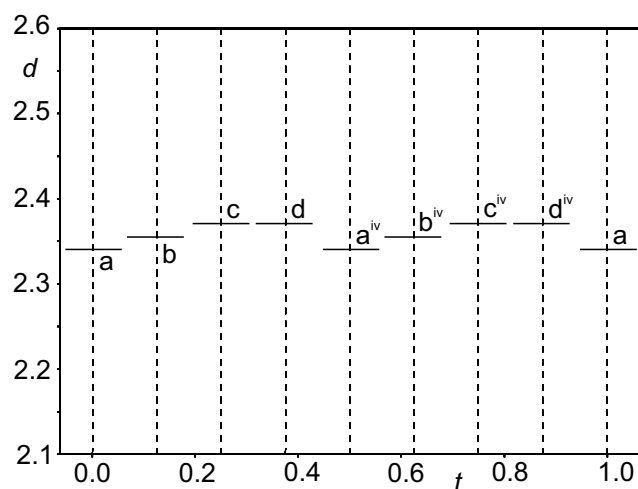


Figure A.14: t -plot of interatomic distances d (Å) between the hydrogen atoms of methyl groups between different chains. $a=H3c3a-H2c3b$; $b=H3c3b-H2c3d$; $c=H2c2c-H3c3d$; $d=H3c3d-H2c2c$. The symmetry operation: (iv) $x_1, -x_2, x_3, t+\frac{1}{2}$. Vertical dashed lines represent the distances in the eight-fold supercell.

Table A.1: Statistical parameters (R_F^{obs} and $wR_{F^2}^{\text{all}}$) of incommensurate (inc) and commensurate refinements of the model with different values of the phase t_0 . Number of reflections (obs/all) used in the refinements: (m=0) = 2020/2539, (m=±1) = 2934/4766, (m=±2) = 1877/5146, (m=±3) = 1159/4779, (m=-4) = 659/2570. Number of parameters used for refinements = 193.

	inc	$t_0 = 0$	$t_0 = \frac{1}{32}$	$t_0 = \frac{1}{16}$
Supercell space group	–	$P2_1cn$	Pc	$P2_1cn$
R_F^{obs} (all)	0.0576	0.0451	0.0453	0.1434
$wR_{F^2}^{\text{all}}$ (all)	0.0828	0.0607	0.0607	0.2769
$R_F^{\text{obs}}(m = 0)$	0.0408	0.0292	0.0295	0.0731
$wR_{F^2}^{\text{all}}(m = 0)$	0.0469	0.0383	0.0385	0.0988
$R_F^{\text{obs}}(m = \pm 1)$	0.0518	0.0482	0.0482	0.1235
$wR_{F^2}^{\text{all}}(m = \pm 1)$	0.0529	0.0471	0.0471	0.1237
$R_F^{\text{obs}}(m = \pm 2)$	0.1016	0.0902	0.0897	0.2001
$wR_{F^2}^{\text{all}}(m = \pm 2)$	0.1151	0.1030	0.1032	0.2068
$R_F^{\text{obs}}(m = \pm 3)$	0.1248	0.1134	0.1143	0.2861
$wR_{F^2}^{\text{all}}(m = \pm 3)$	0.1672	0.1517	0.1521	0.3962
$R_F^{\text{obs}}(m = -4)$	0.1563	0.0656	0.0662	0.9741
$wR_{F^2}^{\text{all}}(m = -4)$	0.2070	0.0806	0.0799	0.9627
$\Delta\rho_{\text{min}}$ (e/Å ³)	-3.11	-1.97	-1.88	-0.58
$\Delta\rho_{\text{max}}$ (e/Å ³)	1.44	1.74	1.66	0.60

Table A.2: Interatomic distances (\AA), torsion angles (deg) and angles (deg) calculated from the superstructure model derived from the superspace model ($t_0 = 0$) describing the distortion of trigonal bipyramidal co-ordination polyhedron of the tin atom. *Symmetry code* : $(iv) x, -y, z + \frac{1}{2}$.

Sn1a–O1a	2.24	O1d–Sn1a–O1a	178.8
Sn1a–O1d	2.19	O1a–Sn1a–C1a	88.6
Sn1a–C1a	2.12	O1a–Sn1a–C2a	90.0
Sn1a–C2a	2.06	O1a–Sn1a–C3a	91.0
Sn1a–C3a	2.11	O1d–Sn1a–C1a	90.7
		O1d–Sn1a–C2a	90.9
C1a–C2a–C3a–Sn1a	-0.3	O1d–Sn1a–C3a	89.5
C2a–C3a–C1a–Sn1a	-0.3	C1a–Sn1a–C2a	119.5
C3a–C1a–C2a–Sn1a	-0.3	C1a–Sn1a–C3a	117.7
		C2a–Sn1a–C3a	122.8
Sn1b–O1b	2.18	O1a ^{iv} –Sn1b–O1b	175.5
Sn1b–O1a ^{iv}	2.19	O1b–Sn1b–C1b	91.3
Sn1b–C1b	2.13	O1b–Sn1b–C2b	89.4
Sn1b–C2b	2.13	O1b–Sn1b–C3b	90.4
Sn1b–C3b	2.11	O1a ^{iv} –Sn1b–C1b	93.0
		O1a ^{iv} –Sn1b–C2b	89.4
C1b–C2b–C3b–Sn1b	-0.7	O1a ^{iv} –Sn1b–C3b	86.5
C2b–C3b–C1b–Sn1b	-0.7	C1b–Sn1b–C2b	120.9
C3b–C1b–C2b–Sn1b	-0.7	C1b–Sn1b–C3b	118.8
		C2b–Sn1b–C3b	120.2
Sn1c–O1c	2.19	O1b–Sn1c–O1c	177.9
Sn1c–O1b	2.19	O1c–Sn1c–C1c	89.9
Sn1c–C1c	2.09	O1c–Sn1c–C2c	90.5
Sn1c–C2c	2.08	O1c–Sn1c–C3c	89.2
Sn1c–C3c	2.11	O1b–Sn1c–C1c	91.4
		O1b–Sn1c–C2c	90.4
C1c–C2c–C3c–Sn1c	0.3	O1b–Sn1c–C3c	88.8
C2c–C3c–C1c–Sn1c	0.3	C1c–Sn1c–C2c	117.4
C3c–C1c–C2c–Sn1c	0.3	C1c–Sn1c–C3c	119.2
		C2c–Sn1c–C3c	123.4
Sn1d–O1d	2.18	O1c–Sn1d–O1d	178.3
Sn1d–O1c	2.23	O1d–Sn1d–C1d	91.0
Sn1d–C1d	2.12	O1d–Sn1d–C2d	90.9
Sn1d–C2d	2.12	O1d–Sn1d–C3d	89.6
Sn1d–C3d	2.14	O1c–Sn1d–C1d	90.7
		O1c–Sn1d–C2d	87.9
C1d–C2d–C3d–Sn1d	-1.0	O1c–Sn1d–C3d	90.0
C2d–C3d–C1d–Sn1d	-1.0	C1d–Sn1d–C2b	118.6
C3d–C1d–C2d–Sn1d	-1.0	C1d–Sn1d–C3b	121.7
		C2d–Sn1d–C3b	119.6

Table A.3: Deviation of metal–oxygen co-ordination distances (Å) at $T = 220$ K and $T = 100$ K of trimethyltin hydroxide and published literature of other similar compounds.

Compound	Space group	Atom groups	distance
Trimethyltin hydroxide (present structure)	$P2_1cn$	Sn–O	2.18/2.24
Trimethyltin hydroxide ($T = 100$ K) (Dey et al., 2016b)	$P2_12_12_1$	Sn–O	2.20/2.22
Trimethyltin fluoride (Clark et al., 1964)	$P2_1cn$	Sn–F	2.16/2.16
Trimethyltin Cyanide (Schlemper and Britton, 1966)	$Cmcm$	Sn–C(or N)	2.47/2.51
Trimethyltin methoxide (Domingos and Sheldrick, 1974)	$P2_12_12_1$	Sn–O	2.20/2.26
Trimethyltin methylsulphinate (Sheldrick and Taylor, 1977)	$C222_1$	Sn–O	2.21/2.27
Hydroxotriphenyltin(IV) (Glidewell and Liles, 1978)	$P2_12_12_1$	Sn–O	2.20/2.26
Hydroxotriphenyllead(IV) (Glidewell and Liles, 1978)	$P2_12_12_1$	Sn–O	2.37/2.44
Triethyltin hydroxide (Deacon et al., 1993)	$Pnma$	Sn–O	2.20/2.26

Appendix B

Supplementary material:
 Λ -Cobalt (III) sepulchrate
trinitrate

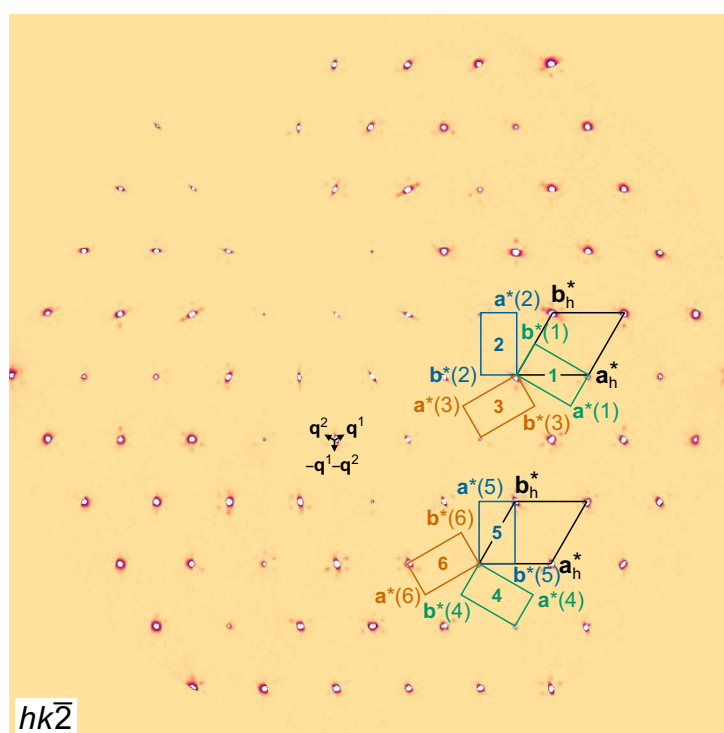


Figure B.1: Reconstruction of the reciprocal lattice plane $hk\bar{2}$ with the hexagonal unit cell and the ones for the monoclinic six-fold twinning, exhibiting strong main and weak satellite reflections at $T = 95$ K.

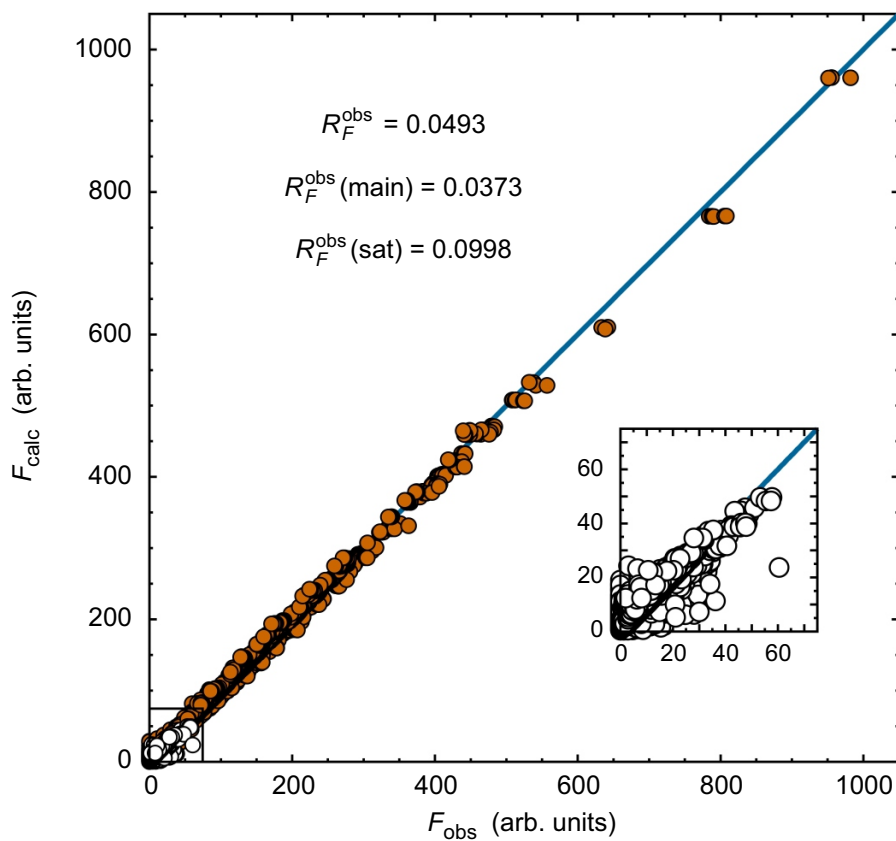


Figure B.2: Plot of F_{obs} vs. F_{calc} of the 8468 main (orange circles) and 50975 satellite reflections (white circles) applied in the refinement of the final structural model at $T = 95$ K. In the inset only the satellite reflections are shown.

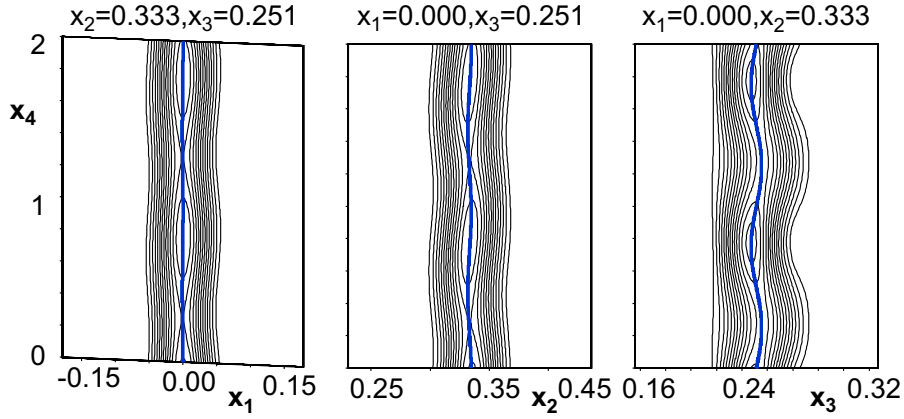


Figure B.3: Sections (x_1, x_4) , (x_2, x_4) and (x_3, x_4) centered at the position of the cobalt atom of the Fourier map of $\text{Co}(\text{sep})(\text{NO}_3)_3$ at $T = 95$ K. They reveal a smooth modulation described by harmonic waves of first order. Contour lines of equal density are at intervals of $1.0 \text{ e}/\text{\AA}^3$. The thick blue curve represents the refined modulation function. The width of each panel is 3 \AA .

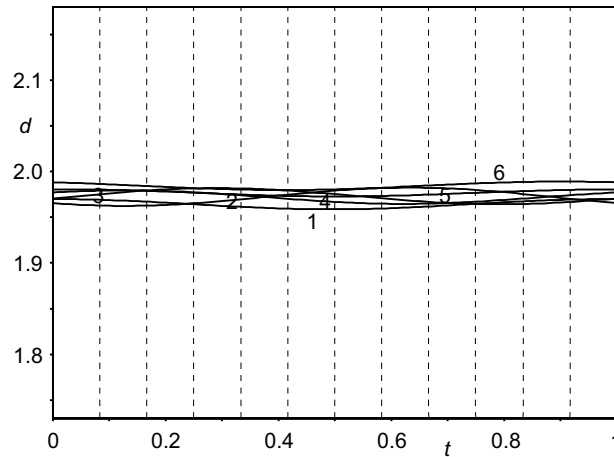


Figure B.4: t -Plot of interatomic distances d (\AA) between the cobalt atom and the six coordinating nitrogen atoms N_{lig} at $T = 95$ K. Vertical, dashed lines indicate t values corresponding to the distances in the 12-fold supercell.

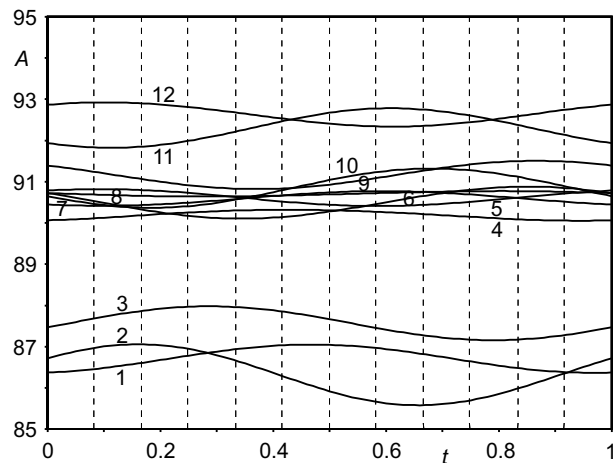


Figure B.5: t -Plot of angles $N_{lig}-Co-N_{lig}$ (deg), involving the six coordinating nitrogen atoms N_{lig} at $T = 95$ K. The variation with t of individual angles is smaller than the average distortion of the CoN_6 octahedron. 1=N21-Co1-N26, 2=N22-Co1-N25, 3=N23-Co1-N24, 4=N22-Co1-N23, 5=N21-Co1-N24, 6=N22-Co1-N26, 7=N25-Co1-N26, 8=N23-Co1-N25, 9=N24-Co1-N26, 10=N22-Co1-N24, 11=N21-Co1-N25, and 12=N21-Co1-N23.

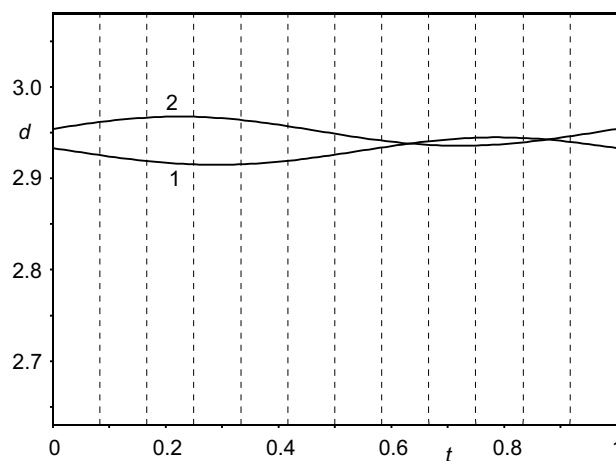


Figure B.6: t -Plot of interatomic distances d (Å) between the cobalt atom and the two capping nitrogen atoms N51 and N52 at $T = 95$ K.

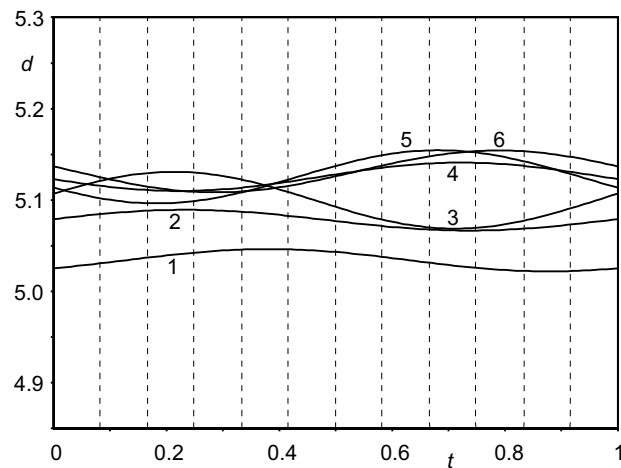


Figure B.7: t -Plot of interatomic distances d (\AA) between the cobalt atom and the nitrogen atoms of nitrate groups A and B at $T = 95$ K. One cobalt atom is coordinated by three nitrate groups A (3, 5 and 6) and three nitrate groups B (1, 2 and 4).

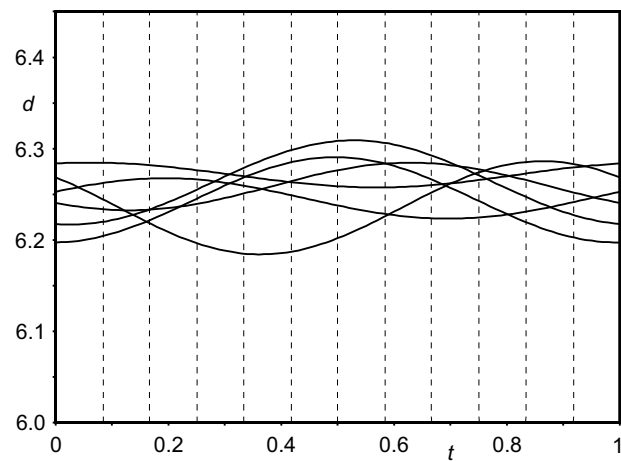


Figure B.8: t -Plot of interatomic distances d (\AA) between the Co atom and the nitrogen atom of nitrate group C at $T = 95$ K. One cobalt atom is coordinated by six nitrate groups C.

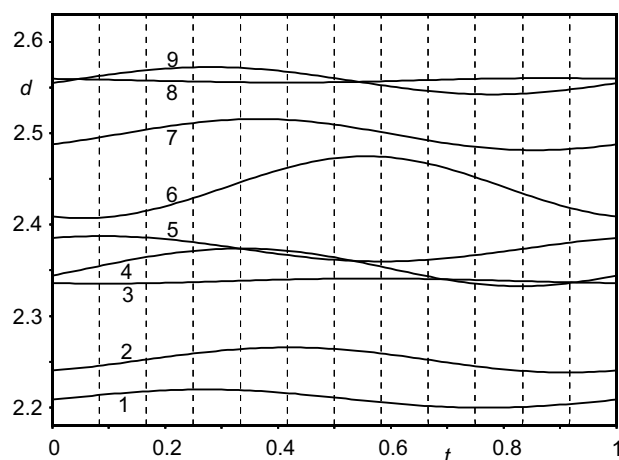


Figure B.9: t -Plot of interatomic distances d (Å) between the O atom of nitrate group B and hydrogen atoms of the sepulchrate cage at $T = 95$ K. Vertical, dashed lines indicate t values corresponding to the distances in the 12-fold supercell. Six N-H \cdots O contacts (3, 5–9) and three C-H \cdots O contacts (1, 2 and 4) are shown (compare Fig. 1): 1=O71/3b \cdots H2c36, 2=O71/1b \cdots H2c34, 3=O71/1b \cdots H1n22, 4=O71b \cdots H2c32, 5=O71/3b \cdots H1n22, 6=O71b \cdots H1n26, 7=O71b \cdots H1n24, 8=O71/1b \cdots H1n26, and 9=O71/3b \cdots H1n24. A similar plot for nitrate group A is given in Fig. 9 of the article.

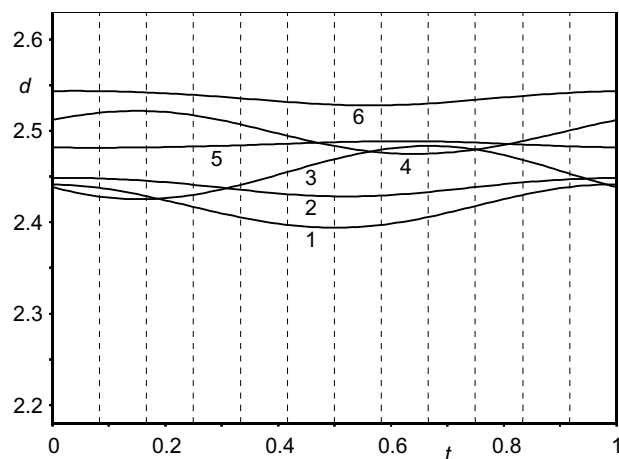


Figure B.10: t -Plot of interatomic distances between the hydrogen atoms of carbon atoms C3 on neighboring molecules at $T = 95$ K.

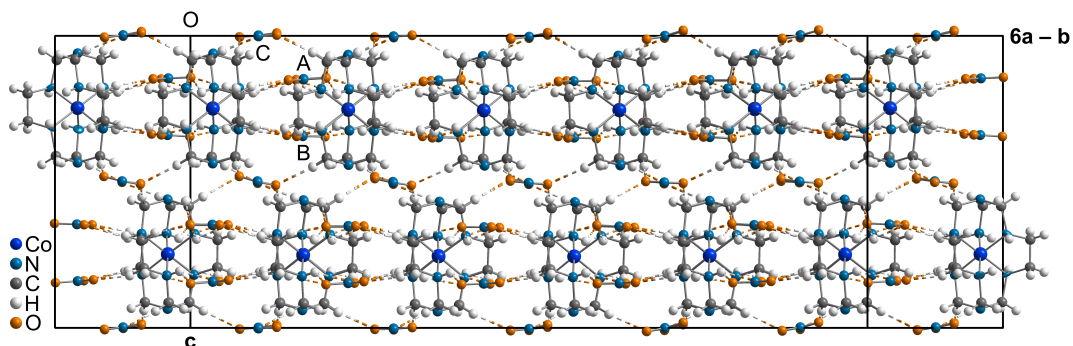


Figure B.11: View along $(6\ 1\ 0)$ of the supercell of Λ -cobalt(III) sepulchrate trinitrate at $T = 95$ K. N-H \cdots O and C-H \cdots O hydrogen bonds are indicated by dashed lines.

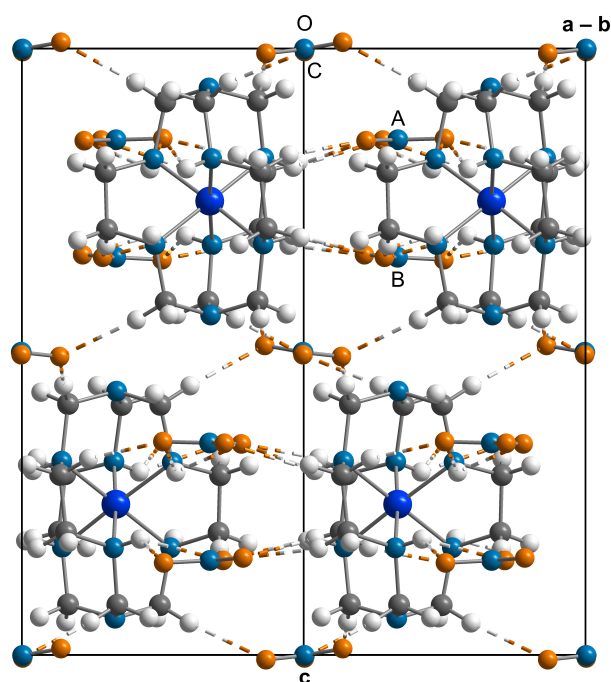


Figure B.12: Projection of the crystal structure along $(1\ 1\ 0)$ of the basic structure at $T = 95$ K. Dashed lines indicate N-H \cdots O and C-H \cdots O hydrogen bonds of nitrate groups A and B, as well as C-H \cdots O hydrogen bonds involving nitrate group C.

Table B.1: Amplitudes of the atomic modulation functions along the three basis vectors at $T = 95$ K. The largest displacements are along **c**; the smallest displacements are along **a**. Magnitudes of displacements are 0.149 Å along **c** for O9 of nitrate group C and up to 0.100 Å for the other atoms; 0.090 Å along **b** for O9 and up to 0.055 Å for the other atoms; and 0.047 Å along **a** for O9 and up to 0.030 Å for the other atoms.

Atom	along a (Å)	along b (Å)	along c (Å)
Co(sep) cage			
Co1	0.0039	0.0209	0.0652
N21	0.0075	0.0314	0.0708
N22	0.0075	0.0368	0.0770
N23	0.0128	0.0332	0.0454
N24	0.0081	0.0300	0.0533
N25	0.0094	0.0288	0.0844
N26	0.0122	0.0330	0.0960
C31	0.0062	0.0226	0.0996
C32	0.0114	0.0381	0.0824
C33	0.0197	0.0277	0.0365
C34	0.0049	0.0259	0.0366
C35	0.0074	0.0185	0.0914
C36	0.0111	0.0266	0.0934
C41	0.0211	0.0607	0.0778
C42	0.0163	0.0500	0.0764
C43	0.0301	0.0409	0.0607
C44	0.0185	0.0538	0.0603
C45	0.0234	0.0396	0.0963
C46	0.0108	0.0540	0.1004
N51	0.0290	0.0545	0.0800
N52	0.0155	0.0548	0.0810
nitrate group A			
N6a	0.0230	0.0408	0.0791
O71a	0.0177	0.0482	0.0658
O71/1a	0.0190	0.0330	0.1056
O71/3a	0.0344	0.0424	0.0845
nitrate group B			
N6b	0.0127	0.0297	0.0709
O71b	0.0147	0.0294	0.0628
O71/1b	0.0156	0.0315	0.0767
O71/3b	0.0077	0.0294	0.0901
nitrate group C			
N8a	0.0283	0.0722	0.0502
O91a	0.0470	0.0897	0.1487
O91/1a	0.0409	0.0634	0.0583
O91/3a	0.0037	0.0645	0.0716

Bibliography

- Anderson, K. M., Goeta, A. E. and Steed, J. W. (2008). Supramolecular synthon frustration leads to crystal structure with $Z' > 1$, *Cryst. Growth Des.* **8**: 2517–2524. [54](#)
- Anderson, K. M., Tallentire, S. E., Probert, M. R., Goeta, A. E., Mendis, B. G. and Steed, J. W. (2011). Trimethyltin hydroxide: A crystallographic and high Z' curiosity, *Cryst. Growth Des.* **11**: 820–826. [7](#), [38](#), [39](#), [40](#), [41](#), [44](#), [52](#), [53](#), [54](#), [55](#), [56](#), [62](#), [63](#)
- Arnold, H. (2006). 5.1. Transformations of the coordinate system (unit-cell transformations), in T. Hahn (ed.), *International Tables for Crystallography Vol. A*, Wiley, UK, pp. 78–85. [75](#), [76](#)
- Bacchi, A., Ferranti, F. and Pelizzi, G. (1993). Structures of two cobalt(III) sepulchrate complexes, *Acta Crystallogr.* **C49**: 1163–1169. [83](#)
- Bacchi, A., Ferranti, F. and Pelizzi, G. (1996). Conformation and packing of cobalt(III) sepulchrate dihydrogentriphosphate hexahydrate, *Acta Crystallogr.* **C52**: 1624–1627. [83](#)
- Bastiansen, O. (1949). The molecular structure of biphenyl and some of its derivatives, *Acta Chem. Scand.* **3**: 408–414. [18](#)
- Baudour, J. L. and Sanquer, M. (1983). Structural phase transition in polyphenyls. VIII. The modulated structure of biphenyl ($T \simeq 20$ K) from neutron diffraction data, *Acta Crystallogr.* **B39**: 75–84. [19](#), [20](#)
- Bernhardt, P. V., Chen, K. I. and Sharpe, P. C. (2006). Transition metal complexes as mediator-titrants in protein redox potentiometry, *J. Biol. Inorg. Chem.* **11**: 930–936. [70](#)

- Brandenburg, K. and Putz, H. (2014). DIAMOND - *Crystal and molecular structure visualization*, Crystal Impact GbR, Kreuzherrenstr. 102, 53227 Bonn, Germany. [39](#), [55](#), [64](#), [66](#), [67](#)
- Brock, C. P. (1996). Investigations of the systematics of crystal packing using the CAMBRIDGE STRUCTURAL DATABASE, *J. Res. Natl. Inst. Stand. Technol.* **101**: 321–325. [54](#)
- Brock, C. P. and Dunitz, J. D. (1994). Towards a grammar of crystal packing, *Chem. Mater.* **6**: 1118–1127. [54](#)
- Bruker (2008). SADABS 2008/1, Bruker AXS Inc., Madison, Wisconsin, USA. [41](#), [59](#), [74](#), [93](#)
- Bussien Gaillard, V., Paciorek, W., Schenk, K. and Chapuis, G. (1996). Hexamethylenetetramine suberate, a strongly anharmonic modulated structure, *Acta Crystallogr.* **B52**: 1036–1047. [24](#), [25](#), [26](#)
- Cailleau, H., Moussa, F. and Mons, J. (1979). Incommensurate phases in biphenyl, *Solid State Comm.* **31**: 521–524. [19](#), [38](#)
- Chapuis, G. (1978). Study of the first-order phase transition of $(\text{C}_3\text{H}_7\text{NH}_3)_2\text{CdCl}_4$ at 183 K by X-ray diffraction of the two phases, *Acta Crystallogr.* **B34**: 1506–1512. [27](#)
- Chapuis, G. (1996). Modulated structures induced by phase transformations, *Crystallogr. Rev.* **5:2**: 109–128. [27](#), [28](#), [29](#)
- Clark, H. C., O'Brien, R. J. and Trotter, J. (1964). The structure of trimethyltin fluoride, *J. Chem. Soc.* pp. 2332–2336. [63](#), [129](#)
- Creaser, I. I., Geue, R. J., Harrowfield, J. M., Herlt, A. J., Sargeson, A. M., Snow, M. R. and Springborg, J. (1982). Synthesis and reactivity of Aza-capped encapsulated Co(III) ions, *J. Am. Chem. Soc.* **104**: 6016–6025. [72](#)
- Dannenberg, J. J., Haskamp, L. and Masunov, A. (1999). Are hydrogen bonds covalent or electrostatic? a molecular orbital comparison of molecules in electric fields and h-bonding environments, *J. Phys. Chem.* **A103**: 7083–7086. [65](#)

- de Wolff, P. M. (1974). The pseudo-symmetry of modulated crystal structures, *Acta Crystallogr.* **A30**: 777–785. [6](#), [12](#), [13](#)
- Deacon, G. B., Lawrenz, E., Nelson, K. T. and Tiekink, E. R. T. (1993). Crystal structure of polymeric triethyltin hydroxide, *Main Group Met. Chem.* **16**: 265–269. [6](#), [39](#), [50](#), [63](#), [129](#)
- Depmeier, W. (1981). The modulated structure of the layered perovskite γ -bis(n-propylammonium) tetrachloromanganate(II): Refinement of the average structure, the possible superspace group and a model for the modulated structure, *Acta Crystallogr.* **B37**: 330–339. [27](#)
- Depmeier, W., Felsche, J. and Wildermut, G. (1977). Phases and phase transitions of compounds $(C_nH_{2n+1}NH_3)_2MnCl_4$, with $n = 1, 2, 3$, *J. Solid State Chem.* **21**: 57–65. [28](#)
- Desiraju, G. R. (1991). The C–H \cdots O hydrogen bond in crystals: What is it?, *Acc. Chem. Res.* **24**: 290–296. [85](#)
- Desiraju, G. R. (1995). Supramolecular synthons in crystal engineering - A new organic synthesis, *Angew. Chem. Int. Ed. Engl.* **34**: 2311–2327. [54](#)
- Desiraju, G. R. (1996). The C–H \cdots O hydrogen bond: Structural implications and supramolecular design, *Acc. Chem. Res.* **29**: 441–449. [50](#)
- Desiraju, G. R. (2007). On the presence of multiple molecules in the crystal asymmetric unit ($Z' \neq 1$), *CrystEnggComm* **9**: 91–92. [54](#)
- Desiraju, G. R., Kashino, S., Coombs, M. M. and Glusker, J. P. (1993). C–H \cdots O packing motifs in some cyclopenta[a]phenanthrenes, *Acta Crystallogr. B* **49**: 880–892. [85](#)
- Desiraju, G. R. and Steiner, T. (2001). *The weak hydrogen bond in structural chemistry and biology*, Oxford University Press, Oxford. [65](#), [85](#), [103](#)
- Dey, S., Schönleber, A., Mondal, S., Prathapa, S. J., van Smaalen, S. and Larsen, F. K. (2016a). The $Z' = 12$ superstructure of Λ -cobalt(III) sepulchrate trinitrate governed by C–H \cdots O hydrogen bonds, *Acta Crystallogr.* **B72**: 372–380. [54](#)

- Dey, S., Schönleber, A., Mondal, S. and van Smaalen, S. (2016b). Superspace description of trimethyltin hydroxide at $T = 100$ K, *Z. Kristallogr.* **231**: 427–434. [62](#), [63](#), [68](#), [129](#)
- Domingos, A. M. and Sheldrick, G. M. (1974). Trimethyltin methoxide, *Acta Crystallogr.* **B30**: 519–521. [39](#), [63](#), [129](#)
- Doudin, B. and Chapuis, G. (1988). Study of the modulated phase of $(\text{C}_3\text{H}_7\text{NH}_3)_2\text{CdCl}_4$ by single-crystal X-ray diffraction, *Acta Crystallogr.* **B44**: 495–502. [27](#)
- Doudin, B. and Chapuis, G. (1990a). Structure analysis of the high-temperature phases of $[\text{NH}_3(\text{C}_3\text{H}_7)]_2\text{CuCl}_4$. I. The commensurate phases, *Acta Crystallogr.* **B46**: 175–180. [28](#)
- Doudin, B. and Chapuis, G. (1990b). Structure analysis of the high-temperature phases of $[\text{NH}_3(\text{C}_3\text{H}_7)]_2\text{CuCl}_4$. II. The modulated phase, *Acta Crystallogr.* **B46**: 180–186. [28](#)
- Doudin, B. and Heine, V. (1990). The origin of the γ incommensurate structure in n-propylammonium tetrachlorometallates, *J. Phys.: Condens. Matter* **2**: 3237–3246. [28](#)
- Dubicki, L., Ferguson, J., Geue, R. J. and Sargeson, A. M. (1980). Circular dichroism of cobalt(III) complexes: Dependence on the outer sphere configuration, *Chem. Phys. Lett.* **74**: 393–397. [70](#)
- Dubicki, L., Ferguson, J. and Williamson, B. (1984). Circular dichroism of cobalt(III) complexes. 2. Phase changes in $\Lambda\text{-Co}(\text{sep})(\text{NO}_3)_3$, *J. Phys. Chem.* **88**: 4254–4258. [8](#), [70](#), [71](#)
- Eaton, V. J. and Steele, D. (1973). Dihedral angle of biphenyl in solution and the molecular force field, *J. Chem. Soc., Faraday Trans. 2* **69**: 1601–1608. [18](#)
- Flack, H. D. (1983). On enantiomorph-polarity estimation, *Acta Crystallogr.* **A39**: 876–881. [57](#), [60](#), [117](#)
- Gahan, L. R. and Harrowfield, J. M. (2015). Sepulchrate: Four decades on, *Polyhedron* **94**: 1–51. [70](#), [83](#)

- Garcia, R., Philp, E. F., Slawin, A. M. Z., Wright, P. A. and Cox, P. A. (2001). 05-O-03-On the role of azamacrocycles and metal cations in the syntheses of met-alloaluminophosphates STA-6, -7 and -8, *in* A. Galarneau, F. Fajula, D. Renzo and J. Viedrine (eds), *Stud. Surf. Sci. Catal.*, Vol. 135, p. 157. [70](#)
- Giacovazzo, C., Monaco, H., Artioli, G., Viterbo, D., Ferraris, G., Gilli, G., Zannotti, G. and Catti, M. (2002). *Fundamentals of Crystallography*, 2 edn, Oxford University Press, Oxford. [30](#)
- Gilli, G. and Gilli, P. (2009). *An introduction to hydrogen bonding*, IUCr/Oxford University Press. [103](#)
- Glidewell, C. and Liles, D. C. (1978). The crystal and molecular structures of hydroxotriphenyltin(IV) and hydroxotriphenyllead(IV), *Acta Crystallogr.* **B34**: 129–134. [39](#), [47](#), [63](#), [129](#)
- Görbitz, C. H., Törnroos, K. W. and Day, G. M. (2012). Single-crystal investigation of L-tryptophan with $Z' = 16$, *Acta Crystallogr.* **B68**: 549–557. [80](#)
- Gotoh, K., Asaji, T. and Ishida, H. (2007). Hydrogen bonding in two solid phases of phenazine-chloranilic acid (1/1) determined at 170 and 93 K, *Acta Crystallogr.* **C63**: 17–20. [31](#)
- Groom, C. R., Bruno, I. J., Lightfoot, M. P. and Ward, S. C. (2016). THE CAMBRIDGE STRUCTURAL DATABASE, *Acta Crystallogr.* **B72**: 171–179. [40](#)
- Gu, Y., Kar, T. and Scheiner, S. (1999). Fundamental properties of the CH \cdots O interaction: Is it a true hydrogen bond?, *J. Am. Chem. Soc.* **121**: 9411–9422. [50](#)
- Hahn, T. and Klapper, H. (2006). 3.3 Twinning of crystals, *in* A. Authier (ed.), *International Tables for Crystallography*, Vol. D, Springer, pp. 393–448. [30](#)
- Hao, X., Siegler, M. A., Parkin, S. and Brock, C. P. (2005). [M(H₂O)₂(15-crown-5)](NO₃)₂: A system rich in polymorphic and modulated phases, *Cryst. Growth Des.* **5**: 2225–2232. [54](#)
- Hargreaves, A. and Hasan Rizvi, S. (1962). The crystal and molecular structure of biphenyl, *Acta Crystallogr.* **15**: 365–373. [19](#), [38](#)

- Harris, P., Larsen, F. K., Lebeck, B. and Achiwa, N. (1994). Crystal structure of the commensurately modulated ζ phase of PAMC, *Acta Crystallogr.* **B50**: 676–684. [54](#)
- Hathaway, B. J. and Webster, D. E. (1963). Trimethyltin tetrafluoroborate: Infrared evidence of covalently bonded tetrafluoroborate anion, *P Chem Soc London* p. 14. [39](#)
- Hondow, N., Harowfield, J., Koutsantonis, G., Nealon, G. and Saunders, M. (2012). Metallosurfactants in the preparation of mesoporous silicas, *Microporous Mesoporous Mater.* **151**: 264–270. [70](#)
- Horiuchi, S., Ishii, F., Kumai, R., Okimoto, Y., Tachibana, H., Nagaosa, N. and Tokura, Y. (2005). Ferroelectricity near room temperature in co-crystals of non-polar organic molecules, *Nature Mater* **4**: 163–166. [31](#)
- Horiuchi, S., Kumai, R. and Tokura, Y. (2009). Proton-displacive ferroelectricity in neutral cocrystals of anilic acids with phenazine, *J. Mater. Chem.* **19**: 4421–4434. [31](#)
- Jagodzinski, H. and Frey, F. (2006). 4.2. Disorder diffuse scattering of X-rays and neutrons, in U. Shmueli (ed.), *International Tables for Crystallography*, Vol. B, Springer, pp. 407–442. [34](#)
- Jahn, I. R., Knorr, K. and Ihringer, J. (1989). The Jahn-Teller effect and orientational order in $(C_nH_{2n+1}NH_3)_2CuCl_4$, $n=1, 2, 3$, *J. Phys.: Condens. Matter* **1**: 6005–6017. [28](#)
- Jahn, I. R., Knorr, K. and Ihringer, J. (1994). Competing structural phase sequences in $(C_3H_7NH_3)_2CuCl_4$: Reconstructive phase transitions and the low-temperature incommensurate phase, *J. Phys.: Condens. Matter* **6**: 10839–10853. [29](#)
- James, R. W. and Saunderson, D. H. (1947). Some apparent periodic errors in the crystal lattice of some molecular complexes of 4:4'-dinitrodiphenyl with 4-iodo- and 4-bromodiphenyl, *Proc. Roy. Soc.* **A190**: 518–533. [6](#)
- James, R. W. and Saunderson, D. H. (1948). Periodic errors in the crystal lattices of some molecular complexes of 4:4'-dinitrodiphenyl, *Acta Crystallogr.* **1**: 81–83. [6](#)

- Janssen, T., Chapuis, G. and de Boissieu, M. (2007). *Aperiodic crystals*, Oxford University Press. [12](#), [40](#), [54](#), [72](#)
- Janssen, T., Janner, A., Looijenga-Vos, A. and de Wolff, P. M. (2006). Incommensurate and commensurate modulated structures, in E. Prince (ed.), *International Tables for Crystallography Vol. C*, Wiley, UK, pp. 907–955. [75](#)
- Jeffrey, G. A. (1997). *An introduction to hydrogen bonding*, Oxford University Press. [85](#), [103](#)
- Kasai, N., Yasuda, K. and Okawara, R. (1965). The crystal structure of trimethyltin hydroxide, *J. Organomet. Chem.* **3**: 169–172. [38](#), [39](#), [54](#), [114](#)
- Kind, R. and Muralt, P. (1986). 20. Unique incommensurate-commensurate phase transitions in a layer-structure perovskite, in R. Blinc and A. P. Levanyuk (eds), *Incommensurate phases in dielectrics 2. Materials*, Vol. 14.2, Elsevier Science Publishers B. V., North-Holland Amsterdam, pp. 301–318. [26](#), [27](#)
- Kriegsmann, H., Hoffmann, H. and Pischtschan, S. (1962). Untersuchungen an Zinnverbindungen. II. Schwingungsspektren und chemisches Verhalten von Trimethylzinnhydroxyd und Hexamethyldistannoxan, *Z. Anorg. Allg. Chem.* **315**: 283–290. [6](#), [38](#), [39](#), [54](#)
- Kriegsmann, H. and Pischtschan, S. (1961). Untersuchungen an Zinnverbindungen. I. Schwingungsspektren, Konstitution und Assoziation von Trimethylzinn-derivaten, *Z. Anorg. Allg. Chem.* **308**: 212–225. [39](#)
- Kumai, R., Horiuchi, S., Sagayama, H., Arima, T.-H., Watanabe, M., Noda, Y. and Tokura, Y. (2007). Structural assignment of polarization in hydrogen-bonded supramolecular ferroelectrics, *J. Am. Chem. Soc.* **129**: 12920–12921. [31](#)
- Larsen, F. K., Jørgensen, P., Hazell, R. G., Lebech, B., Thomas, R., Geue, R. J. and Sargeson, A. M. (1988). Phase transitions in Λ -Co(sepulchrates)(NO₃)₃, in J. J. Stezowski, J.-L. Huang and M.-C. Shao (eds), *Molecular structure: Chemical reactivity and biological activity*, IUCr/Oxford University Press, Oxford, pp. 499–504. [8](#), [71](#)
- Li, L., Wölfel, A., Schönleber, A., Mondal, S., Schreurs, A. M. M., Kroon-Batenburg, L. M. J. and van Smaalen, S. (2011). Modulated anharmonic ADPs are intrinsic to

- aperiodic crystals: a case study on incommensurate Rb_2ZnCl_4 , *Acta Crystallogr.* **B67**: 205–217. [78](#)
- Luis, J. and Amorós, M. (1968). *Molecular crystals: Their transforms and diffuse scattering*, John Wiley and Sons. [11](#)
- Munshi, P. and Guru Row, T. N. (2005). Exploring the lower limit in hydrogen Bonds: Analysis of weak C–H···O and C–H···pi interactions in substituted coumarins from charge density analysis, *J. Phys. Chem. A* **109**: 659–672. [85](#)
- Muralt, P., Kind, R., Blinc, R. and Zeks, B. (1982). Incommensurate-reentrant high-symmetry phase transition in a layer-structure perovskite, *Phys. Rev. Lett* **49**: 1019–1022. [27](#)
- Noohinejad, L., Mondal, S., Ali, S. I., Dey, S., van Smaalen, S. and Schönleber, A. (2015). Resonance-stabilized partial proton transfer in hydrogen bonds of incommensurate phenazine-chloranilic acid, *Acta Crystallogr.* **B71**: 228–234. [31](#), [32](#), [54](#)
- Noohinejad, L., Mondal, S., Wölfel, A., Ali, S. I., Schönleber, A. and van Smaalen, S. (2014). Ferroelectricity of phenazine-chloranilic acid at $T = 100$ K, *J. Chem. Crystallogr.* **44**: 387–393. [31](#), [32](#), [38](#), [40](#)
- Okawara, R. and Ohara, M. (1964). The infrared and far infrared spectra of tri-alkyltin formates: Presence of a linear polymer in the solid state and in solution, *J. Organometal. Chem* **1**: 360–365. [39](#)
- Okawara, R. and Yasuda, K. (1964). Occurrence of dimeric trimethyltin hydroxide, *J. Organometal. Chem* **1**: 356–359. [38](#)
- Palatinus, L. (2013). The charge-flipping algorithm in crystallography, *Acta Crystallogr.* **B69**: 1–16. [44](#), [59](#), [114](#)
- Palatinus, L. and Chapuis, G. (2007). SUPERFLIP - A computer program for the solution of crystal structures by charge flipping in arbitrary dimensions, *J. Appl. Crystallogr.* **40**: 786–790. [44](#), [59](#), [76](#), [96](#), [114](#)
- Pan, Y., Brown, D. and Chapuis, G. (2001). Molecular dynamics simulation of incommensurate structures, *Ferroelectrics* **250**: 107–110. [26](#)

- Pan, Y. and Chapuis, G. (2002). Mechanism of the incommensurate phase in hexamethylene-tetramine suberate: A molecular-dynamics study, *Phys. Rev.* **B65**: 1–8. [26](#)
- Pan, Y. and Chapuis, G. (2005). Molecular dynamics investigations of modulated phases in organic materials, *Acta Crystallogr.* **A61**: 19–27. [26](#)
- Parsons, S. (2003). Introduction to twinning, *Acta Crystallogr.* **D59**: 1995–2003. [30](#), [31](#)
- Parsons, S., Pulham, C. and Wood, P. (2004). *CCDC 247854: Experimental crystal structure determination*, CAMBRIDGE CRYSTALLOGRAPHIC DATA Centre, CSD refcode = TMESNH01. [40](#), [41](#), [44](#), [52](#)
- Pérez-Mato, J. M., Chapuis, G., Farkas-Jahnke, M., Senechal, M. L. and Steurer, W. (1992). Ad interim commission on aperiodic crystallography, International Union of Crystallography, report of the executive committee for 1991, *Acta Crystallogr.* **A48**: 922–946. [11](#)
- Petricek, V., Coppens, P. and Becker, P. (1985). Structure analysis of displacively modulated molecular crystals, *Acta Crystallogr.* **A41**: 478–483. [19](#)
- Petricek, V., Dusek, M. and Palatinus, L. (2014). Crystallographic computing system JANA2006: General features, *Z. Kristallogr.* **229**: 345–352. [44](#), [59](#), [76](#), [96](#), [114](#)
- Petricek, V., Eigner, V., Dusek, M. and Cejchan, A. (2016). Discontinuous modulation functions and their application for analysis of modulated structures with the computing system JANA2006, *Z. Kristallogr.* **231**: 301–312. [44](#), [59](#), [115](#)
- Pina, F., Mulazzani, Q. G., Venturi, M., Ciano, M. and Balzani, V. (1985). Photochemistry of Co(sep)³⁺-Oxalatoen pairs: A novel system for dihydrogen evolution from aqueous solutions, *Inorg. Chem.* **24**: 848–851. [70](#)
- Pinheiro, C. B. and Abakumov, A. M. (2015). Superspace crystallography: A key to the chemistry and properties, *IUCrJ* **2**: 137–154. [38](#), [54](#), [80](#)
- Price, S. L. (2014). Predicting crystal structures of organic compounds, *Chem. Soc. Rev.* **43**: 2098–2111. [38](#)

- Ramirez-Montes, P. I., Ochoa, M. E., Santillan, R., Ramírez, D. J. and Farfán, N. (2014). Steroidal wheel-and-axle host type molecules: Insights from awkward shape, conformation, $Z' > 1$ and packing, *Cryst. Growth Des.* **14**: 4681–4690. [54](#)
- Reddy, J. P., Prabhakaran, P. and Steed, J. W. (2016). Polymorphism of (*Z*)-3-bromopropenoic acid: A high and low Z' pair, *Cryst. Growth Des.* **16**: 4021–4025. [54](#)
- Rigaku Oxford Diffraction (2015). *CRYSTALISPRO Software system, version 1.171.38.41*, Rigaku Corporation, Oxford, UK. [43](#)
- Ritzert, N. L., Rodríguez-Lopez, J., Tan, C. and Abruna, H. D. (2013). Kinetics of interfacial electron transfer at single-layer graphene electrodes in aqueous and nonaqueous solutions, *Langmuir* **29**: 1683–1694. [70](#)
- Rowland, R. S. and Taylor, R. (1996). Intermolecular nonbonded contact distances in organic crystal structures: Comparison with distances expected from van der Waals radii, *J. Phys. Chem.* **100**: 7384–7391. [20](#), [47](#), [63](#)
- Saito, K., Amano, M., Yamamura, Y., Tojo, T. and Atake, T. (2006). Low-temperature phase transitions of an organic ferroelectrics, phenazine-chloranilic acid, *J. Phys. Soc. Jpn.* **75**: 1–3. [31](#)
- Schlemper, E. O. and Britton, D. (1966). The crystal structure of trimethyltin cyanide, *Inorg. Chem.* **5**: 507–510. [63](#), [129](#)
- Schomaker, V. and Trueblood, K. N. (1968). On the rigid-body motion of molecules in crystals, *Acta Cryst.* **B24**: 63–76. [77](#), [97](#)
- Schönleber, A. (2011). Organic molecular compounds with modulated crystal structures, *Z. Kristallogr.* **226**: 499–517. [12](#), [19](#), [20](#), [38](#), [54](#), [72](#), [80](#)
- Schönleber, A., Pattison, P. and Chapuis, G. (2003). The (3+1)-dimensional superspace description of the commensurately modulated structure of *p*-chlorobenzamide (α -form) and its relation to the γ -form, *Z. Kristallogr.* **218**: 507–513. [21](#), [22](#), [23](#), [38](#), [40](#), [54](#)
- Schönleber, A., van Smaalen, S. and Larsen, F. K. (2010). Orientational disorder in Λ -cobalt(III) sepulchrate trinitrate, *Acta Crystallogr.* **C66**: 107–109. [8](#), [70](#), [76](#), [77](#), [82](#), [83](#), [84](#), [103](#), [105](#)

- Schönleber, A., van Smaalen, S., Weiss, H. C. and Kesel, A. J. (2014). N–H···O and C–H···F hydrogen bonds in the incommensurately modulated crystal structure of adamantan-1-ammonium 4-fluorobenzoate, *Acta Crystallogr.* **B70**: 652–659. [20](#), [21](#), [38](#)
- Schreurs, A. M. M., Xian, X. and Kroon-Batenburg, L. M. J. (2010). EVAL15: A diffraction data integration method based on ab initio predicted profiles, *J. Appl. Crystallogr.* **43**: 70–82. [41](#), [56](#), [72](#), [93](#)
- Sheldrick, G. M. and Taylor, R. (1977). Trimethyltin methylsulphinate, *Acta Crystallogr.* **B33**: 135–137. [63](#), [129](#)
- Siegler, M. A., Parkin, S. and Brock, C. P. (2012). [Ni(MeCN)(H₂O)₂(NO₃)₂].(15-crown-5).MeCN: Detailed study of a four-phase sequence that includes an intermediate modulated phase, *Acta Crystallogr.* **B68**: 389–400. [38](#)
- Smith, A. E. (1952). The crystal structure of urea-hydrocarbon complexes, *Acta Crystallogr.* **5**: 224–235. [6](#)
- Steed, J. W. (2003). Should solid-state molecular packing have to obey the rules of crystallographic symmetry, *CrystEnggComm* **5**: 169–179. [54](#)
- Steed, J. W. (2016). *High Z' Structure Data Base*, Durham University, <http://zprime.co.uk/database>. [80](#)
- Steed, K. M. and Steed, J. W. (2015). Packing problems: High *Z'* crystal structures and their relationship to co-crystals, inclusion compounds, and polymorphism, *Chem. Rev.* **115**: 2895–2933. [54](#), [80](#)
- Steiner, T. and Desiraju, G. R. (1998). Distinction between the weak hydrogen bond and the van der Waals interaction, *Chem. Commun.* pp. 891–892. [65](#), [85](#)
- Stokes, H. T., Campbell, B. J. and van Smaalen, S. (2011). Generation of (3+*d*)-dimensional superspace groups for describing the symmetry of modulated crystalline structures, *Acta Crystallogr.* **A67**: 45–55. [17](#), [19](#), [20](#), [22](#), [24](#), [40](#), [41](#), [55](#), [59](#), [62](#), [76](#), [93](#), [94](#), [95](#), [114](#)
- Stone, F. G. A. and West, R. (eds) (1967). *Advances in Organometallic Chemistry*, Vol. 5, Academic Press, Cambridge, Massachusetts. [39](#)

- Subashini, A., Leela, S., Ramamurthi, K., Arakcheeva, A., Stoeckli-Evans, H., Petricek, V., Chapuis, G., Pattison, P. and Reji, P. (2013). Synthesis, growth and characterization of 4-bromo-4-nitrobenzylidene aniline (BNBA): A novel nonlinear optical material with a (3+1)-dimensional incommensurately modulated structure, *CrystEngComm* **15**: 2474–2481. [38](#)
- Takaki, Y., Nakata, K., Taniguchi, T. and Sakurai, K. (1978). Disordered crystal structure of the γ form and reversible solid-phase transformations of *p*-chlorobenzamide, *Acta Crystallogr.* **B34**: 2579–2586. [21](#)
- Taylor, R., Cole, J. C. and Groom, C. R. (2016). Molecular interactions in crystal structures with $Z' > 1$, *Cryst. Growth Des.* **16**: 2988–3001. [54](#)
- Trotter, J. (1961). The crystal and molecular structure of biphenyl, *Acta Crystallogr.* **14**: 1135–1140. [18](#)
- van Smaalen, S. (1987). Superspace-group description of short-period commensurately modulated crystals, *Acta Crystallogr.* **A43**: 202–207. [54](#)
- van Smaalen, S. (2012). *Incommensurate Crystallography*, Oxford University Press, Oxford. [12](#), [30](#), [38](#), [40](#), [54](#), [72](#), [76](#), [78](#), [80](#), [81](#), [101](#), [102](#)
- van Smaalen, S., Campbell, B. J. and Stokes, H. T. (2013). Equivalence of superspace groups, *Acta Crystallogr.* **A69**: 75–90. [17](#), [19](#), [20](#), [22](#), [24](#), [40](#), [41](#), [55](#), [59](#), [62](#), [76](#), [93](#), [94](#), [95](#), [114](#)
- Wagner, T. and Schönleber, A. (2009). A non-mathematical introduction to the superspace description of modulated structures, *Acta Crystallogr.* **B65**: 249–268. [12](#), [54](#)
- Welberry, T. R. (2004). *Diffuse X-ray scattering and models of disorder*, 1 edn, Oxford University Press, Oxford. [34](#), [63](#)
- Welberry, T. R. (2014). One hundred years of diffuse X-ray scattering, *Metall. Mater. Trans.* **A45**: 75–84. [34](#)
- Welberry, T. R. and Weber, T. (2015). One hundred years of diffuse scattering, *Crystallogr. Rev.* **22**: 2–78. [34](#)

- Willis, T. M. (2006). 4.1. Thermal diffuse scattering of X-rays and neutrons, in U. Shmueli (ed.), *International Tables for Crystallography*, Vol. B, Springer, pp. 400–406. [34](#), [63](#)
- Zentner, C. A., Lai, H. W. H., Greenfield, J. T., Wiscons, R. A., Zeller, M., Campana, C. F., Talu, O., Fitzgerald, S. A. and Rowsell, J. L. C. (2015). High surface area and Z' in a thermally stable eight-fold polycatenated hydrogen-bonded framework, *Chem. Commun.* **51**: 11642–11645. [54](#)
- Zhang, X., Zhao, H., Palatinus, L., Gagnon, K. J., Bacsá, J. and Dunbar, K. R. (2016). Self-assembly of organocyanide dianions and metalorganic macrocycles into polymeric architectures including an unprecedented quadruple helical aperiodic structure, *Cryst. Growth Des.* **16**: 1805–1811. [38](#)

Publications

Two chapters of this thesis are published in the international scientific literature:

Chapter 3:

Dey, S., Schönleber, A., Mondal, S. and van Smaalen, S. (2016).
Superspace description of trimethyltin hydroxide at $T = 100$ K,
Z. Kristallogr. **231**: 427-434.

Chapter 5:

Dey, S., Schönleber, A., Mondal, S., Prathapa, S. J., van Smaalen, S. and Larsen, F. K. (2016).
The $Z' = 12$ superstructure of Λ -cobalt(III) sepulchrate trinitrate governed by C–H \cdots O hydrogen bonds,
Acta Crystallogr. **B72**: 372–380.

Two chapters of this thesis will be submitted for publication

Chapter 4:

Dey, S., Schönleber, A., Mondal, S., Ali Sk, I. and van Smaalen, S.
Modulated inter-strand C–H \cdots O bonds in the high Z' superstructure of trimethyltin hydroxide (to be submitted).

Chapter 6:

Dey, S., Schönleber, A., van Smaalen, S.,
Intermediate low temperature phases of Λ -Co(III) sepulchrate trinitrate (to be submitted).

Contribution to published articles in international scientific literature where the content is relevant to this thesis:

Noohinejad, L., Mondal, S., Ali, S. I., Dey, S., van Smaalen, S. and Schönleber, A. (2015).

Resonance-stabilized partial proton transfer in hydrogen bonds of incommensurate phenazine-chloranilic acid,

Acta Crystallogr., **B71**, 228–234.

Acknowledgements

The successful completion of this thesis has been achieved with the kind help of number of persons. During this time, I have understood the importance of critical thinking, collaborative work, patience, honesty and mental boost from family and friends.

First of all, I would like to express my deepest gratitude towards my supervisors, Prof. dr. Sander van Smaalen and PD dr. Andreas Schönleber for giving me the opportunity to work on the two projects. I thank them for their patience in teaching me the fundamentals of crystallography, superspace and also necessary soft skills. What matters most is every rigorous discussion have contributed towards enriching my scientific knowledge.

I would also take this opportunity to thank Dr. Václav Petříček, Dr. Michal Dusek and Dr. Lukás Palatinus, Institute of Physics, Academy of Sciences, Prague, Czech Republic for their invaluable time to address queries regarding the software suites JANA2006 and SUPERFLIP, and also for developing the suites to meet up to the requirements of latest projects. I would also like to acknowledge the fruitful discussions that I have had with them during congress meetings.

I thank Dr. Carsten Paulmann, Dr. Martin Tolkien and Dr. Wolfgang Morgenroth for their assistance during our diffractions experiments at the beamline F1 and D3, DESY, Hamburg, Germany.

I would like to sincerely thank Dr. Swastik Mondal, Dr. Sk Imran Ali and Dr. Leila Noohinejad who are former members of our laboratory for helping me both scientifically and socially. Regular exchange of ideas, exploring each other's scientific problems and social mingling every now and then meant a strong bond established amongst us.

I would also like thank my colleagues of our laboratory Dr. Christian B. Hübschle, Dr. Maxim Bykov, Dr. Elena Bykova, Dr. Alexander Wölfel, Dr. Leyla

Ismailova, Mr. Sitaram Ramakrishnan, Mr. Claudio Eisele and Mr. Georgios Aprilis for their sincere help in scientific issues.

No scientific project is successful without proper management. The efforts of Mrs. Denise Kelk-Huth put forward patiently in dealing with a spectrum of bureaucratic and management issues have ensured that I had a smooth beginning and stay in the Laboratory. I would also like to acknowledge the ideas and help of Mr. Franz Fischer, Mr. Alfred Suttner and Mrs. Kerstin Küspert for their time in dealing with technical issues on a regular basis.

I sincerely thank Prof. dr. P. N. Santhosh and Prof. dr. R. Nirmala, Indian Institute of Technology Madras, Chennai, India and Dr. V. P. S. Awnana, National Physical Laboratory, New Delhi, India for recommending me to explore the field of crystallography.

My private life in Bayreuth has been deeply influenced amongst the company of my friends Max Himmelmann, Felix Otto, Victor Graumann and Tobias Schultes. I also take this opportunity to thank Mr. Kedar Kolharkar and Dr. Yamini Avadhut who have been very supportive during my stay.

The shaping of a character is very much like a potter building up different kind of utensils while using the same basic raw materials. I think that applies appropriately to my family, specially my 'Ma' (Mother) who has been 'THE' factor in making me whatever I am today. Any words trying to describe their constant inspiration and backing would belittle their contributions.

Declaration

Ich versichere hiermit eidesstattlich, dass ich diese Dissertation selbstständig und nur unter Verwendung angegebener Quellen und zulässiger Hilfsmittel erstellt habe. Ich habe bisher keine Promotionsversuche unternommen. Ich habe bisher weder die Hilfe von gewerblichen Promotionsberatern bzw. -vermittlern in Anspruch genommen, noch werde ich sie künftig in Anspruch nehmen.

Somnath Dey

Bayreuth, den

